A SELF-CONSISTENT VISCOUS BLAST WAVE MODEL AND ITS APPLICATIONS TO HIGH ENERGY NUCLEAR COLLISIONS

A Dissertation

by

ZHIDONG YANG

Submitted to the Office of Graduate and Professional Studies of
Texas A&M University
in partial fulfillment of the requirements for the degree of

DOCTOR OF PHILOSOPHY

Chair of Committee,	Rainer J. Fries
Committee Members,	Ralf Rapp
	Carl A. Gagliardi
	Charles M. Folden III
Head of Department,	Grigory Rogachev

December 2019

Major Subject: Physics

ABSTRACT

Collisions of nuclei at large energies create fireballs of hot hadronic matter and quark gluon plasma. The properties of these extreme forms of nuclear matter can be studied by the experiments at the Relativistic Heavy Ion Collider (RHIC) and Large Hadron Collider (LHC). In this work we refine tools to study the matter in nuclear collisions and we infer the shear viscosity of hot hadronic matter from data.

Hadronic observables in the final stage of the heavy-ion collisions can be described well by hydrodynamics or blastwave parameterizations. We construct a blastwave model with self-consistent viscous corrections by calculating the viscous stress tensor from the parameterized flow field in the Navier-Stokes approximation. We improve similar models developed earlier by using a more realistic flow field and by calculating the time derivative terms by solving the ideal hydrodynamic equations analytically. Such a viscous blastwave can describe important features of the fireball without running numerically expensive hydrodynamics. We can validate the blastwave by comparison with established hydrodynamic calculations. We can quantify the uncertainty and bias from the simplifications of hypersurface and flow field by systematically comparing to hydrodynamic calculations with resonance decays and bulk stress included.

As a first application, we focus on the freeze-out temperature T_{fo} and the specific shear viscosity η/s of hot hadronic matter at that temperature. We use statistical Bayesian analysis tools to extract η/s at $T = T_{\text{fo}}$ from experimental data. Our approach is complementary to existing extractions from viscous hydrodynamics. The latter is sensitive to an averaged shear viscosity during that time evolution while our analysis is only sensitive to the shear viscosity at kinetic freeze-out. We can use the comparison to hydrodynamics to remove some systematic bias in the extraction results of T and η/s.

We can also use the viscous blastwave to provide realistic input for quark recombination models. These calculations had previously assumed breaking of thermal equilibrium in a naive way which is now replaced by viscous corrections to equilibrium. We get the quark spectra at $T \approx T_c$

from the blastwave and then use recombination to get spectra and elliptic flow v_2 of identified hadrons at intermediate transverse momentum p_T (2 GeV/c $< p_T < 6$ GeV/c). We find a moderate breaking of the constituent quark number scaling (QNS) law consistent with experimental data from RHIC and LHC. Thus, we demonstrate that the QNS law is not a necessary feature of quark recombination.

DEDICATION

This work is dedicated to my family: my father Benlun Yang, my mother Cuilan Yao and my younger brother Zhiliang Yang.

ACKNOWLEDGMENTS

Firstly, I would like to express my sincere gratitude to my advisor Prof. Rainer J. Fries for the continuous support of my Ph.D study and related research, for his patience, motivation, and immense knowledge. His guidance helped me in all the time of research and writing of this thesis.

Also I would like to thank the rest of my thesis committee: Prof. Ralf Rapp, Prof. Carl A. Gagliardi, and Prof. Charles M. Folden III, for their insightful comments and encouragement, which widened my research from various perspectives.

My sincere thanks also goes to the fellow graduate students at the Cyclotron Institute: Dr. Zilong Chang, Dr. Yifeng Sun, Dr. Xiaojian Du, Dr. Shuai Liu and Yanfang Liu, who provided me a lot of help, and whom I had many discussions with. I also give my thanks to my former and current colleagues in Prof. Fries's group: Dr. Guangyao Chen, Dr. Sidharth Somanathan, Dr. Michael Kordell and Steven Rose, who gave me valuable help and suggestions.

Finally, I would like to thank my family: my father, my mother and my younger brother, as well as my friends: Weihua Jin, Wuhua Wu, Dr. Haiqin Huang, Dr. Yan Yang, Dr. Shumao Zhang, Dr. Wenlong Yuan, Dr. Fuxiang Li, Dr. Chen Sun, Dr. Han Cai, Dr. Zhijin Li and Yang Zhang. Without your support and company, it is impossible for me to persist and finish this work.

CONTRIBUTORS AND FUNDING SOURCES

Contributors

This work was supervised by a dissertation committee consisting of Professor Rainer J. Fries, Professor Carl A. Gagliardi and Professor Ralf Rapp of the Department of Physics and Astronomy and Professor Charles M. Folden III of the Department of Chemistry.

All other work conducted for the dissertation was completed by the student independently, under the supervision of Rainer J. Fries of the Department of Physics and Astronomy.

In this thesis I have used the hydrodynamics code MUSIC developed by Charles Gale et al. (McGill) and the statistical analysis package MADAI developed by Steffen A. Bass et al. (Duke). All other code used for this thesis was written by me. Computations were carried out on resources provided by Texas A&M University, in particular the Brazos Cluster and the Ganglia LAB Cluster.

Funding Sources

Graduate study was supported by a fellowship from Texas A&M University and a graduate research assistantship by the US National Science Foundation under award nos. 1516590, 1550221 and 1812431.

NOMENCLATURE

QCD	Quantum Chromodynamics
QGP	Quark-Gluon Plasma
LHC	Large Hadron Collider
RHIC	Relativistic Heavy Ion Collision
EOS	Equations of State
QNS	Quark Number Scaling
RRM	Resonance Recombination Model
RL	Retiere and Lisa
MADAI	Models and Data Analysis Initiative
LFR	Lower Fit Range
RFR	Regular Fit Range
HFR	Higher Fit Range
CM	Center of Mass
RHS	Right Hand Side
LHS	Left Hand Side

TABLE OF CONTENTS

Page

LIST OF FIGURES

FIGURE Page

LIST OF TABLES

1. INTRODUCTION

1.1 Quark Gluon Plasma

Quantum chromodynamics (QCD) is the theory of the strong interaction. Quarks are the fundamental degrees of freedom and couple to each other through gluons with coupling constant g. QCD is a non-Abelian theory and gluons can also interact with each other.The coupling strength $\alpha_s = g^2/(4\pi)$ between quarks and gluons becomes small at high energies. This is known as "the asymptotic freedom" [5, 6]. On the other hand, QCD exhibits confinement, the property that quarks and gluons can only exist in bound states that are color neutral, i.e. have no strong charge. No free single quarks or gluons have ever been observed in experiment. However, asymptotic freedom predicts that a new state of matter will be generated if the nuclear matter is hot and dense enough. In the new state, color-free quarks and gluons are deconfined from hadrons. This new state is called quark gluon plasma (QGP). The temperature to reach deconfinement and chiral phase transition is about $T_c = 160$ MeV [1].

There are several reasons why we need to study QGP. First it is related to the evolution of the universe. In the standard Big Bang theory, the universe was very hot initially. Its temperature T was higher than 200 MeV at about 10^{-6} s after the Big Bang. We expect that the universe was filled with QGP at those early times and had a QCD phase transition or crossover to hadronic matter at $T = T_c$.

To understand the evolution of the early universe, one must understand the properties of the QGP phase at high T. QGP may also exist in the core of neutron stars, where the mass density is higher than 10^{14} g/cm^3. With such high density, neutrons and protons are closely packed so that quarks and gluons may be deconfined. Thus quarks and gluons may have a large influence on the properties of neutron stars.

The early universe at $T \sim 200$ MeV is in the past and we can only observe neutron stars through indirect methods. How do we test our theoretical modeling of QGP? The answer is rel-

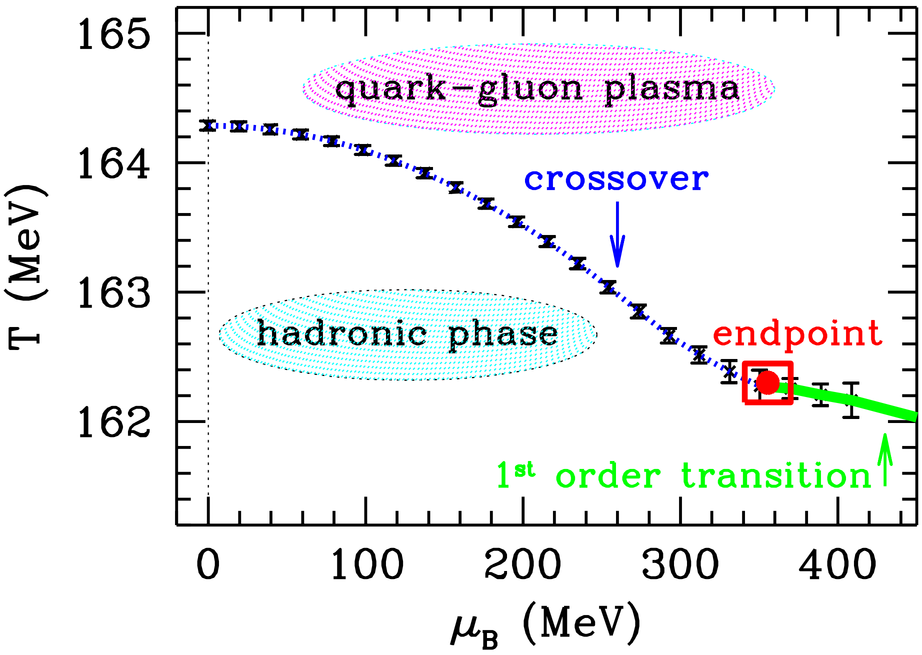

Figure 1.1: Phase diagram given by LQCD calculation, reprinted from Ref. [1]. The solid line shows the first-order phase transitions, the dotted line indicates crossover transitions. Reprinted with permission from Ref. [1] Copyright 2004 by SISSA.

ativistic heavy ion collisions. The Relativistic Heavy Ion Collider (RHIC) and the Large Hadron Collider (LHC) are experimental facilities aiming to probe the properties of nuclear matter at extremely high temperatures and densities. QGP will be generated if the nuclear matter is hot and dense enough. In the initial stage of heavy-ion collisions, hot and dense fireball is created by the overlapping nucleons of the target and projectile. The fireball cools down rapidly and expands into the surrounding vacuum, then reaches a chemical freeze-out stage T_{chem} where hadron species decouple from each other. Hadrons further collide and scatter elastically and reach a final kinetic freeze-out T_{kin} when the hadronic matter becomes so dilute that no interactions occur between hadrons any more (free streaming).

Based on the idea of asymptotic freedom, QGP is expected to have gas-like behavior. Soon after the start of the RHIC program it was realized that experimental data from this machine required a new paradigm. Although the original motivation for postulating the existence of QGP came from the known weakening of the strong-interaction coupling constant with temperature, it turned out that in reality QGP close to the pseudo-critical temperature T_c, i.e. at temperatures probed by the experimental programs at RHIC and LHC, behaves like a strongly coupled liquid [7, 8].

The first hint came from the great success achieved by *ideal* hydrodynamics (or hydrodynamics) in describing the flow of hadrons measured at RHIC [9, 10]. As it turns out, the process of cooling and expansion of the fireball of QGP and hadronic matter behaves hydrodynamically from very early times in the collision onward. In other words, the fireball exhibits a strong collective behavior. By convention, the beam goes in the longitudinal direction and the collision zone perpendicular to beam is called the transverse plane. In experiment, we can study the collective properties through transverse momentum (p_T) distributions of identified particles. These distributions have information about the transverse expansion and the temperature when the hadrons decouple from the system. For this reason, studying the bulk properties of the expanding fireball is important. In addition, probes can be used to study QGP further. Probes are particles created in the collision that are usually not part of the bulk of the fireball but can interact with it. Examples are QCD jets created by very high momentum quarks or gluons, heavy quarks and their bound states, and photons. In this thesis we will work exclusively with the bulk of the heavy ion collisions.

1.2 Relativistic Hydrodynamics

Relativistic hydrodynamics describes the space-time evolution of the energy-momentum tensor $T^{\mu\nu}$ of the strongly interacting QGP or hadronic matter and has been extensively applied to high energy heavy-ion collisions [11, 12]. It assumes that the created fireball reaches thermal equilibrium rapidly, which means local relaxation times need to be much shorter than macroscopic dynamical time. Applying ideal hydrodynamics to describe the expansion of the strongly-coupled matter generated in heavy-ion collisions was first proposed by Landau in 1953 [13]. As a macroscopic theory, hydrodynamics can provide several general properties of the system without tracking the complicated dynamics of every quark, gluon and hadron in the system. The ideal hydrodynamic equations of motion (EOM) can be written as

$$\partial_\mu T^{\mu\nu} = 0 \tag{1.1}$$

which are equivalent to the local conservation of energy and momentum of a relativistic fluid. The energy-momentum tensor of an ideal fluid of energy density e and pressure p in its local rest frame is

$$T^{\mu\nu} = (e+p)u^\mu u^\nu - pg^{\mu\nu} \tag{1.2}$$

where u^μ is the 4-velocity describing the collective motion of a fluid cell. For viscous hydrodynamics, one needs to include the shear stress tensor $\pi^{\mu\nu}$ and bulk viscous pressure Π

$$T^{\mu\nu} = (e+p+\Pi)u^\mu u^\nu - (p+\Pi)g^{\mu\nu} + \pi^{\mu\nu} \tag{1.3}$$

$\pi^{\mu\nu}$ and Π are given by the gradient expansion of 4-velocity u^μ. For the first order (Navier-Stokes) approximation $\pi^{\mu\nu} = 2\eta \langle \partial^\mu u^\nu \rangle$ and $\Pi = \zeta \partial_\mu u^\mu$, where η and ζ are the corresponding shear and bulk viscosity constants. Various types of hydrodynamics have been developed for heavy ion collisions. For example, VISH2+1 is a (2+1)-dimensional hydrodynamic code which adopts longitudinal boost-invariant in the evolution [14]. MUSIC is a (3+1)-dimensional hydrodynamic code which has full space-time evolution [15]. We will use MUSIC in this work, but running in the numerically less expensive (2+1)D mode.

Hydrodynamics needs realistic initial conditions at a starting time τ_0. In the earliest stage of collisions, the coherent longitudinal motion is partially redirected into the transverse directions. This process starts out far from thermal equilibrium and thus cannot be described by hydrodynamics. At that time, the system can be described by classical gluon fields [16, 17]. In order to apply hydrodynamics, we need to know the energy-momentum distributions at the starting time

($\tau_0 \sim 0.2 - 1.0$ fm/c) of the hydrodynamic stage. In practice initial conditions are typically provided by the Glauber Model [18] or classical gluon field calculations (color glass condensate) [16, 17]. Initial conditions play an important role in hydrodynamics. It turns out the positions of the nucleons and the color charge density inside the colliding nuclei fluctuate event-by-event. Collisions at finite impact parameter b lead to fireballs with (an average) elliptic shape in the transverse plane. This causes anisotropic pressure gradients and finally leads to anisotropies in flow. Thus the initial spatial an isotropy of the nuclear reaction zone is finally transferred to momentum anisotropy. The most important observable of this effect is elliptic flow v_2. It is defined as the second order Fourier coefficient of the azimuthal particle spectrum

$$\frac{dN}{d^2p_T} = \frac{dN}{2\pi p_T dp_T}[1 + 2v_2(p_T)\cos(2\theta) + ...] \tag{1.4}$$

where N is the number of the particle, p_T is the transverse momentum and θ is the azimuthal angle.

Besides initial conditions, we also need to know the nuclear equation of state (EOS) to solve Eq. 1.1. The EOS is usually given by $p(e)$ or the speed of sound squared $c_s^2 = \frac{\partial p}{\partial e}$ and can be modeled or extracted from lattice QCD calculations [11, 12]. In the simplest case, nuclear matter above the critical temperature T_c is often modeled as an ideal gas of massless quarks and gluons with corresponding EOS $p = \frac{1}{3}e - \frac{4}{3}B$, where B is the bag pressure constant. Below T_c, the system is treated as a hadron resonance gas that includes all experimentally identified resonance states and has corresponding EOS. We will use the modern lattice QCD inspired EOS provided with MUSIC in chapter 3.

Once knowing initial conditions and EOS, the space-time evolution of the system can be calculated. As the system is expanding rapidly, the hydrodynamic description must be stopped when the mean free path of particles becomes too large and the fluid described by hydrodynamics must be converted into particles. The criterion to stop hydrodynamics is usually set to be constant temperature T_{fo} or constant energy density. Once all points in the hydrodynamic medium are below T_{fo}, hydrodynamics is stopped and the Cooper-Frye formula [19] is applied to convert hydrodynamic output into particles; see chapter 2.

The success of ideal hydrodynamics points to low shear viscosity η and low dissipation in QGP. However to measure shear viscosity one needs to go beyond *ideal* hydrodynamics and one should use *viscous* hydrodynamics.

1.3 Shear Viscosity

Ideal hydrodynamics was successful in central collisions between large nuclei (A≈200) at midrapidity at the top RHIC energies ($\sqrt{s_{NN}} = 130$ GeV and 200 GeV), but gradually broke down in smaller collision systems, such as particles away from midrapidity, peripheral collisions and low-energy collisions [20]. This fact reveals the importance of dissipative effects and the necessity of developing viscous hydrodynamics. One of the most popular approaches is the Israel-Stewart formalism, which includes second order viscous corrections [21]. One can find how viscous corrections affect elliptic flow especially at large p_T, as shown in Fig. 1.2. Generally speaking, viscous corrections include both bulk and shear stress as introduced in Eq. (1.3).

The success of ideal hydrodynamics points to very low dissipation in QGP and thus very low specific shear viscosity η/s, i.e. the ratio of shear viscosity η to entropy density s. Viscous hydrodynamics simulations compared to data allowed for the quantitative extraction of specific shear viscosity η/s from data [22, 23, 24]. Kovtun, Son and Starinets hypothesized that there might be a universal lower bound of $\eta/s = 1/(4\pi)$ for the specific shear viscosity, based on their study of strongly interacting systems using AdS/CFT correspondence [25]. Collective flow observables like v_2 are particularly sensitive to shear viscosity. The first generation of calculations used relativistic hydrodynamics with a fixed, temperature-independent η/s as a parameter. Hydrodynamics was run all the way to kinetic freeze-out at the end of the hadronic phase, which was modeled very similar to the approach discussed further below here. Obviously the value of η/s extracted from this method is averaged over the entire temperature evolution of the QGP *and* the hot hadronic matter below T_c, a range of several hundred MeV at top RHIC and LHC energies. Shear stress signals a departure from thermal equilibrium and microscopical particle distributions are no longer thermal. Their deformation has to be taken into account at freeze-out. η/s extracted through this

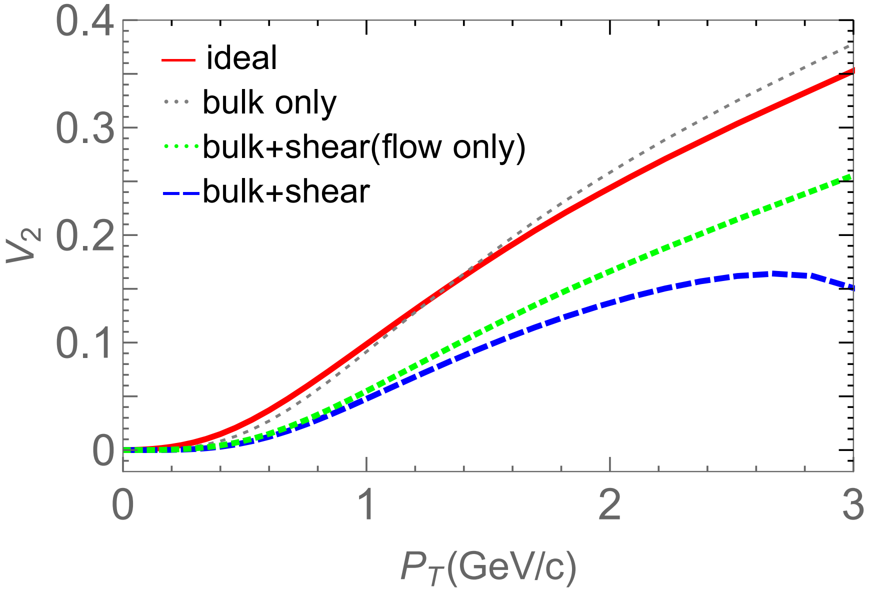

Figure 1.2: Transverse flow of protons with and without viscous corrections. Events are generated by the MUSIC hydrodynamic code. Here "ideal" means no viscosity, "bulk only" means no shear viscosity, "bulk+shear flow only" means there is no deformation δf at freeze-out and "bulk+shear" includes viscous corrections both during evolution and at freeze-out. The freeze-out temperature T is set to be 130 MeV and the specific shear viscosity η/s is set to be 0.2.

method thus also includes the effects of deformations of particle distributions at freeze-out that are present at finite shear stress [26, 23]. This deformation effect is extremely important and will be used here to measure η/s at freeze-out. It will be described in detail in chapter 2. Fig. 1.2 shows how large the expected effect is.

Subsequently, several groups have argued that the hadronic phase should be rather described by hadronic transport models because the specific shear viscosity in the hadronic phase could be too large for the evolution to be described accurately in second order viscous fluid dynamic codes [27, 28]. This argument was aided by estimates of η/s for a hadronic matter from chiral perturbation theory or hadronic transport by various groups [29, 30, 31, 32, 33, 34, 35, 36, 37]. While these calculations do not agree quantitatively, they generally find rather large specific shear viscosity for hot hadronic matter, $\eta/s \gtrsim 5/(4\pi)$ even very close to T_c; examples see Fig. 1.3. Thus fluid dynamic calculations were matched to hadronic transport models just below T_c while

η/s was retained as a parameter only for the QGP phase and the crossover region around T_c. Even more recently, fluid dynamic calculations using simple parameterizations have also been used to constrain the functional form of the temperature dependence of η/s, mostly for the QGP case [27, 38, 39]. We refer the reader to [40] for a review of fluid dynamic simulations of nuclear collisions, including the extraction of shear viscosity.

On the theoretical side, lattice calculations of η/s have been attempted but are challenging [41, 42, 43, 44]. They generally find η/s to be close to the conjectured lower bound around T_c with a rather slow rise towards higher temperatures, for examples see Fig. 1.3. However, pushing these

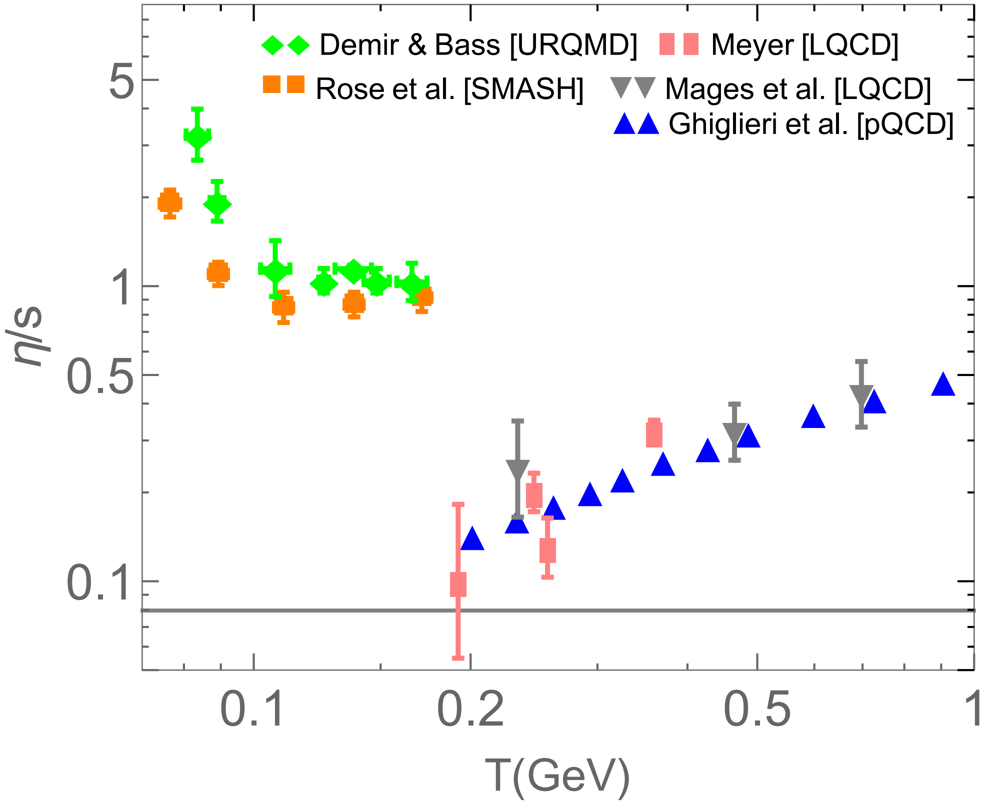

Figure 1.3: Previous calculations for specific shear viscosity η/s as a function of temperature. We will add our results in chapter 4.

calculations into the hadronic phase below T_c is difficult. Perturbative QCD calculations at leading order have indicated large values of η/s at temperatures well above T_c [45, 46], but a recent next-to-leading order calculation predicts a significant drop towards T_c which makes the perturbative results comparable to lattice QCD [47]. From general arguments one expects a minimum of η/s around T_c which has been found to be the case for a large variety or systems [48]. How fast the specific shear viscosity is rising towards lower temperatures below T_c cannot be seen as settled from either data nor first principle calculations. In any conceivable experiment information on specific shear viscosity in the QGP phase is always diluted by contributions from the hadronic phase, and thus uncertainties in hadronic η/s are directly responsibly for increased uncertainties of QGP shear viscosities extracted from data. One common feature of most hadronic transport calculations of η/s is that they do not seem to go smoothly to the QGP result $(1\ldots2)/(4\pi)$ around T_c. As the transition between QGP and hadronic matter is a crossover at small baryon chemical potential, very sharp features in the temperature dependence of η/s are not expected.

It is clear that an independent assessment of the hadronic specific shear viscosity is necessary to improve our extraction of QGP specific shear viscosity. As a reasonable minimum requirement, theoretical uncertainties coming from incomplete knowledge of the hadronic phase should inform realistic contributions to error bars for quantities extracted for the QGP phase. Moreover, the question of the specific shear viscosity of hot hadronic matter in itself is compelling. Maybe hadronic matter close to T_c is strongly interacting as well.

It is one of the main points of this thesis to argue that it is possible to use experimental data to estimate the specific shear viscosity of the hot hadronic matter at the kinetic freeze-out independently. The main effect of the time evolution of the system before freeze-out is the build-up of a flow field u^μ which leads to the system expanding and cooling. Viscous corrections to first order are given by gradients of the flow field (Navier-Stokes approximation). Computing the flow field in hydrodynamics, introduces additional dependences on initial conditions and the equation of state. We take a complementary approach and *fit* the final flow field, together with the temperature and system size at kinetic freeze-out. The specific shear viscosity is then a parameter at just one fixed temperature T_{fo}, the kinetic freeze-out temperature, and a set of chemical potentials

$\mu_{\rm fo} = (\mu_B, \mu_\pi, \ldots)$. Of course, such fits of flow fields and temperatures at freeze-out are well established and generally known as blastwave parameterizations [49, 50, 51]. We will use such a blastwave, with η/s added as a parameter, to extract $\eta/s(T_{\rm fo}, \mu_{\rm fo})$ for a variety of points ($T_{\rm fo}$,$\mu_{\rm fo}$) in different collision systems.

1.4 Blastwave Parameterization

Hydrodynamics is powerful and predictive but also requires significant computing resources. For some applications it is sufficient to consider blastwave parameterizations. Blastwave parameterizations try to capture an approximate snapshot of a hydrodynamic system at a fixed time or temperature. In fact it uses the same formalism, Cooper-Frye, which is also used for the freeze-out of hydrodynamic calculations. However, the details of the freeze-out (isothermal) surface and other properties, e.g. the flow field on the hypersurface are parameterizations with a set of fit parameters of the result of calculations. Using a simple ansatz for the flow field and freeze-out hypersurface, blastwaves can nevertheless provide good descriptions of some important features such as observed transverse momentum (p_T) spectra and elliptic flow. Due to their simplicity, blastwaves have been widely used in heavy ion collisions. Blastwaves are a useful way to discuss trends in heavy ion collision data. For example, from the parameters extracted by blastwave fits to experimental data, we can study the trends of flow velocity and freeze-out temperature in different centrality bins and different collision energies [52, 53]; see Fig. 4.3. The term "blastwave" comes from the assumption that the transverse velocity increases linearly with respect to the radius, akin to an explosion.

In 1976, Westfall et. al first introduced the nuclear fireball model, which assumed protons were emitted from the source isotropically [49]. In 1993, Schnedermann al. developed a blastwave model using boost-invariant longitudinal flow and radially increasing transverse flow [50]. They successfully fitted the transverse momentum spectra with only two parameters: a kinetic temperature (T_{fo}), and a radial flow strength (α_o). In 2001, Huovinen generalized this parameterization to noncentral collisions by adding an additional parameter (α_2) so that the flow strength is stronger in the reaction plane than out of the plane [10]. In 2003, Retiere and Lisa added the spatial deformation of the fireball and treated the transverse plane as an ellipse with semi axes R_x and R_y, so that the elliptic flow v_2 receives contributions both from the elliptic deformation (α_2) of the flow field, and from the elliptic spatial deformation (R_y/R_x) [51]. We will discuss these parameters in detail in chapter 2.

In this work, we introduce non-equilibrium deformations of particle distributions due to shear viscosity into the blastwave. We use the Navier-Stokes approximation to calculate viscous corrections, which are proportional to the traceless shear gradient tensor. Viscous corrections to blastwaves have been studied in [26, 54]. Both of these previous works assume spatial spherical symmetry in the transverse plane and free streaming for simplicity. We will generalize these assumptions here. The shear gradient tensor is expressed by the derivative terms of the flow field. The spatial derivatives are straightforward once the flow field is established. The time-derivatives cannot be given by the blastwave itself, but can be obtained by solving ideal hydrodynamic equations of motion. The details are presented in chapter 2. Here we emphasize that our blastwave is self-consistent and all viscous corrections are calculated from the same flow field.

By adding shear corrections, v_2 will increase and then decrease at large transverse momentum $p_T > 2$ GeV/c, unlike in the ideal case where v_2 continues to increase; see Fig. 2.5 (similar to the hydrodynamic case in Fig. 1.2). We can validate the blastwave by comparison with established hydrodynamic calculations; see chapter 3. Since the blastwave, for simplicity, ignores the effects of feed-down from hadronic resonances as well as bulk stress, we can quantify the uncertainty and bias from these simplifications by comparing to MUSIC calculations *with* resonance decays and bulk stress included. The latter comparison is important to remove the systematic bias in the extraction results of T and η/s in chapter 4. To our knowledge, this is the first such systematic comparison between hydrodynamics and blastwave fits.

1.5 Quark Recombination

Early experimental results from RHIC showed that there is a large baryon-to-meson ratio (close to 1) at intermediate transverse momentum regime, 2 GeV/$c < p_T < 6$ GeV/c [55, 56]. This was surprising as baryon production is usually suppressed compared to meson production in elementary collisions. Besides, an interesting scaling of elliptic flow v_2 between mesons and baryons is also found in this regime [3, 4, 2] suggesting the relationship

$$v_2(p_T) = n_q v_2^{(q)}(p_T/n_q) \tag{1.5}$$

between the elliptic flow of hadrons and the elliptic flow $v_2^{(q)}$ for quarks at $T = T_c$ (n_q is the number of valence quarks contained in the hadron) This is called the constituent quark number

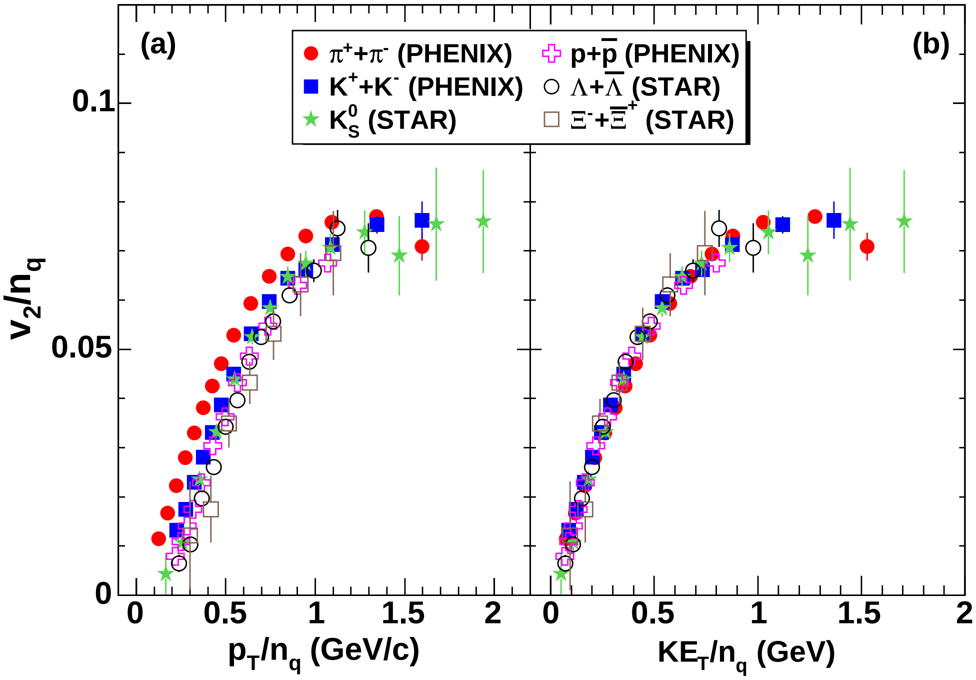

Figure 1.4: Quark scaling results from PHENIX and STAR experiment, reprint from Ref. [2]. (a) v_2/n_q vs p_T/n_q and (b) v_2/n_q vs KE_T/n_q for identified particles obtained from PHENIX in minimum bias Au+Au collisions. The STAR results are from Refs. [3, 4]. Reprinted with permission from Ref. [2] Copyright 2007 by APS.

scaling (QNS) law. As a result, plotting v_2/n_q vs p_T/n_q leads to a universal curve, at least at intermediate p_T, see Fig. 1.4. One can also check the scaling law at low p_T by plotting v_2 as a function of the transverse kinetic energy $KE_T = m_T - m_0$, where m_0 is the hadron mass and $m_T = \sqrt{p_T^2 + m_0^2}$ is the hadron's transverse mass. KE_T scaling can be understood well in hydrodynamics or blastwaves [57]. However, the constituent quark number scaling poses a big challenge to hydrodynamic models. In hydrodynamics, the valence quark number should not influence the behavior of a hadron species. For example, the proton and phi meson with roughly equal mass should have very similar flow. Also, the QNS law applies in a region in $p_T > 2$ GeV/c where $v_2(p_T)$ has stopped growing and is flat or even decreasing. Such a behavior of $v_2(p_t)$ is not possible in (ideal) hydrodynamics and it suggests that in this region thermalization is broken.

To describe the baryon-over-meson enhancement and QNS at intermediate p_T, new ideas were needed. In 2003, it was found that the observations at intermediate p_T are successfully described by quark coalescence or recombination models [58, 59, 60, 61]. In these models, valence quarks are assumed to be abundant in phase space at $T = T_c$ and recombine to hadrons through quark recombination. The hadron formation process is usually assumed to be instantaneous and take a infinitely thin hypersurface ($\Delta\tau \sim 0$). Such an approximation usually gives good results for intermediate p_T. Energy conservation is violated and only momentum is conserved in these models. At intermediate p_T the violation is small but as a consequence instantaneous recombination cannot be applied in the low p_T range. As mentioned in [60], energy conservation approximately holds if $Q/p_T \ll 1$ which is guaranteed at intermediate p_T and for small $Q = m - (m_q + m_{\bar{q}})$, where m is the hadron mass and $m_{q,\bar{q}}$ is the quark mass.

In order to extend recombination to low p_T, in 2007 Ravagli and Rapp proposed an alternative implementation [62] and later formulated as Resonance Recombination Model (RRM) [57, 63]. In RRM, quark coalescence was interpreted as a resonance formation process, $q+\overline{q} \rightleftharpoons M$, and implemented via a Boltzmann equation. By doing this, energy-momentum conservation is guaranteed. The long-time limit for the Boltzmann equation naturally recovers thermal equilibrium.

In all recombination implementations, one main concern is how to implement hadron and parton distributions in coordinate and momentum space with their correct space-momentum correlations. Often, quarks are assumed to be in thermal equilibrium and hadron wave functions are assumed to be narrow (close to δ-functions) in momentum space. In order to describe the QNS law, thermalization is broken in [59, 60] and the elliptic flow of quarks in the fireball is implemented locally (cell by cell) and thus space-momentum correlations are neglected. This establishes the QNS law to high accuracy but it is unphysical since the elliptic flow should come from the collective flow field of the fireball.

Subsequently, it was widely believed that the QNS law is a necessary feature of quark recombination, and that violations of the QNS law found experimentally can be interpreted as evidence against quark recombination. Indeed, data from LHC shows the elliptic flow of identified hadrons following the QNS law to a lesser extent than data from RHIC [64]. Recent publication from ALICE report deviations from QNS law for Pb-Pb collisions [65]. They find significant deviations for the intermediate region $(m_T - m_0)/n_q \sim 0.8 - 2$ GeV/c^2 and the scaling law exhibits deviations at the level of $\pm 20\%$.

Here we argue that it is possible to describe the hadron elliptic flow with physical space-momentum correlations using quark recombination. To do this, we will generalize the calculation in [58, 59, 60] and use our improved blastwave as an input for quark recombination. In that case, the blastwave is utilized to give quark spectra at the critical temperature T_c. Note this is different from chapter 4, in which blastwave is applied to hadrons at T_{kin}. The blastwave has realistic space-momentum correlations. In addition, equilibrium at higher p_T is broken by viscous corrections in a systematic gradient expansion. This is the physical way to introduce the breaking of kinetic equilibrium and stop the growth of $v_2(p_T)$ that was not well understood in 2003.

In chapter 5, we use the viscous blastwave model and instantaneous quark recombination to fit spectra and elliptic flow v_2 of identical hadrons at intermediate p_T. In particular we check the QNS scaling law by fitting v_2 of different hadrons at a variety of collision energies and impact parameters. Though experimental measurement shows a deviation from QNS, we can obtain a rather good description via this quark recombination model. We also apply our blastwave together with the RRM and calculate the elliptic flow with the same blastwave parameters. We find these two models provide similar results. Our results indicate that QNS can be broken in quark recombination and careful quantitative calculations have to be carried out to study quark recombination.

In the next chapter, we present the viscous blastwave formalism. In chapter 3, we systematically compare our blastwave to hydrodynamic calculations with resonance decays and bulk stress included. In chapter 4, we apply our blastwave to extract the freeze-out temperature T_{fo} and the specific shear viscosity η/s of hot hadronic matter at that temperature. In chapter 5, we use the viscous blastwave to provide realistic input for quark recombination models. In chapter 6, we summarize our work.

2. A VISCOUS BLASTWAVE [*]

In this chapter, we present a blastwave parameterization of nuclear collisions at high energies. We will subsequently apply it to describe the final state of nuclear collisions at $T = T_{\text{fo}}$. However we will also apply it to the $T = T_c$ hypersurface in chapter 5. Comparing with previous blastwave models in the literature, we include non-equilibrium deformations of particle distributions due to shear viscosity η/s in the Navier-Stokes approximation, following previous work in Ref. [26, 54, 66]. We discuss details for computing the Navier-Stokes corrections including spatial and time derivative terms of the flow field. The spatial derivatives are straightforward once the flow field is given. The time-derivatives cannot be given by the blastwave itself, but can be obtained by solving ideal hydrodynamic equations of motion on top of a blastwave profile.

2.1 Cooper-Frye Formula

The spectrum of particles emitted from a constant temperature hypersurface is given by the Cooper-Frye formula [19]

$$E\frac{d^3N}{dp^3} = \frac{g}{(2\pi)^3}\int_\Sigma f(r,p)p^\mu d\Sigma_\mu \tag{2.1}$$

where $f(r,p)$ is the distribution function of the given particle species, p^μ is the particle 4-momentum, g is its degeneracy and $d\Sigma^\mu$ is the normal vector on the hypersurface. A major application of the Cooper-Frye formula is the freeze-out process where the particles are hadrons or hadron resonances and T is the freeze-out temperature T_{fo}.

For the blastwave, we make two major assumptions in our analysis, both of which have been routinely used and studied in the literature. The first is that at freeze-out the system of hadrons is close enough to kinetic equilibrium so that at any position $r^\mu = (t, x, y, z)$ there exists a local rest frame with a local temperature $T(r)$ and a set of chemical potentials $\mu(r)$ such that the particle

---

[*] Part of this chapter is reprinted with permissions from “A Blast Wave Model With Viscous Corrections” by Zhidong Yang and Rainer J. Fries, 2017, J. Phys. Conf. Ser. **832**, 012056, Copyright 2017 by IOP.

distribution in the local rest frame can be written as

$$f(r,p) = f_0(r,p) + \delta f(r,p) \tag{2.2}$$

where f_0 is the equilibrium Bose/Fermi-distribution with the local temperature and chemical potentials,

$$f_0(r,p) = \frac{1}{e^{(E-\mu(r,p))/T(r,p)} \mp 1} \tag{2.3}$$

with "-" for Bosons and "+" for Fermions and δf is a gradient correction of Navier-Stokes type. In the laboratory frame we can replace E with $p^\mu u_\mu$ which is a Lorentz invariant, Eq. (2.3) becomes

$$f_0(r,p) = \frac{1}{e^{(p^\mu u_\mu-\mu(r,p))/T(r,p)} \mp 1} \tag{2.4}$$

where u^μ is the flow field of the fireball.

For the δf term, we use the general form

$$\delta f(r,p) = \frac{\eta}{s}\frac{\Gamma(6)}{\Gamma(4+\lambda)}\left(\frac{E}{T}\right)^{\lambda-2}\frac{p_\mu p_\nu}{T^3}\sigma^{\mu\nu} f_0(r,p) \tag{2.5}$$

which follows from a generalized Grad ansatz [67]. The power λ parameterizes further details of the underlying microscopic physics. Here we mostly restrict ourselves to the original Grad ansatz $\lambda = 2$ which is widely used. Eq. (2.5) becomes

$$\delta f(r,p) = \frac{\eta}{s}\frac{p_\mu p_\nu}{T^3}\sigma^{\mu\nu} f_0(r,p) \tag{2.6}$$

We will include λ as a tuneable parameter in chapter 5. In the Navier-Stokes approximation, the viscous correction is proportional to the traceless shear stress tensor, defined as

$$\sigma^{\mu\nu} = \frac{1}{2}\left(\nabla^\mu u^\nu + \nabla^\nu u^\mu\right) - \frac{1}{3}\Delta^{\mu\nu}\nabla_\alpha u^\alpha \tag{2.7}$$

Here $\nabla^\mu = \Delta^{\mu\nu}\partial_\nu$, with $\Delta^{\mu\nu} = g^{\mu\nu} - u^\mu u^\nu$, is the derivative operator perpendicular to the flow field vector u^μ. The gradient corrections need to be small. For the quantitative analysis in chapter 4, we will ensure that numerically $\delta f \lesssim f$ for all relevant momenta in that analysis.

The second major assumption for the blastwave pertains to the simplified shape of the freeze-out hypersurface and flow field. In the longitudinal direction (along the colliding beams), we assume boost-invariance, which turns out to be a good approximation for particles measured around midrapidity at LHC and top RHIC energies. In the specific case of freeze-out, blastwave parameterizations assume it to happen at constant T and μ_{fo} which is approximated by the constant (longitudinal) proper time $\tau = \tau_0$ hypersurface.

This is supported by hydrodynamical calculations. In the transverse direction, the t-x-y shape of $T = const$ (smooth) hydro hypersurfaces have the famous Muffin shape which comes about through the competition of cooling and expansion; for examples see [14, 23]. In the blastwave, the sides of the muffin are removed for simplicity, and only the "lid" is modeled. Most particles in a rapidly expanding fireball will emerge from the lid since the flux scalar $p^\mu d\Sigma_\mu$ in the Cooper-Frye formula is the most favorable (recall Σ is the normal vector on the hypersurface). In a last step, the lid which has a curvature and might cover several fm/c is approximated by a constant τ surface. The study in chapter 3 will test the uncertainties introduced by these two basic assumptions for blastwaves.

2.2 Blastwave Parameterization

To parameterize the flow field, we start from the longitudinal rest frame. In the longitudinal (z-axis) rest frame there is only transverse flow in the $x-y$-plane which can be written as

$$\vec{v} = v_T\vec{e}_r + v_L\vec{e}_z = (v_T\cos\phi_b, v_T\sin\phi_b, 0) \tag{2.8}$$

or in relativistic form

$$u^\mu = (\cosh\eta_T, \sinh\eta_T\cos\phi_b, \sinh\eta_T\sin\phi_b, 0) \tag{2.9}$$

where v_T is the transverse velocity, $\eta_T = \frac{1}{2}\log[(1+v_T)/(1-v_T)]$ is the transverse flow rapidity, and ϕ_b is the azimuthal angle of the flow vector in the transverse plane. We can extend expression (2.9) to all z, where the longitudinal velocity v_L is nonzero by using the boost symmetry. Specifically we apply a Lorentz boost with a rapidity η_L to arrive at

$$u^\mu = (\cosh\eta_L \cosh\eta_T, \sinh\eta_T \cos\phi_b, \sinh\eta_T \sin\phi_b, \sinh\eta_L \cosh\eta_T) \tag{2.10}$$

where $\eta_L = \frac{1}{2}\log[(1+v_L)/(1-v_L)]$. Boost invariance means that $\eta_L = \eta_s$ where $\eta_s = \frac{1}{2}\log[(t+z)/(t-z)]$ is the space time rapidity. we can rewrite the position vector in Milne coordinates (τ, η_s, x, y) as

$$r^\mu = (t, x, y, z) = (\tau\cosh\eta_s, x, y, \tau\sinh\eta_s) \tag{2.11}$$

Recall that boost-invariance naturally follows from a velocity ordering of particles emerging from a single position $z = 0$ as $v_L = z/t$. Here boost invariant means longitudinal flow does not depend on x and y and transverse flow is the same at different space time rapidity. Our final expression for the flow field everywhere is

$$u^\mu = (\cosh\eta_s \cosh\eta_T, \sinh\eta_T \cos\phi_b, \sinh\eta_T \sin\phi_b, \sinh\eta_s \cosh\eta_T) \tag{2.12}$$

where η_T and ϕ_b only depend on transverse coordinates x and y. For those, we follow the Retiere and Lisa (RL) parameterization [51]. The transverse shape of the fireball is assumed to be an ellipse with semi axes R_x and R_y in x- and y-directions respectively. We agree to define the coordinate axes such that the impact parameter b of the collision is measured along the x-axis. In the following we use the reduced radius $\rho = \sqrt{x^2/R_x^2 + y^2/R_y^2}$. The transverse velocity can be parameterized as [51]

$$v_T = \rho^n\,(\alpha_0 + \alpha_2\cos(2\phi_b)) \tag{2.13}$$

which encodes a Hubble-like velocity ordering with an additional shape parameter n. It is common to fix n=1 and thus v_T increases linearly with respect to the radius ρ. In chapter 4, we will keep

n as an independent parameter for increased precision. α_0 is the average velocity on the boundary $\rho = 1$, and α_2 parameterizes an elliptic deformation of the flow field coming from the original elliptic spatial deformation of systems with finite impact parameters. Higher order deformations could be present [54], but the observables discussed here are not particularly sensitive to them.

The time evolution of pressure gradients in the expansion leads to flow vectors tilted towards the smaller axis of the ellipse [51]. This is accomplished by demanding that the transverse flow vector is perpendicular to the elliptic surface at $\rho = 1$, i.e. $\tan\phi_b = R_x^2/R_y^2 \tan\phi_s$, where $\phi_s = \arctan y/x$ is the azimuthal angle of the position r^μ. It is convenient to write the radial coordinate as $\vec{r} = (x, y) = (R_x\rho\cos\phi, R_y\rho\sin\phi)$ with $\tan\phi = R_x/R_y \tan\phi_s$. Using Eq. (2.11), we can write the hypersurface as

$$d\Sigma^\mu = dxdydzd\tau\delta(\tau - \tau)\ \mathbf{n}^\mu = \tau R_x R_y \rho d\rho d\phi d\eta_s\ \mathbf{n}^\mu \tag{2.14}$$

with outbound normal vector

$$\mathbf{n}^\mu = (\cosh\eta_s, 0, 0, \sinh\eta_s) \tag{2.15}$$

The momentum vector in the laboratory frame is written in the standard form as

$$p^\mu = (m_T\cosh y, p_T\cos\theta, p_T\sin\theta, m_T\sinh y) \tag{2.16}$$

where p_T is the transverse momentum, y is the longitudinal momentum rapidity, θ is the azimuthal angle of p_T in the transverse plane, and $m_T = \sqrt{p_T^2 + m^2}$ is the transverse mass for the particle. Then we have

$$p^\mu d\Sigma_\mu = \tau R_x R_y m_T \rho\cosh(\eta_s - y) d\eta_s d\rho d\phi \tag{2.17}$$

We can also write

$$dp^3 = dp_T^2 dp_z = m_T\cosh y dp_T^2 dY = E dp_T^2 dy \tag{2.18}$$

Hence for hadrons measured around midrapidity ($y = 0$) the spectrum given by Eq. (2.1) takes the standard form

$$\frac{dN}{dyd^2p_T} = g\tau R_x R_y m_T \int_0^1 d\rho \int_0^{2\pi} d\phi \int_{-\infty}^{\infty} d\eta_s \frac{\rho\cosh\eta_s}{(2\pi)^3} f_0(\rho,\phi,\eta_s)\left[1+\frac{\eta}{s}\frac{p_\mu p_\nu}{T^3}\sigma^{\mu\nu}\right] \tag{2.19}$$

2.3 Shear Stress Tensor

We can now determine the shear stress tensor $\sigma^{\mu\nu}$ for the RL blastwave. As we have mentioned in chapter 1, viscous corrections to the blastwave have been studied in [26, 54] but have assumed spatial spherical symmetry in the transverse plane ($R_x = R_y$) and free streaming for the time derivatives in $\sigma^{\mu\nu}$. Both assumptions seem to be inadequate. In particular, the elliptic spatial deformation contributes significantly to the elliptic flow v_2, as we will demonstrate at the end of this chapter. With spatial azimuthal symmetry the derivative terms are much simpler than in our case.

Once the ansatz for the flow field is fixed, as done in the last section, computing shear stress can be reduced to the task of computing derivatives of η_s, η_T and ϕ_b. For spatial derivatives, η_s only depends on z and the latter two only depends on x and y. For time-derivatives, we will use the hydrodynamic equations of motion. By convention, in the following part we will use $g^{\mu\nu} \equiv \{1,-1,-1,-1\}$, $x^\mu \equiv g^{\mu\nu}x_\nu$, $\partial_\mu \equiv \frac{\partial}{\partial x^\mu}$ and $x^\mu = (x^0, x^1, x^2, x^3)$.

2.3.1 Spatial Derivatives

We start with the derivatives of η_T, which are expressed by radius ρ and azimuthal angle ϕ_b. Recall that we have $\rho = \sqrt{x^2/R_x^2 + y^2/R_y^2}$ and $\tan\phi_b = \frac{y}{x}\frac{R_x^2}{R_y^2}$. Then

$$\frac{\partial\rho}{\partial x} = \frac{\partial\sqrt{x^2/R_x^2 + y^2/R_y^2}}{\partial x} = \frac{1}{\sqrt{x^2/R_x^2 + y^2/R_y^2}}\frac{x}{R_x^2} = \frac{1}{\rho}\frac{x}{R_x^2} = \frac{\cos\phi}{R_x} \tag{2.20}$$

$$\frac{\partial\tan\phi_b}{\partial x} = \frac{R_x^2}{R_y^2}\frac{\partial(y/x)}{\partial x} = \frac{R_x^2}{R_y^2}\left(\frac{y}{-x^2}\right) = \frac{\tan\phi_b}{-x} \tag{2.21}$$

For derivative of $\cos\phi_b$, when $\cos\phi_b = \frac{1}{\sqrt{1+\tan^2\phi_b}} > 0$

$$\frac{\partial\cos\phi_b}{\partial x} = -\frac{\tan\phi_b}{(1+\tan^2\phi_b)^{\frac{3}{2}}}\frac{\partial\tan\phi_b}{\partial x} = \frac{1}{x}\frac{\tan^2\phi_b}{(1+\tan^2\phi_b)^{\frac{3}{2}}} = \frac{1}{x}\sin^2\phi_b\cos\phi_b \tag{2.22}$$

when $\cos\phi_b = -\frac{1}{\sqrt{1+\tan^2\phi_b}} < 0$

$$\frac{\partial\cos\phi_b}{\partial x} = \frac{\tan\phi_b}{(1+\tan^2\phi_b)^{\frac{3}{2}}}\frac{\partial\tan\phi_b}{\partial x} = -\frac{1}{x}\frac{\tan^2\phi_b}{(1+\tan^2\phi_b)^{\frac{3}{2}}} = \frac{1}{x}\sin^2\phi_b\cos\phi_b \tag{2.23}$$

which is identical to Eq. (2.22). Using derivatives of $\tan\phi_b$ and $\cos\phi_b$, we can easily obtain derivatives of $\sin\phi_b$ and $\cos 2\phi_b = \frac{1-\tan^2\phi_b}{1+\tan^2\phi_b}$,

$$\frac{\partial\sin\phi_b}{\partial x} = \cos\phi_b\frac{\partial\tan\phi_b}{\partial x} + \tan\phi_b\frac{\partial\cos\phi_b}{\partial x} = \frac{\sin\phi_b}{-x} + \frac{1}{x}\sin^3\phi_b = -\frac{1}{x}\sin\phi_b\cos^2\phi_b \tag{2.24}$$

$$\frac{\partial\cos 2\phi_b}{\partial x} = \frac{-4\tan\phi_b}{(1+\tan^2\phi_b)^2}\frac{\partial\tan\phi_b}{\partial x} = \frac{4\tan^2\phi_b}{(1+\tan^2\phi_b)^2}\frac{1}{x} = \frac{\sin^2(2\phi_b)}{x} \tag{2.25}$$

Based on the above expressions, we now obtain the x-derivative for v_T and η_T

$$\begin{aligned}\frac{\partial v_T}{\partial x} =& \alpha_2\frac{\partial\cos 2\phi_b}{\partial x}\rho^n + v_T\frac{n}{\rho}\frac{\partial\rho}{\partial x} = \alpha_2\frac{\sin^2(2\phi_b)}{x}\rho^n + v_T\frac{n}{\rho}\frac{\cos\phi}{R_x} &(2.26)\\ \frac{\partial\eta_T}{\partial x} =& \frac{1}{1-v_T^2}\frac{\partial v_T}{\partial x} = \cosh^2\eta_T\frac{\partial v_T}{\partial x} &(2.27)\end{aligned}$$

Following the same process, we can obtain the derivative in the y-direction. For ρ and ϕ_b, we have

$$\frac{\partial\rho}{\partial y} = \frac{\partial\sqrt{\frac{x^2}{R_x^2}+\frac{y^2}{R_y^2}}}{\partial y} = \frac{1}{\sqrt{\frac{x^2}{R_x^2}+\frac{y^2}{R_y^2}}}\frac{y}{R_y^2} = \frac{1}{\rho}\frac{y}{R_y^2} = \frac{\sin\phi}{R_y} \tag{2.28}$$

$$\frac{\partial\tan\phi_b}{\partial y} = \frac{R_x^2}{R_y^2}\frac{\partial(y/x)}{\partial x} = \frac{R_x^2}{R_y^2}\frac{1}{x} = \frac{\tan\phi_b}{y} \tag{2.29}$$

$$\frac{\partial\cos\phi_b}{\partial y} = -\frac{\tan\phi_b}{(1+\tan^2\phi_b)^{\frac{3}{2}}}\frac{\partial\tan\phi_b}{\partial y} = -\frac{1}{y}\frac{\tan^2\phi_b}{(1+\tan^2\phi_b)^{\frac{3}{2}}} = -\frac{1}{y}\sin^2\phi_b\cos\phi_b \tag{2.30}$$

$$\frac{\partial \sin\phi_b}{\partial y} = \cos\phi_b \frac{\partial \tan\phi_b}{\partial y} + \tan\phi_b \frac{\partial \cos\phi_b}{\partial y} = \frac{\sin\phi_b}{y} - \frac{1}{y}\sin^3\phi_b = \frac{1}{y}\sin\phi_b\cos^2\phi_b \tag{2.31}$$

$$\frac{\partial \cos 2\phi_b}{\partial y} = \frac{-4\tan\phi_b}{(1+\tan\phi_b)^2}\frac{\partial \tan\phi_b}{\partial y} = -\frac{4\tan^2\phi_b}{(1+\tan\phi_b)^2}\frac{1}{y} = -\frac{\sin^2(2\phi_b)}{y} \tag{2.32}$$

then obtain the y-derivative for v_T and η_T

$$\frac{\partial v_T}{\partial y} = \alpha_2 \frac{\partial \cos 2\phi_b}{\partial y}\rho^n + v_T \frac{n}{\rho}\frac{\partial \rho}{\partial y} = -\alpha_2 \frac{\sin^2(2\phi_b)}{y}\rho^n + v_T \frac{n}{\rho}\frac{\sin\phi}{R_y} \tag{2.33}$$

$$\frac{\partial \eta_T}{\partial y} = \cosh^2\eta_T \frac{\partial v_T}{\partial y} \tag{2.34}$$

2.3.2 Time Derivatives

The task of determining the time-derivatives in $\sigma^{\mu\nu}$ can be reduced to the question of computing $\partial_\tau \eta_T$. We start from the relativistic ideal hydrodynamic equations of motion

$$\partial_\mu T^{\mu\nu} = 0\,, \tag{2.35}$$

$$T^{\mu\nu} = (e+p)u^\mu u^\nu - p g^{\mu\nu}\,. \tag{2.36}$$

where e is the local energy density and p is the pressure. We can restrict ourselves to ideal fluid dynamics to obtain the leading order expressions in a gradient expansion for the time derivatives. Dissipative corrections in the determination of the time derivatives would lead to terms of order $\eta^2 \times$ (second order spatial gradients) in δf which we neglect. The ideal fluid dynamics equations can be rewritten as follows. We first plug $T^{\mu\nu}$ into Eq. (2.35)

$$(e+p)u^\mu \partial_\mu u^\nu + (e+p)u^\nu \partial_\mu u^\mu + u^\mu u^\nu \partial_\mu e + u^\mu u^\nu \partial_\mu p - g^{\mu\nu}\partial_\mu p = 0\,. \tag{2.37}$$

then we contract with u_ν and simplify the result to be

$$0 = 0 + (e+p)\partial_\mu u^\mu + u^\mu \partial_\mu e + u^\mu \partial_\mu p - g^{\mu\nu} u_\nu \partial_\mu p = (e+p)\partial_\mu u^\mu + u^\mu \partial_\mu e\,. \tag{2.38}$$

Now we make use of $u^\mu u_\mu = 1$ and $u_\mu \partial_\nu u^\mu = 0$. With Eq. (2.38), Eq. (2.37) becomes

$$(e+p)u^\mu \partial_\mu u^\nu + u^\mu u^\nu \partial_\mu p - g^{\mu\nu}\partial_\mu p = 0 \tag{2.39}$$

By convention, $\Delta^{\mu\nu} \equiv g^{\mu\nu} - u^\mu u^\nu$ is the projection operator orthogonal to the flow four-velocity, $\bigtriangledown^\nu \equiv \Delta^{\mu\nu} d_\mu$, $D \equiv u^\alpha d_\alpha$ is the co-moving derivative and d_α is the covariant derivative. In Cartesian coordinate, $d_\alpha = \partial_\alpha$. Eq. (2.38), (2.39) can be generalized to be

$$De = -(e+p)\partial_\mu u^\mu = -(e+p)\triangle_\mu u^\mu \,, \tag{2.40}$$

$$Du^\mu = \frac{\nabla^\mu p}{e+p} \,. \tag{2.41}$$

Freeze-out is the process of decoupling of particles where the mean free path rapidly grows beyond the system size. In fluid dynamics this process is modelled through a sudden transition during which the mean free path goes from very small values to infinity instantaneously at $T = T$. The system is assumed to be free streaming, $Du^\mu = 0$, after the transition, i.e. from $T = T - \epsilon$ on (with small $\epsilon > 0$). This free streaming assumption has been used to determine time derivatives in the blastwave model in Ref. [26, 54]. However, it seems more physical to assume that the local particle distributions $f(r,p)$ remain frozen across the $T = T$ hypersurface and that $\sigma^{\mu\nu}$, including time derivatives, should be set by $T = T + \epsilon$. This is consistent with the treatment in hydrodynamics. Moreover, applying the viscous blastwave to temperatures higher than T_{fo} mandates using the proper time evolution. Eq. (2.40), (2.41) can be solved for the blastwave geometry and flow field assumed here to obtain the time derivatives we seek.

We rewrite Eq. (2.38), Eq. (2.39) as

$$u^\mu \partial_\mu e = -(e+p)\partial_\mu u^\mu \tag{2.42}$$

$$u^\mu \partial_\mu u^\nu = \frac{c_s^2}{(e+p)} g^{\mu\nu}\partial_\mu e - \frac{c_s^2}{(e+p)} u^\mu u^\nu \partial_\mu e \tag{2.43}$$

where $c_s^2 = \partial p/\partial e$ is the speed of sound squared, given by the equation of state of the system at

$T = T$, and plug Eq. (2.42) into Eq. (2.43)

$$u^\mu \partial_\mu u^\nu = \frac{c_s^2}{(e+p)} \partial^\nu e + c_s^2 u^\nu \partial_\mu u^\mu \,. \tag{2.44}$$

Recall the hypersurface is given by $\tau = \sqrt{t^2 - z^2}$ or $t = \tau \cosh \eta_s$, $z = \tau \sinh \eta_s$, so

$$\partial_0 = \frac{\partial}{\partial t} = \frac{\partial \tau}{\partial t}\frac{\partial}{\partial \tau} + \frac{\partial \eta_s}{\partial t}\frac{\partial}{\partial \eta_s} = \cosh \eta_s \partial_\tau - \frac{\sinh \eta_s}{\tau}\partial_{\eta_s} \tag{2.45}$$

$$\partial_3 = \frac{\partial}{\partial z} = \frac{\partial \tau}{\partial z}\frac{\partial}{\partial \tau} + \frac{\partial \eta_s}{\partial z}\frac{\partial}{\partial \eta_s} = -\sinh \eta_s \partial_\tau + \frac{\cosh \eta_s}{\tau}\partial_{\eta_s} \tag{2.46}$$

The flow velocity is $u^\mu = (\cosh \eta_s \cosh \eta_T, \sinh \eta_T \cos \phi_b, \sinh \eta_T \sin \phi_b, \sinh \eta_s \cosh \eta_T)$, then

$$\begin{aligned}
\partial_\mu u^\mu =&\partial_0 u^0 + \partial_1 u^1 + \partial_2 u^2 + \partial_3 u^3 \\
=& \cosh \eta_s \partial_\tau u^0 - \sinh \eta_s \partial_\tau u^3 + \partial_1 u^1 + \partial_2 u^2 + (\cosh \eta_s/\tau)\partial_{\eta_s} u^3 - (\sinh \eta_s/\tau)\partial_{\eta_s} u^0 \\
=&\partial_\tau \cosh \eta_T + \partial_1 u^1 + \partial_2 u^2 + \cosh \eta_T/\tau
\end{aligned} \tag{2.47}$$

and for a random 4-vector

$$\begin{aligned}
u^\mu \partial_\mu x =&u^0 \partial_0 x + u^1 \partial_1 x + u^2 \partial_2 x + u^3 \partial_3 x \\
=&(u^0 \cosh \eta_s - u^3 \sinh \eta_s)\partial_\tau x + u^1 \partial_1 x + u^2 \partial_2 x + (u^3 \cosh \eta_s/\tau - u^0 \sinh \eta_s/\tau)\partial_{\eta_s} x \\
=& \cosh \eta_T \partial_\tau x + u^1 \partial_1 x + u^2 \partial_2 x
\end{aligned} \tag{2.48}$$

Using $\partial_1 e = \partial_2 e = 0$ and $\partial_{\eta_s} e = 0$ because of the constant temperature hypersurface, then we have $\partial_0 e = \cosh \eta_T \partial_\tau e$, $\partial_3 e = -\sinh \eta_T \partial_\tau e$. Using Eq. (2.48), (2.42) and (2.44) become

$$\cosh \eta_T \partial_\tau e = -(e+p)\partial_\mu u^\mu \tag{2.49}$$

$$\begin{cases} \cosh\eta_T\partial_\tau u^0 + u^1\partial_1 u^0 + u^2\partial_2 u^0 = \dfrac{c_s^2}{e+p}\cosh\eta_s\partial_\tau e + c_s^2 u^0\partial_\mu u^\mu \\ \cosh\eta_T\partial_\tau u^1 + u^1\partial_1 u^1 + u^2\partial_2 u^1 = 0 + c_s^2 u^1\partial_\mu u^\mu \\ \cosh\eta_T\partial_\tau u^2 + u^1\partial_1 u^2 + u^2\partial_2 u^2 = 0 + c_s^2 u^2\partial_\mu u^\mu \\ \cosh\eta_T\partial_\tau u^3 + u^1\partial_1 u^3 + u^2\partial_2 u^3 = \dfrac{c_s^2}{e+p}\sinh\eta_s\partial_\tau e + c_s^2 u^3\partial_\mu u^\mu \end{cases} \tag{2.50}$$

The first and fourth equations in (2.50) are equivalent. Using one of them and together with Eq. (2.49), we have

$$\cosh\eta_T\partial_\tau\cosh\eta_T + u^1\partial_1\cosh\eta_T + u^2\partial_2\cosh\eta_T = -\frac{c_s^2}{\cosh\eta_T}\partial_\mu u^\mu + c_s^2\cosh\eta_T\partial_\mu u^\mu \tag{2.51}$$

Now the only unknown term in Eq. (2.51) is $\partial_\tau\cosh\eta_T$. Plugging in Eq. (2.47), we obtain the time derivative of the transverse flow rapidity,

$$(1 - c_s^2\tanh^2\eta_T)\partial_\tau\cosh\eta_T = c_s^2\tanh^2\eta_T(\partial_1 u^1 + \partial_2 u^2 + \frac{\cosh\eta_T}{\tau}) - \frac{u^1\partial_1 u^0}{u^0} - \frac{u^2\partial_2 u^0}{u^0} \tag{2.52}$$

in terms of known spatial derivatives. The time derivative of the direction of the transverse flow field can be computed by using (2.52) in the second and third equation in (2.50).

2.3.3 Full Derivatives

Using the expressions obtained in the two previous sections, we can write all the derivative terms with respect to $r^\mu = (t, x, y, z)$. Recall we have $\tau = \sqrt{t^2 - z^2}$, $\eta_s = \frac{1}{2}\ln\frac{t+z}{t-z}$, then

$$\begin{aligned} \frac{\partial\tau}{\partial z} &= -\frac{z}{\sqrt{t^2 - z^2}} = -\sinh\eta_s \\ \frac{\partial\eta_s}{\partial z} &= \frac{t}{t^2 - z^2} = \frac{\cosh\eta_s}{\tau} \\ \frac{\partial\tau}{\partial t} &= \frac{t}{\sqrt{t^2 - z^2}} = \cosh\eta_s \\ \frac{\partial\eta_s}{\partial t} &= -\frac{z}{\sqrt{t^2 - z^2}} = -\frac{\sinh\eta_s}{\tau} \end{aligned} \tag{2.53}$$

The full derivatives of $u^0 = \cosh\eta_s \cosh\eta_T$ are

$$\begin{cases} \dfrac{\partial u^0}{\partial t} = \cosh\eta_s \dfrac{\partial u^0}{\partial \tau} - \dfrac{\sinh\eta_s}{\tau}\dfrac{\partial u^0}{\partial \eta_s} = \cosh\eta_s \dfrac{\partial u^0}{\partial \tau} - \dfrac{\sinh\eta_s}{\tau} \sinh\eta_s \cosh\eta_T \\ \dfrac{\partial u^0}{\partial x} = \cosh\eta_s \sinh\eta_T \dfrac{\partial \eta_T}{\partial x} = \cosh\eta_s \sinh\eta_T \cosh^2\eta_T [\alpha_2 \dfrac{\sin^2(2\phi_b)}{x}\rho^n + v_T \dfrac{n}{\rho}\dfrac{\cos\phi}{R_x}] \\ \dfrac{\partial u^0}{\partial y} = \cosh\eta_s \sinh\eta_T \dfrac{\partial \eta_T}{\partial y} = \cosh\eta_s \sinh\eta_T \cosh^2\eta_T [-\alpha_2 \dfrac{\sin^2(2\phi_b)}{y}\rho^n + v_T \dfrac{n}{\rho}\dfrac{\sin\phi}{R_y}] \\ \dfrac{\partial u^0}{\partial z} = -\sinh\eta_s \dfrac{\partial u^0}{\partial \tau} + \dfrac{\cosh\eta_s}{\tau}\dfrac{\partial u^0}{\partial \eta_s} = -\sinh\eta_s \dfrac{\partial u^0}{\partial \tau} + \dfrac{\cosh\eta_s}{\tau} \sinh\eta_s \cosh\eta_T \end{cases} \tag{2.54}$$

The full derivatives of $u^1 = \sinh\eta_T \cos\phi_b$ are

$$\begin{cases} \dfrac{\partial u^1}{\partial t} = \cosh\eta_s \dfrac{\partial u^1}{\partial \tau} - \dfrac{\sinh\eta_s}{\tau}\dfrac{\partial u^1}{\partial \eta_s} = \cosh\eta_s \dfrac{\partial u^1}{\partial \tau} \\ \dfrac{\partial u^1}{\partial x} = \cosh\eta_T \cos\phi_b \cdot \cosh^2\eta_T [\alpha_2 \dfrac{\sin^2(2\phi_b)}{x}\rho^n + v_T \dfrac{n}{\rho}\dfrac{\cos\phi}{R_x}] + \sinh\eta_T \cdot \dfrac{1}{x}\sin^2\phi_b \cos\phi_b \\ \dfrac{\partial u^1}{\partial y} = \cosh\eta_T \cos\phi_b \cdot \cosh^2\eta_T [-\alpha_2 \dfrac{\sin^2(2\phi_b)}{y}\rho^n + v_T \dfrac{n}{\rho}\dfrac{\sin\phi}{R_y}] - \sinh\eta_T \cdot \dfrac{1}{y}\sin^2\phi_b \cos\phi_b \\ \dfrac{\partial u^1}{\partial z} = -\sinh\eta_s \dfrac{\partial u^1}{\partial \tau} + \dfrac{\cosh\eta_s}{\tau}\dfrac{\partial u^1}{\partial \eta_s} = -\sinh\eta_s \dfrac{\partial u^1}{\partial \tau} \end{cases} \tag{2.55}$$

The full derivatives of $u^2 = \sinh\eta_T \sin\phi_b$ are

$$\begin{cases} \dfrac{\partial u^2}{\partial t} = \cosh\eta_s \dfrac{\partial u^2}{\partial \tau} - \dfrac{\sinh\eta_s}{\tau}\dfrac{\partial u^2}{\partial \eta_s} = \cosh\eta_s \dfrac{\partial u^2}{\partial \tau} \\ \dfrac{\partial u^2}{\partial x} = \cosh\eta_T \sin\phi_b \cdot \cosh^2\eta_T [\alpha_2 \dfrac{\sin^2(2\phi_b)}{x}\rho^n + v_T \dfrac{n}{\rho}\dfrac{\cos\phi}{R_x}] - \sinh\eta_T \cdot \dfrac{1}{x}\sin\phi_b \cos^2\phi_b \\ \dfrac{\partial u^2}{\partial y} = \cosh\eta_T \sin\phi_b \cdot \cosh^2\eta_T [-\alpha_2 \dfrac{\sin^2(2\phi_b)}{y}\rho^n + v_T \dfrac{n}{\rho}\dfrac{\sin\phi}{R_y}] + \sinh\eta_T \cdot \dfrac{1}{y}\sin\phi_b \cos^2\phi_b \\ \dfrac{\partial u^2}{\partial z} = -\sinh\eta_s \dfrac{\partial u^2}{\partial \tau} + \dfrac{\cosh\eta_s}{\tau}\dfrac{\partial u^2}{\partial \eta_s} = -\sinh\eta_s \dfrac{\partial u^2}{\partial \tau} \end{cases} \tag{2.56}$$

The full derivatives of $u^3 = \sinh\eta_s \cosh\eta_T$ are

$$\begin{cases} \dfrac{\partial u^3}{\partial t} = \cosh\eta_s \dfrac{\partial u^3}{\partial \tau} - \dfrac{\sinh\eta_s}{\tau}\dfrac{\partial u^3}{\partial \eta_s} = \cosh\eta_s \dfrac{\partial u^3}{\partial \tau} - \dfrac{\sinh\eta_s}{\tau}\cosh\eta_s\cosh\eta_T \\ \dfrac{\partial u^3}{\partial x} = \sinh\eta_s\sinh\eta_T \dfrac{\partial \eta_T}{\partial x} = \sinh\eta_s\sinh\eta_T\cosh^2\eta_T[\alpha_2 \dfrac{\sin^2(2\phi_b)}{x}\rho^n + v_T \dfrac{n}{\rho}\dfrac{\cos\phi}{R_x}] \\ \dfrac{\partial u^3}{\partial y} = \sinh\eta_s\sinh\eta_T \dfrac{\partial \eta_T}{\partial y} = \sinh\eta_s\sinh\eta_T\cosh^2\eta_T[-\alpha_2 \dfrac{\sin^2(2\phi_b)}{y}\rho^n + v_T \dfrac{n}{\rho}\dfrac{\sin\phi}{R_y}] \\ \dfrac{\partial u^3}{\partial z} = -\sinh\eta_s \dfrac{\partial u^3}{\partial \tau} + \dfrac{\cosh\eta_s}{\tau}\dfrac{\partial u^3}{\partial \eta_s} = -\sinh\eta_s \dfrac{\partial u^3}{\partial \tau} + \dfrac{\cosh\eta_s}{\tau}\cosh\eta_s\cosh\eta_T\,. \end{cases} \tag{2.57}$$

The last task is to calculate shear stress tensor $\sigma^{\mu\nu}$ and correction $p_\mu p_\nu \sigma^{\mu\nu}$. According to the definition $\sigma^{\mu\nu} \equiv \frac{1}{2}(\nabla^\mu u^\nu + \nabla^\nu u^\mu) - \frac{1}{3}\Delta^{\mu\nu}\nabla_\alpha u^\alpha$ with $\nabla^\mu = \Delta^{\mu\nu}\partial_\nu$, $\Delta^{\mu\nu} = g^{\mu\nu} - u^\mu u^\nu$, we have

$$\nabla^\mu u^\nu = \partial^\mu u^\nu - u^\mu u^\alpha \partial_\alpha u^\nu \qquad \nabla^\nu u^\mu = \partial^\nu u^\mu - u^\nu u^\alpha \partial_\alpha u^\mu, \tag{2.58}$$

$$\frac{1}{2}(\nabla^\mu u^\nu + \nabla^\nu u^\mu) = \frac{1}{2}(\partial^\mu u^\nu + \partial^\nu u^\mu) - \frac{1}{2}u^\alpha \partial_\alpha (u^\mu u^\nu) \tag{2.59}$$

and obtain

$$\begin{cases} \sigma^{00} = \partial^0 u^0 - u^0 u^\alpha \partial_\alpha u^0 - \dfrac{1}{3}(1 - u^0 u^0)\partial_\alpha u^\alpha \\ \sigma^{0i} = \dfrac{1}{2}(\partial^0 u^i + \partial^i u^0) - \dfrac{1}{2}u^\alpha \partial_\alpha (u^0 u^j) + \dfrac{1}{3}u^0 u^i \partial_\alpha u^\alpha \\ \sigma^{ij} = \dfrac{1}{2}(\partial^i u^j + \partial^j u^i) - \dfrac{1}{2}u^\alpha \partial_\alpha (u^i u^j) - \dfrac{1}{3}(g^{ij} - u^i u^j)\partial_\alpha u^\alpha \end{cases} \tag{2.60}$$

where $\partial^0 = \partial_0 = \frac{\partial}{\partial t}$, $\partial^1 = -\partial_1 = -\frac{\partial}{\partial x}$, $\partial^2 = -\partial_2 = -\frac{\partial}{\partial y}$ and $\partial^3 = -\partial_3 = -\frac{\partial}{\partial z}$, are the spatial and time derivatives we calculated earlier.

Finally the correction $p_\mu p_\nu \sigma^{\mu\nu}$ is given by

$$p_\mu p_\nu \sigma^{\mu\nu} = p^0 p^0 \sigma^{00} - 2p^0 p^i \sigma^{0i} + p^i p^j \sigma^{ij} \tag{2.61}$$

with $p^\mu = (m_T \cosh y, p_T \cos\theta, p_T \sin\theta, m_T \sinh y)$.

2.4 Blastwave Parameters

In this part we discuss the parameters in the viscous blastwave model and study some of the dependences of particle spectra and elliptic flow on these parameters. The initial parameters in the model are $\tilde{\mathcal{P}} = (\mu, c_s^2, \lambda, \tau, T, R_y, R_x, n, \alpha_0, \alpha_2, \eta/s)$, where μ denotes any chemical potentials for the particles considered. Not all parameters are good fit parameters but can rather be constrained by additional physics considerations. We are also often interested in reducing the number of fit parameters for efficiency and stability. The following considerations can help. Some of the parameters play important roles and reflect the main features of the model, which we are interested in. We make them fit parameters. Others are less interesting even though some physical meaning can be attached to them, such as the speed of sound squared c_s^2 and chemical potentials μ. For the latter, we may estimate or obtain their values otherwise. In addition, some of the parameters are highly correlated with each other. For these parameters, we may resolve the correlations by additional theoretical considerations.

The parameter λ is related to the scalar momentum dependence in δf. As we mentioned earlier, we will mostly use $\lambda = 2$, which is also an assumption widely used in the literature [26, 14, 54]. We will retain λ as a tuneable parameter in chapter 5.

In terms of the geometric parameters, it turns out the ratio R_y/R_x has a large influence on elliptical flow, so we always choose R_y/R_x as a fit parameter. Our observables depend on R_x, R_y and τ primarily through the ratio R_y/R_x, and through the overall volume $\sim R_x R_y \tau$ which determines the normalization of spectra. Dependences on the individual size parameters are completely absent in the ideal blastwave, which only depends on the overall volume $R_x R_y \tau$. However these dependences enter in a sub-leading way through the viscous correction terms in our model. We constrain R_x, R_y and τ by fitting the ratio R_y/R_x, the time τ and by adding the simple geometric estimate

$$R_x \approx (R_0 - b/2) + \tau c_\tau(\alpha_0 + \alpha_2)\,, \tag{2.62}$$

for the propagation of the fireball boundary in x-direction. Here R_0 is the radius of the colliding nucleus, b is the impact parameter and $c_\tau = \bar{\alpha}_0/\alpha_0$ relates the *time-averaged* surface velocity.

Based on the discussion above, we will restrict the set of simultaneously fitted parameters to a maximum of seven, choosing $\mathcal{P} = (\tau, T, R_y/R_x, n, \alpha_0, \alpha_2, \eta/s)$ from the full set $\tilde{\mathcal{P}}$. It is also interesting to explore the dependence of spectra and elliptic flow on the remaining parameters.

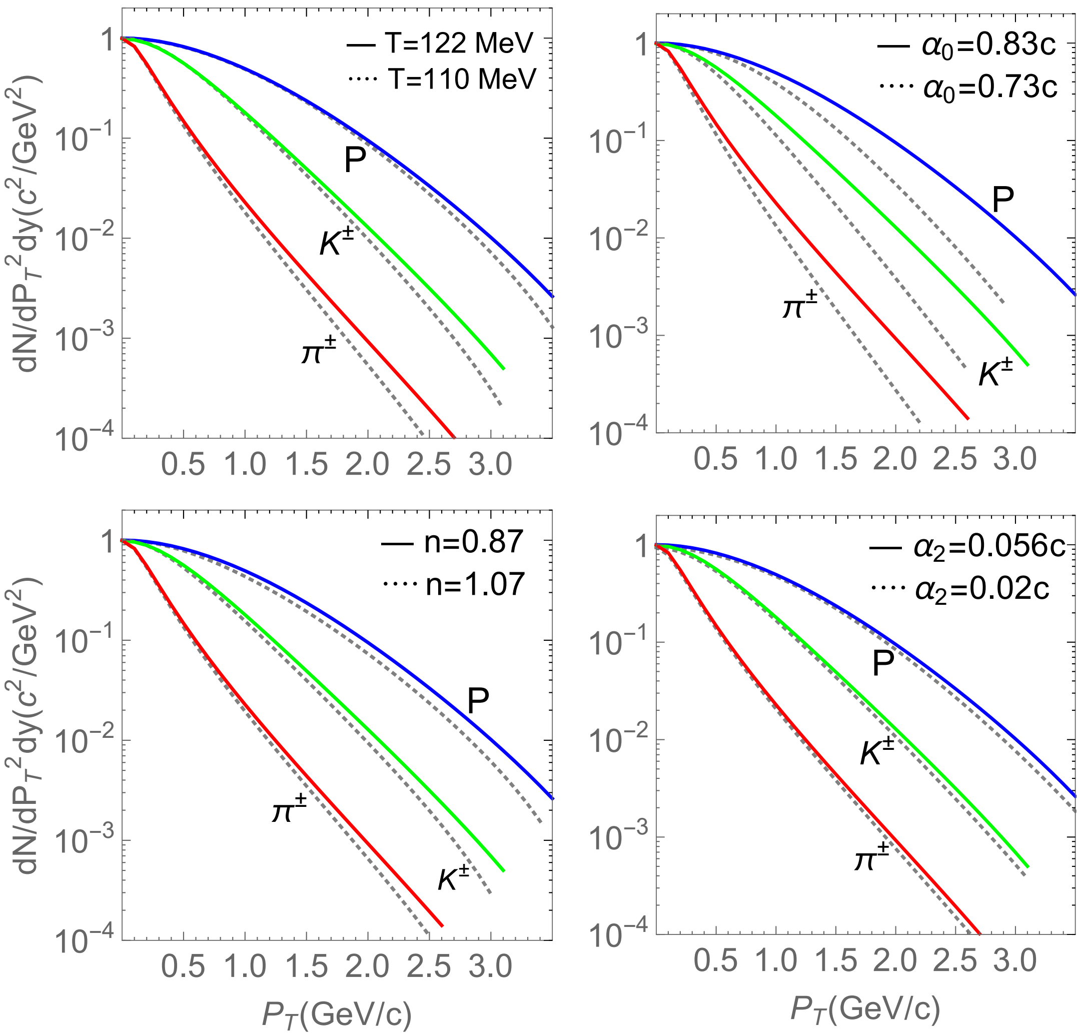

Figure 2.1: Transverse momentum spectra of proton, kaon and pion calculated with varying parameters T, α_0, n and α_2. The spectra are normalized to 1. The default parameters are from blastwave fit results for ALICE 30-40%, i.e. $\tau = 11.4$ fm, $T = 122$ MeV, $R_y/R_x = 1.27, n = 0.87, \alpha_0 = 0.83c, \alpha_2 = 0.056c, \eta/s = 0.32$.

Generally speaking, spectra are most sensitive to the freeze-out temperature T, boundary veloc-

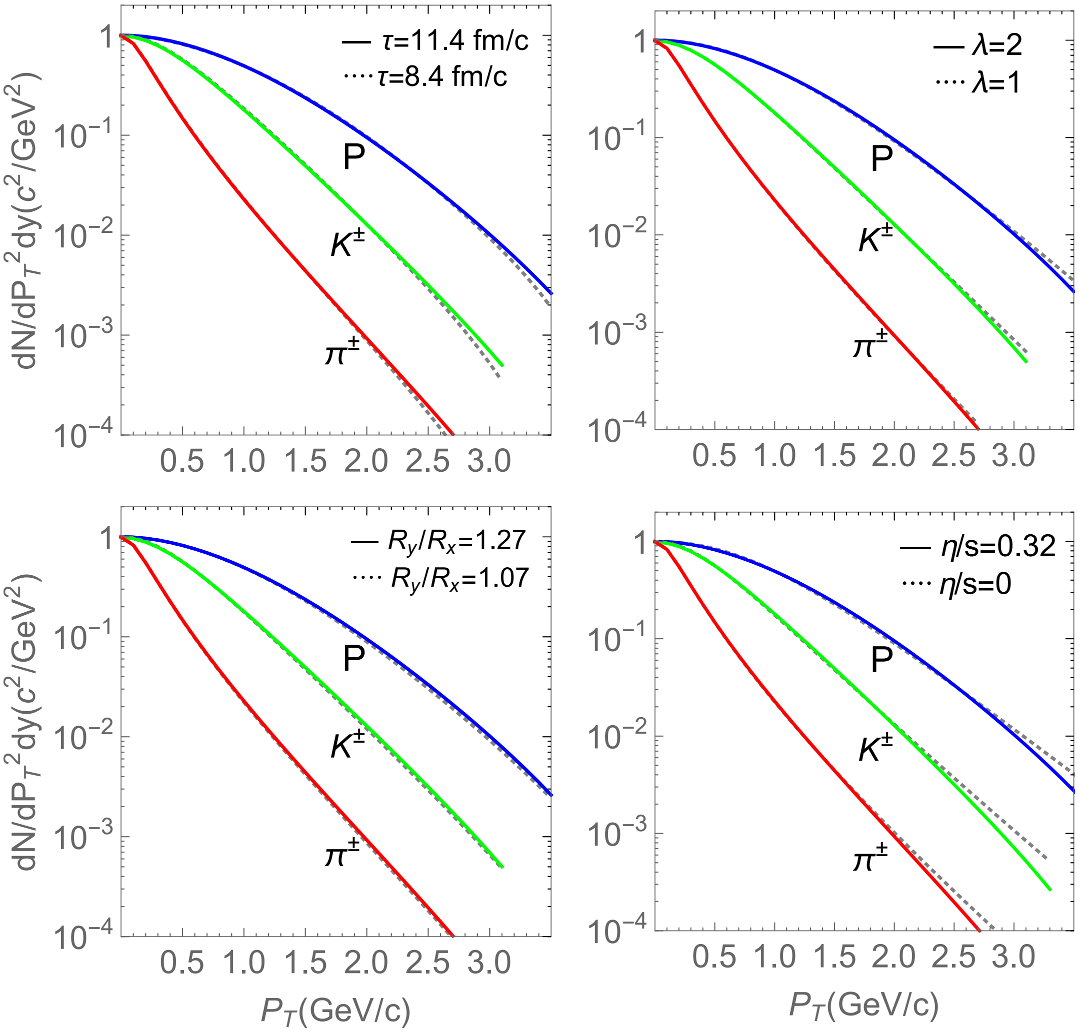

Figure 2.2: Transverse momentum spectra of proton, kaon and pion calculated with varying parameters $\tau, \lambda, R_y/R_x$ and η/s. The spectra are normalized to 1. The default parameters are the same as used in Fig. 2.1.

ity α_0 and velocity profile n. The elliptic flow is most sensitive to the azimuthal flow deformation parameter α_2, spatial deformation R_y/R_x as well as the specific shear viscosity η/s. When fitting experimental measurements, α_2, R_y/R_x and η/s are mostly constrained by elliptic flow, other parameters are constrained by both spectra and elliptic flow. The dependence of spectra on the set of parameters $(T, \alpha_0, n, \alpha_2, \tau, R_y/R_x, \lambda, \eta/s)$ are shown in Fig. 2.1 and 2.2. The systematic dependence of elliptic flow on these parameters are shown in Fig. 2.3, 2.4 and 2.5.

From Fig. 2.1, we can find the spectra become steeper as T decreases, which comes mainly from the particle distribution term $\sim e^{-E/T}$. We can also find that spectra become steeper as the average flow velocity decreases. This can be achieved by lower boundary velocity α_0, higher radial profile parameter n and lower elliptic flow deformation α_2. This is because small flow velocity means fewer particles are pushed to large momentum and thus fewer particles in high p_T, which makes the spectra steeper. From Fig. 2.2 we can find the dependence of spectra on $(\tau, \lambda, R_y/R_x, \eta/s)$ is rather small, because these parameters mainly affect the shape of the spectra through viscous corrections δf, which is a more subtle effect than a dependence through f_0.

In general, elliptic flow v_2 starts to deviate from the equilibrium behavior with the increase of p_T. From Fig. 2.3, we can find (τ, T, n) have little influence on elliptic flow at low p_T and only change elliptic flow at high p_T. From Fig. 2.4, we can find a large dependence of elliptic flow on $(\alpha_0, \alpha_2, R_y/R_x)$. In particular, elliptic flow increases dramatically for larger α_2 and it moves up parallelly as R_y/R_x increases. At last, the dependence of elliptic flow on λ and η/s is shown in Fig. 2.5. For λ, we can find viscous corrections become larger as λ increases and $\lambda = 2$ has the largest corrections. Similarly, viscous corrections also become larger as η/s increases since they are directly proportional to η/s.

We can also check the magnitude of viscous corrections with respect to p_T. In particular, for the dependence of the spectra on η/s, we calculate the spectra for the same parameters with and without the correction term δf. As expected, we find at large p_T the correction δf is largest and increases dramatically. This is due to the p^2-dependence of δf. Note that despite the p^2-dependence of δf in the local rest frame, δf does not have to strictly vanish at small transverse momenta p_T in the *lab frame*. In fact, due to the largest correction δf at large p_T, extracted values of η/s are very sensitive to v_2 at large p_T. Since δf cannot be too large, we should be cautious when choosing fit ranges. Generally we exclude points for which the slope of v_2 turns negative, since in this case δf may be too large.

From Fig. 2.6, we can read the ratio of correction δf to original f_0. Within the p_T range, e. g. 0-2.0 GeV/c for pions, 0-2.5 GeV/c for kaons and 0-3.3 GeV/c for protons, the largest correction is 9% for pions, 14% for kaons and 23% for protons respectively. The typical size of viscous corrections is much smaller than the maximum numbers quoted here. We have to be mindful that δf cannot be too large. As discussed earlier, higher order corrections in shear stress would have to be taken into account if $\delta f \approx f$

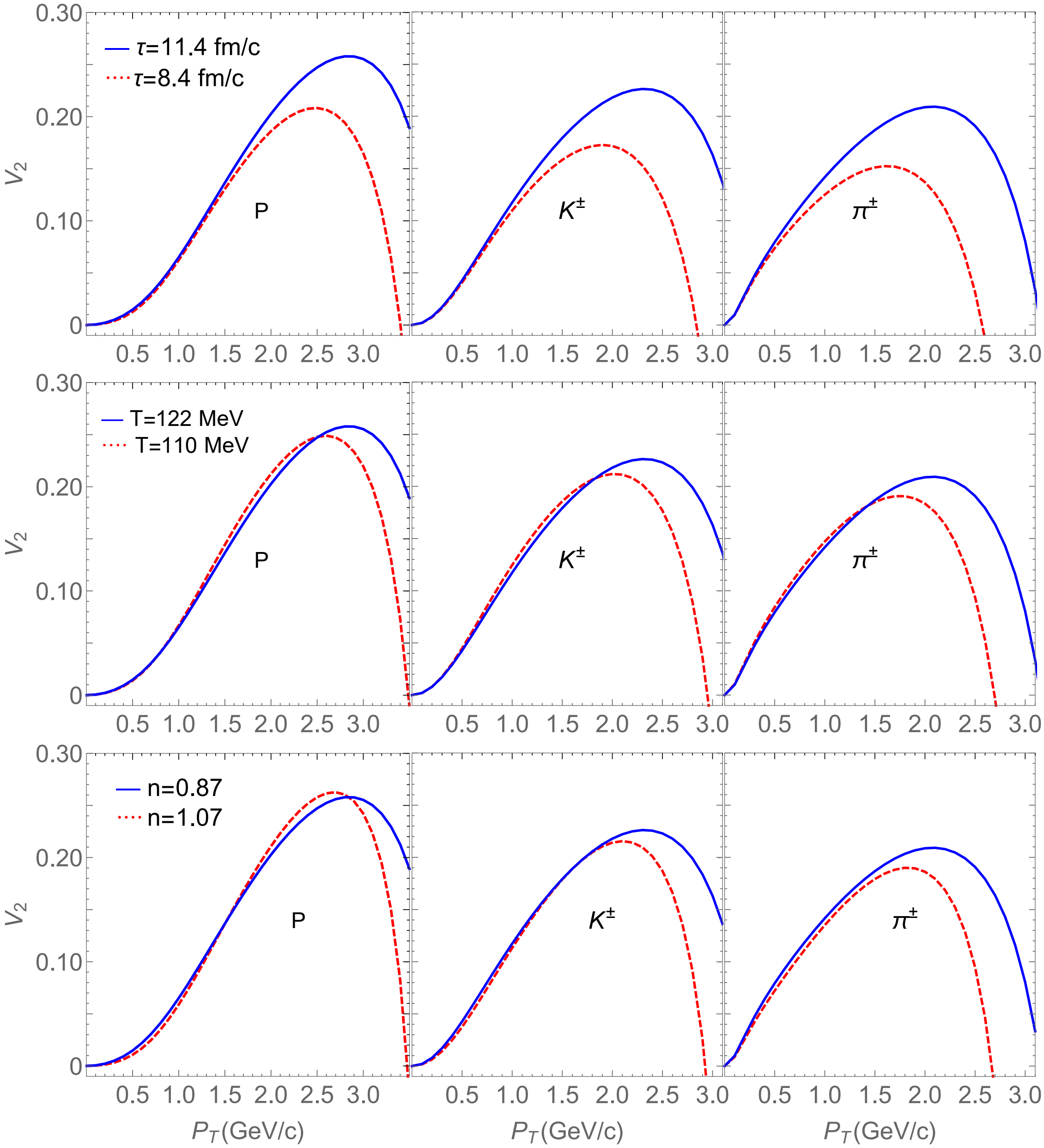

Figure 2.3: Elliptic flow of proton, kaon and pion calculated with varying parameters τ, T and n. The default parameters are the same as used in Fig. 2.1.

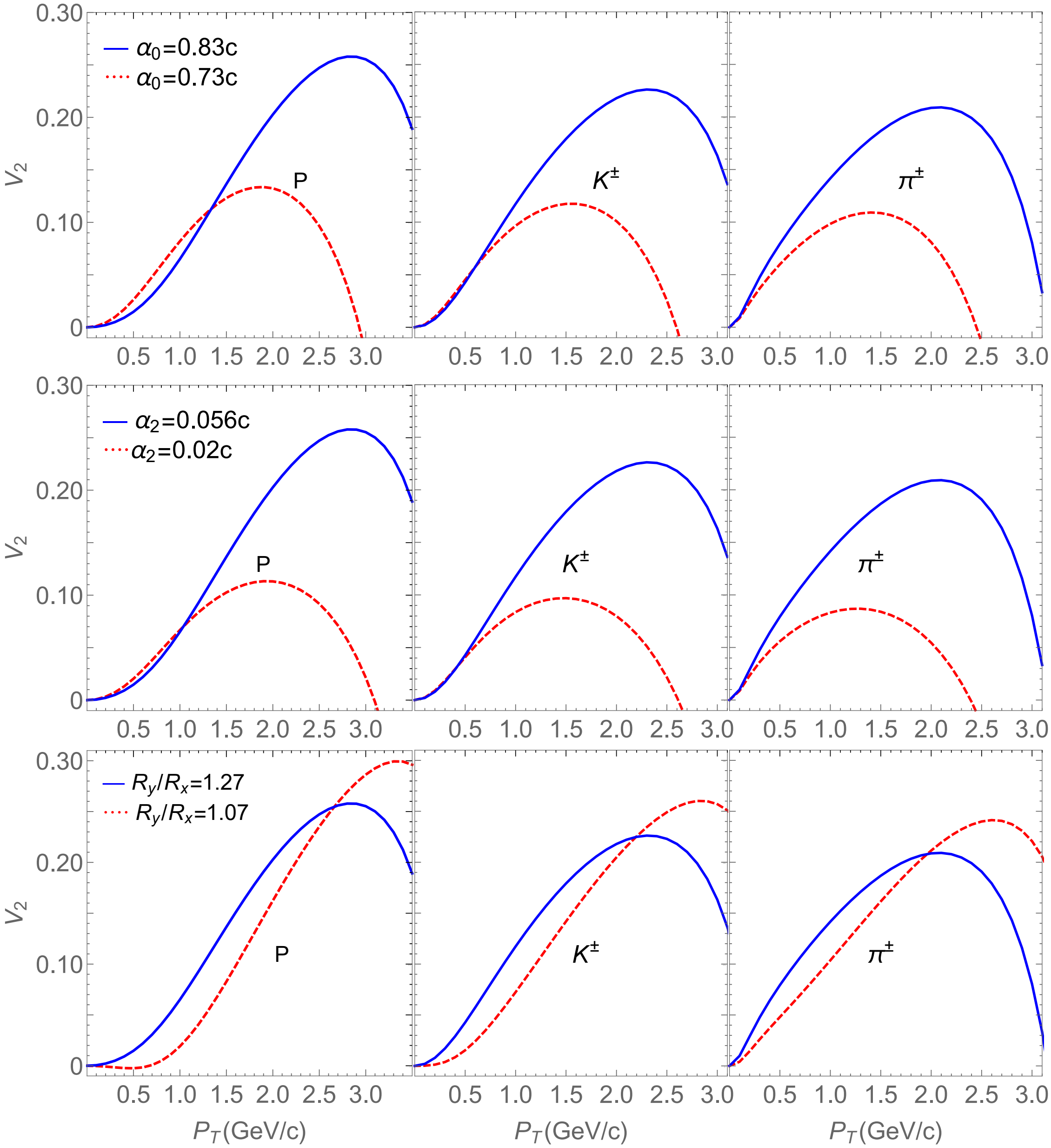

Figure 2.4: Elliptic flow of proton, kaon and pion calculated with varying parameters α_0, α_2 and R_y/R_x. The default parameters are the same as used in Fig. 2.1.

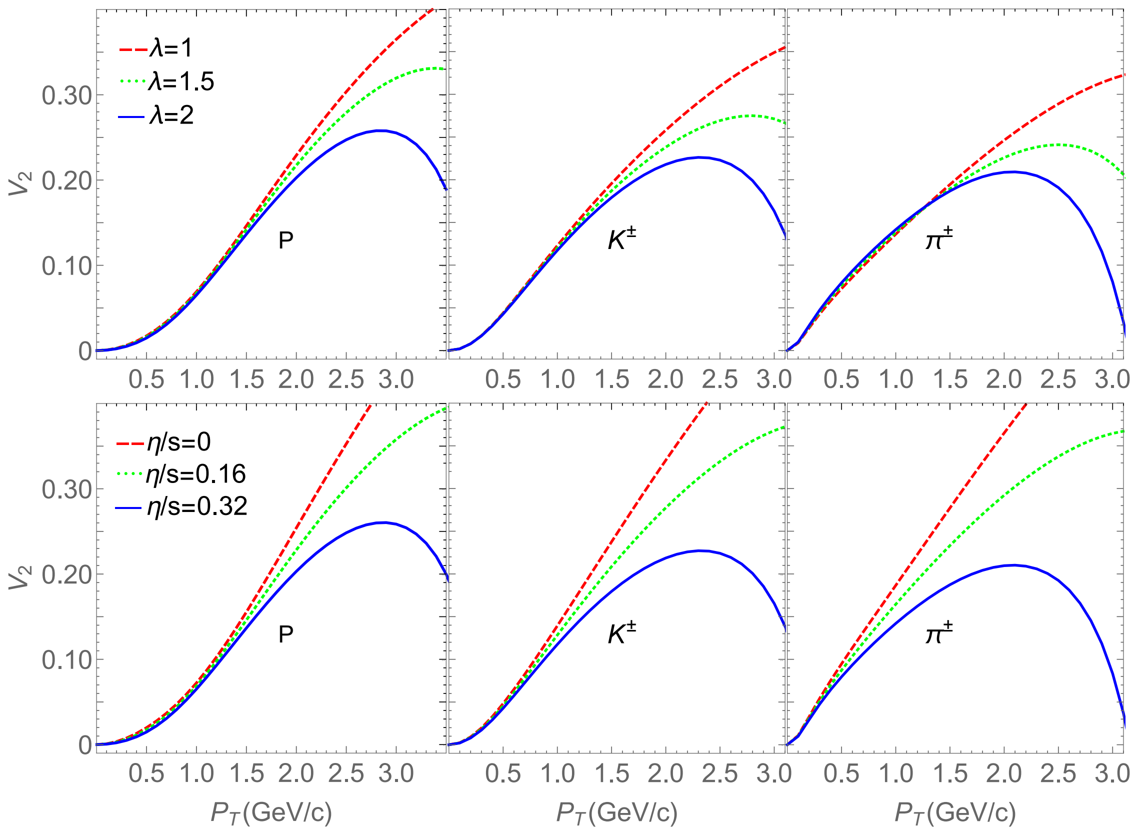

Figure 2.5: Elliptic flow of proton, kaon and pion calculated with varying parameters λ and η/s. The default parameters are the same as used in Fig. 2.1.

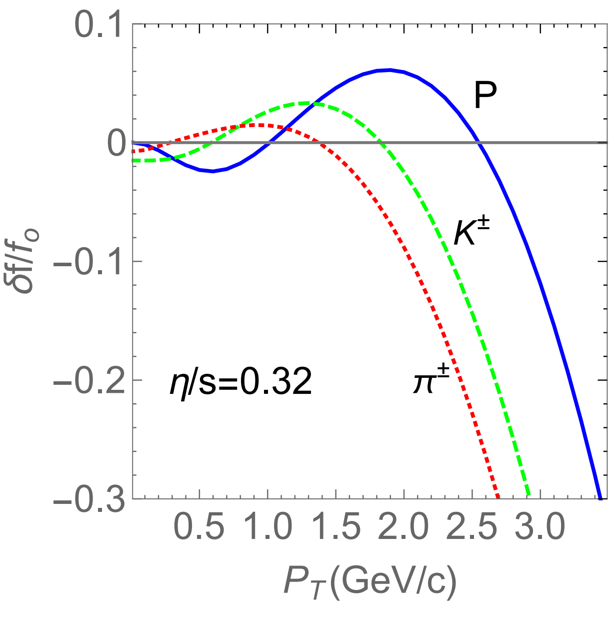

Figure 2.6: The ratio of corrections δf to f_0 for transverse momentum spectra. The default parameters are the same as used in Fig. 2.1.

3. COMPARISON TO HYDRODYNAMICS

Blastwaves have been a simple and effective tool that can be used to parameterize the final state of nuclear collisions. Basic information like the kinetic freeze-out temperature and average radial flow at freeze-out are easily read off from fits to final hadron spectra. However, given the approximations made in blastwave fits, the main question is how well the extracted parameters reflect the actual values. If systematic uncertainties from blastwave fits could be quantified, or systematic deviations could be corrected for, blastwaves would be a more widely accepted tool for quantitative analyses. In this chapter we will start this process of quantification by comparing freeze-out conditions from smooth viscous hydrodynamics to blastwave fits. The global picture is one of two successive approximations

$$\text{experimental data} \succ \text{hydro simulation} \succ \text{blastwave fit}$$

where $\succ$ means "approximated by". There are several approximations in describing the freeze-out process with hydrodynamics [40]. They are briefly discussed here but their quantification is outside the scope of this chapter. Approximations that blastwaves make are discussed in more detail and then quantified in a specific case. We focus here on the accuracy of the extracted freeze-out temperature T_{fo} and the specific shear viscosity η/s at freeze-out. The results from the analysis here can be used directly to improve our extraction of η/s from experimental data in chapter 4.

Here we use the viscous hydrodynamics code MUSIC [15, 68] for this purpose. We generate events at different temperatures and with various specific viscosities with MUSIC. These events use smooth initial conditions and include shear viscosity. Then we extract the flow field from spectra and elliptic flow v_2 of these hydrodynamic calculations with our viscous blastwave. Especially we compare the extracted freeze-out temperature T_{fo} and specific viscosity η/s to values used in hydrodynamics and obtain the mapping matrix between them. By using the mapping matrix, we are able to unfold our blastwave fit results of experiment measurement.

The setup of our hydrodynamic calculations reflects conditions in Au+Au collisions at RHIC as described below, although none of the hydrodynamic calculations in this chapter were fit to data. For comparison to data we refer the reader to chapter 4 and Refs. [15, 68]. We also check several fits to hydrodynamics set up for Pb+Pb collisions at LHC to establish that our results are sufficiently universal for our purposes. We will establish a map in the T_{fo}-η/s-plane from the values for a set of hydrodynamic simulations to the corresponding values extracted from viscous blastwave fits of hydrodynamic spectra and elliptic flow. We are then providing a parameterization of this map and its inverse. The inverse map can be used to unfold the bias from blastwave fits. We will also estimate the uncertainties from this procedure.

This work only presents one specific aspect of a systematic blastwave-hydrodynamics comparison, focusing on a particular range of hydrodynamic initial conditions, and on temperature and specific shear viscosity as observables. However, the results should still be very useful in heavy ion collisions. We also do not attempt to assign how much of the bias and uncertainties we discover are due to particular assumptions in the blastwave. We will only offer a qualitative assessment of the impact of bulk viscous effects.

3.1 Hydro Events Preparation

We use the viscous hydrodynamics code MUSIC to simulate Au-Au collisions at RHIC energies and at different impact parameters. MUSIC is a (3+1)D relativistic second-order viscous hydrodynamics code for heavy ion collisions. It was initially developed at McGill as an ideal (3+1)D hydrodynamic code in 2009 and later extended to include first and second order shear viscous corrections [15, 68]. The work flow is as follows. First, we carry out the hydrodynamic evolution starting from suitable initial conditions. Then we freeze out and finally carry out all resonance decays. MUSIC has many parameters that can be set by the user. For most settings, we use the default values. We choose boost-invariant (2+1)D mode consistent with the blastwave. We use the built-in optical Glauber model as initial conditions and the equation of state (EOS) s95p-v1.2. We include a constant shear viscosity η/s and the default MUSIC bulk viscosity in the evolution. We freeze out at a constant freeze-out temperature T_{fo} and add the shear correction terms δf in the

Cooper-Fry formula consistent with the blastwave. Other MUSIC settings are documented in Tab. 3.1.

Parameter	Set
Target+Projectile	Au+Au
Initial_profile	Optical Glauber model
EOS_to_use	lattice EOS s95p-v1.2 for UrQMD
reconst_type	solve flow velocity for hydro eqns
Maximum energy density	54.0
SigmaNN	42.1
boost_invariant	1
Viscosity_Flag	1
Include_Shear_Visc	1
T_dependent_Shear_to_S_ratio	0
Include_Bulk_Visc	1
Include_second_order_terms	0
Do_FreezeOut	1
freeze_out_method	Schenke's more complex method
use_eps_for_freeze_out	use temperature
pt_steps	36
min_pt	0.01
max_pt	3.0
phi_steps	40
Include_deltaf_in Cooper-Frye formula	1
Inlucde_deltaf_bulk	1

Table 3.1: List of parameter set for MUSIC. 1 and 0 are flags (1 = YES and 0 = NO).

As discussed above, we focus here on the relation of extracted to true temperature and specific shear viscosity. We expect η/s to decrease with temperature in the hadronic phase and T_{fo} increases with impact parameter b. For this study to be useful, we focus on a band in the T-η/s-plane, varying the impact parameter b with T. These choices were guided by fits to RHIC data to be discussed in chapter 4. The values of T and η/s in the center of the band are listed in Tab. 3.2 together with the impact parameter used. From MUSIC output files we extract transverse momentum p_T spectra and elliptic flow v_2 at rapidity y=0 for pions, kaons and protons as our pseudo data. As set in the code, the full p_T range of the pseudo data is from 0 to 3 GeV/c.

b(fm)	5	5	6	6.5	7	8	9	10.5	10.5
T_{fo}(MeV)	105	110	115	120	125	130	135	140	145
$4\pi\eta/s$	6.03	5.28	4.52	3.77	3.02	2.51	2.01	1.51	1.01

Table 3.2: The first set of impact parameter b, freeze-out temperature T_{fo} and shear viscosity η/s for MUSIC hydro runs.

MUSIC	spectra (GeV/c)			v_2 (GeV/c)		
	pion	kaon	proton	pion	kaon	proton
105	0.34-1.95	0.34-2.23	0.76-2.52	0.53-3.0	0.34-3.0	0.34-3.0
110	0.34-2.37	0.34-2.68	0.34-3.0	0.34-3.0	0.34-3.0	0.34-3.0
115	0.34-1.95	0.34-2.23	0.34-2.52	0.34-3.0	0.34-3.0	0.34-3.0
120	0.40-1.95	0.40-2.09	0.34-2.37	0.34-2.84	0.34-3.0	0.34-3.0
125	0.40-1.95	0.40-2.09	0.34-2.37	0.34-2.68	0.34-2.84	0.34-3.0
130	0.46-1.95	0.40-2.09	0.29-2.23	0.34-2.68	0.34-2.68	0.34-2.84
135	0.34-1.82	0.29-1.95	0.24-2.09	0.34-2.52	0.34-2.68	0.34-2.68
140	0.24-1.57	0.20-1.69	0.20-1.82	0.24-2.23	0.53-2.23	0.20-2.37
145	0.24-1.57	0.20-1.69	0.20-1.82	0.24-2.23	0.53-2.23	0.20-2.37

Table 3.3: Fit ranges for different hydro pseudo data.

We will discuss the effect of the choice of fit range on blastwave fits in detail in chapter 4. Here we just summarize the discussion briefly. First, the p_T range can be expanded to higher p_T going from peripheral to central collisions, because thermal particle production dominates up to higher p_T. Note that in pure hydrodynamics all particles are thermal, but we choose our fit ranges to roughly represent the fit ranges appropriate for experimental data discussed in chapter 4. It turns out that elliptic flow can be fitted exceptionally well even at large p_T (> 2 GeV/c) and we make use of this to constrain η/s more effectively. The default fit ranges for events at different T_{fo} are shown in Tab. 3.3.

To do the analysis, we need to assign uncertainties to hydro pseudo data. We assign 5% uncertainty and 2% uncertainty for spectra and v_2 respectively, with a pedestal of 0.002 for v_2 since v_2 vanishes for small p_T. We will vary the uncertainties later on to estimate uncertainties from this choice.

3.2 Bayesian Method

Before we start the analysis, we would like to introduce the statistical tools used. We use the statistical analysis package from the Models and Data Analysis Initiative (MADAI) project [69, 70] to determine fit parameters. The MADAI package includes a Gaussian process emulator and a Bayesian analysis tool. It works as follows. First, we choose prior ranges for each parameter with flat probabilities and generate a set of training points in parameter space. Second, we calculate all fitted observables at each training point. The package then builds a Gaussian process emulator, which can estimate observables for random parameter values. Finally a Markov Chain Monte Carlo provides a likelihood analysis and gives the maximum likelihood parameters and uncertainties.

As a general strategy we often start with a very wide prior range and narrow it down subsequently for better resolution. In order to guarantee the accuracy of the Gaussian emulator, the prior range should not be too wide and the number of training points needs to be large enough for the chosen number of parameters. Our final prior ranges have $\Delta T \approx$ 15 MeV, $\Delta\eta/s \approx 2/(4\pi)$ and use $N = 500$ training points for the Gaussian process emulator. As an example, the final prior range for this T-η/s choice is shown in Table. 3.4.

parameter	prior range
T(GeV)	0.111 – 0.123
$\alpha_0(c)$	0.73 – 0.78
R_y/R_x	1.07 – 1.13
$\alpha_2(c)$	0.037 – 0.057
$4\pi\eta/s$	1.5 – 3.5

Table 3.4: Prior range for MUSIC event $T = 130$ MeV, $\eta/s = 2.51/(4\pi)$.

We can check the quality of the Gaussian emulator by comparing the predicted values and the actual calculation. For example, we can pick a random set of parameters: $T = 115$ MeV, $\alpha_0 = 0.75c$, $R_y/R_x = 1.1$, $\alpha_2 = 0.05c$, $\eta/s = 2/(4\pi)$ and ask the Gaussian emulator to make a prediction. Using the same parameters, we also calculate the spectra and v_2 directly from the blastwave. We find the accuracy of the emulator to be extremely good, i.e. the results of the Gaussian emulator are identical with the true blastwave results within $\leq 1\%$ accuracy. The only exception is for elliptic flow at large p_T where deviations read a few percent. Fig. 3.1 and 3.2 demonstrate the accuracy of our Gaussian emulator for this example.

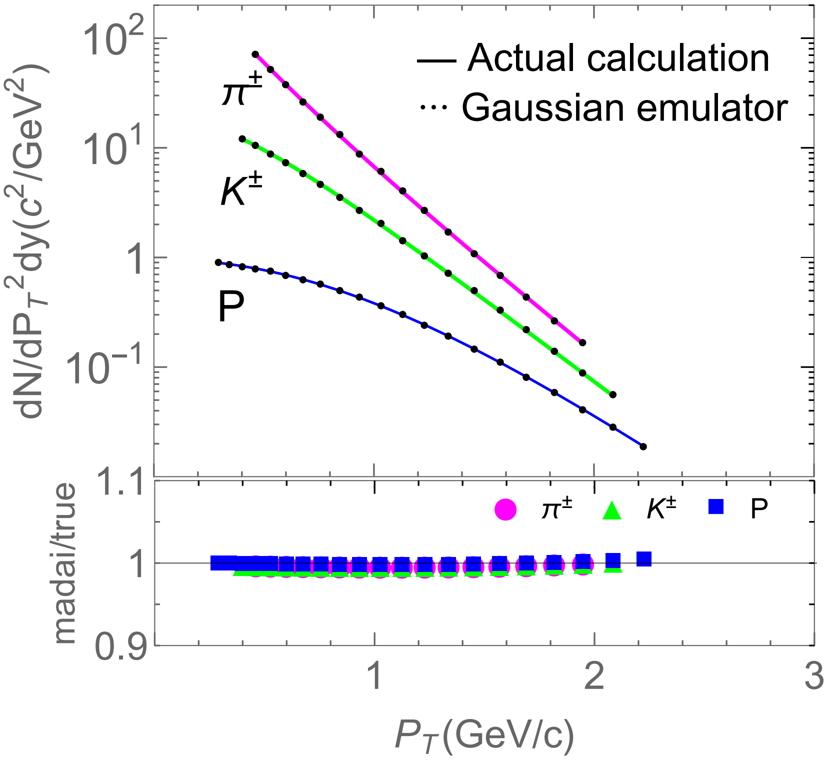

Figure 3.1: Comparing the predicted values from the Gaussian emulator and the actual blastwave calculation for the spectra of π, $\mathbf{K}$, $\mathbf{p}$. Parameters are given in the text.

The blastwave computation Eq. (2.19) is carried out by a short program in C language. A single computation of Eq. (2.19) is quite fast and takes about 1 minute for one particle at 30 different p_T values. For the task of training the Gaussian process emulator, we use the Brazos Cluster of Texas A&M University to complete it. Once the Gaussian process emulator is built, the full statistical analysis runs easily on a single CPU.

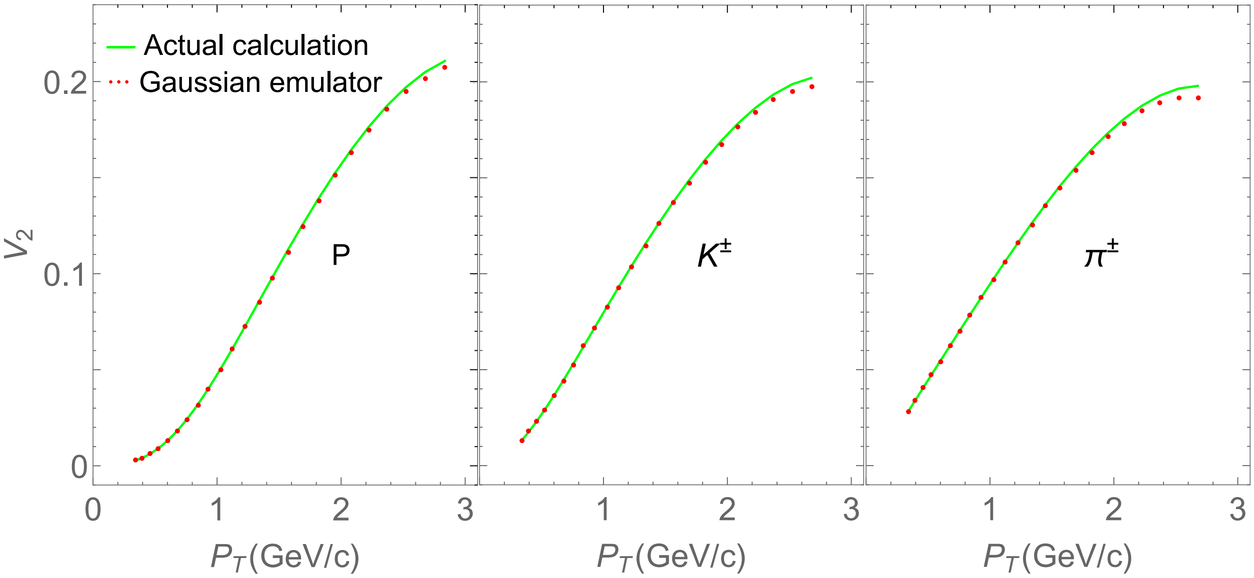

Figure 3.2: Comparing the predicted values from the Gaussian emulator and the actual blastwave calculation for elliptic flow of π, $\mathbf{K}$, $\mathbf{p}$. Parameters are given in the text.

3.3 Blastwave Fit

The parameters used in the blastwave fit to hydro pseudo data are $(\tau, T, R_y/R_x, n, \alpha_0, \alpha_2, \eta/s)$. Chemical potentials μ are set to zero in MUSIC. We will ultimately only use T and η/s in this analysis. We fix the parameters n and τ by choosing values close to those extracted from RHIC data in chapter 4. The values can be found in Tab. 3.5. Later we will estimate the uncertainty of this choice by varying n.

As an example, we discuss here the MUSIC event T = 130 MeV, $\eta/s = 2.5/(4\pi)$ in detail. Fig. 3.3 shows the result from the statistical analysis for the chosen fit range of this data set; see Tab. 3.3. The horizontal and vertical axes show the chosen prior ranges for the parameters. From left to right (top to bottom): T (MeV), α_0, R_y/R_x, α_2, η/s. Plots on the diagonal show posterior likelihood distributions. The off-diagonal plots show correlations between parameters. The correlations on the off-diagonal plots are important since they demonstrate the connections between parameters. Besides, they also help to verify the Gaussian emulator. Only when we have the correct correlations, the statistical analysis becomes reliable. For example, the negative correlation

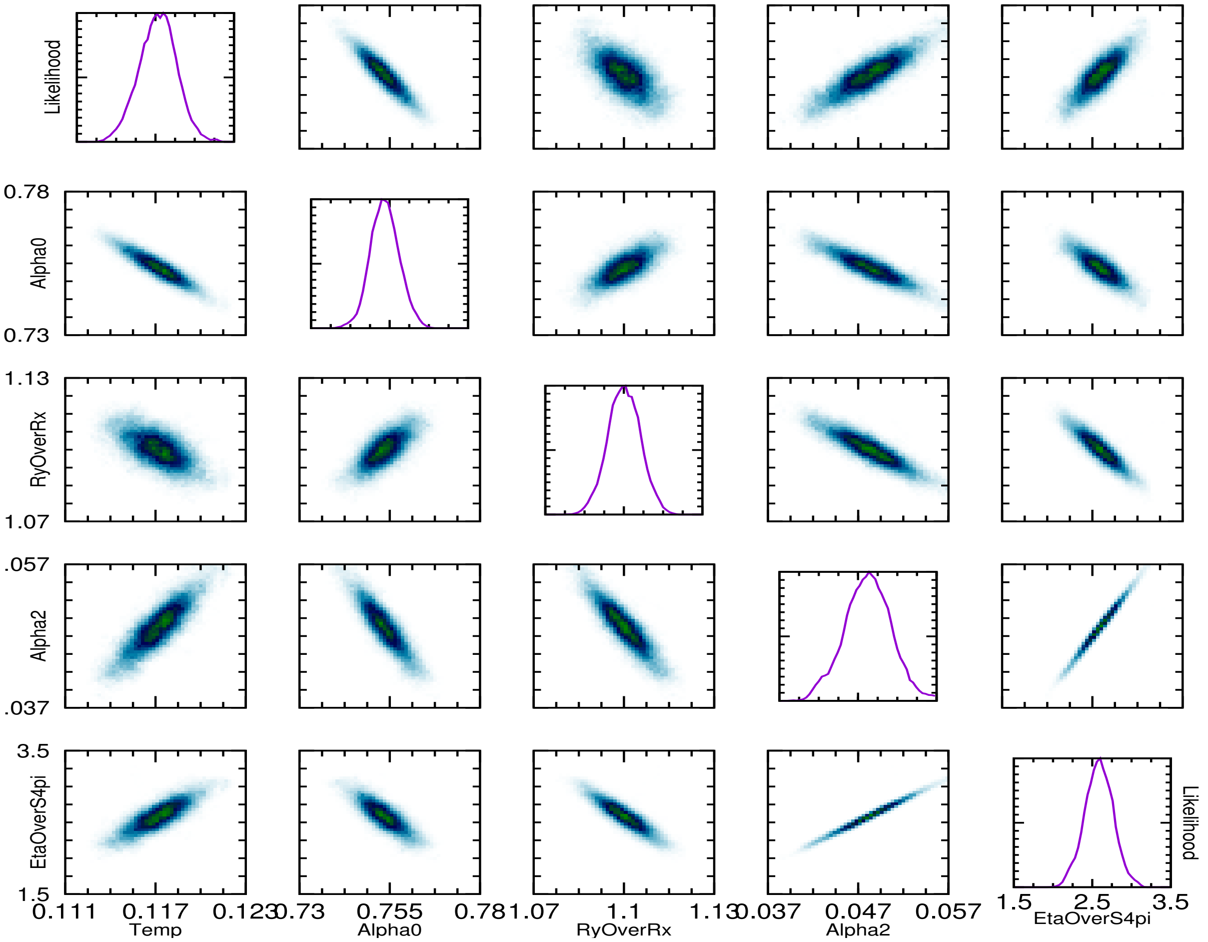

Figure 3.3: Likelihood analysis for MUSIC event $T = 130$ MeV, $\eta/s = 2.5/(4\pi)$ provided by the MADAI package. The diagonal show posterior likelihood distributions. The off-diagonal plots show correlations between parameters.

between T and α_0 shows the fact that increasing T makes the spectra softer and decreasing α_0 makes it steeper. The positive correlation between α_2 and η/s shows the fact that increasing α_2 makes the elliptic flow larger and increasing η/s makes it smaller.

The likelihood plots on the diagonal of Fig. 3.3 show well defined peaks. Based the output of the MADAI package, the preferred (average) values for MUSIC event T = 130 MeV are, T=117 MeV, α_0=0.753c, R_y/R_x=1.10, α_2=0.048c, η/s=2.6/4π ($\tau = 8.4$ fm/c and n=0.88 are fixed in this case). We proceed for the other T-η/s points in Tab. 3.2 analogously.

The extracted parameter values for MUSIC pseudo data in different freeze-out temperature are

MUSIC	τ (fm/c)	T (MeV)	α_0/c	n	R_y/R_x	α_2/c	$4\pi\eta/s$
105	12.2	111	0.824	0.86	0.99	0.021	5.8
110	11.4	114	0.822	0.87	1.01	0.021	5.4
115	10.6	113	0.833	0.81	1.04	0.025	4.7
120	9.8	114	0.820	0.84	1.06	0.028	3.8
125	9.1	118	0.786	0.88	1.08	0.037	3.0
130	8.4	117	0.753	0.88	1.10	0.048	2.6
135	7.8	120	0.715	0.92	1.15	0.059	2.1
140	7.2	123	0.654	0.96	1.27	0.069	1.6
145	6.8	126	0.604	1.00	1.35	0.080	1.2

Table 3.5: Extracted parameter values for different MUSIC pseudo data. Note: τ and n are fixed and not obtained by fitting.

shown in Tab. 3.5. We can plug these parameters into our blastwave and calculate the spectra and v_2, then compare to the hydro calculation. The plots of spectra and v_2 for MUSIC in different freeze-out temperature are shown in Fig. 3.4 and Fig. 3.5. We find blastwave calculations agree very well with hydro pseudo data within a few percentage error.

Now we shall analyze the uncertainty of our extracted values. The uncertainty mainly comes from 3 sources: (i) uncertainty due to a fixed value of n; see Tab. 3.6, (ii) uncertainty due to the uncertainties assigned to MUSIC pseudo data; see Tab. 3.7 and (iii) uncertainty from the Gaussian emulator and likelihood analysis; see Fig. 3.3. From Tab. 3.6 we find that T varies within a few MeV and η/s becomes larger when using smaller n. From 3.7 we find T varies within a few MeV and η/s does not change much when using different uncertainties assigned to MUSIC pseudo spectra data. From Fig. 3.3 we can read the uncertainty from the likelihood analysis. In general, the influence of these variations on the extracted values are moderate and we will treat them as independent uncertainties and add them quadratically.

The final extracted freeze-out temperature and viscosities for the points from Tab. 3.2 are shown in Fig. 3.6 with their combined uncertainties. We find that the extracted specific shear viscosities are mostly consistent with true values within uncertainties. However the extracted temperature is distorted and it underestimates the true temperature significantly at high T. The extracted T_{fo}

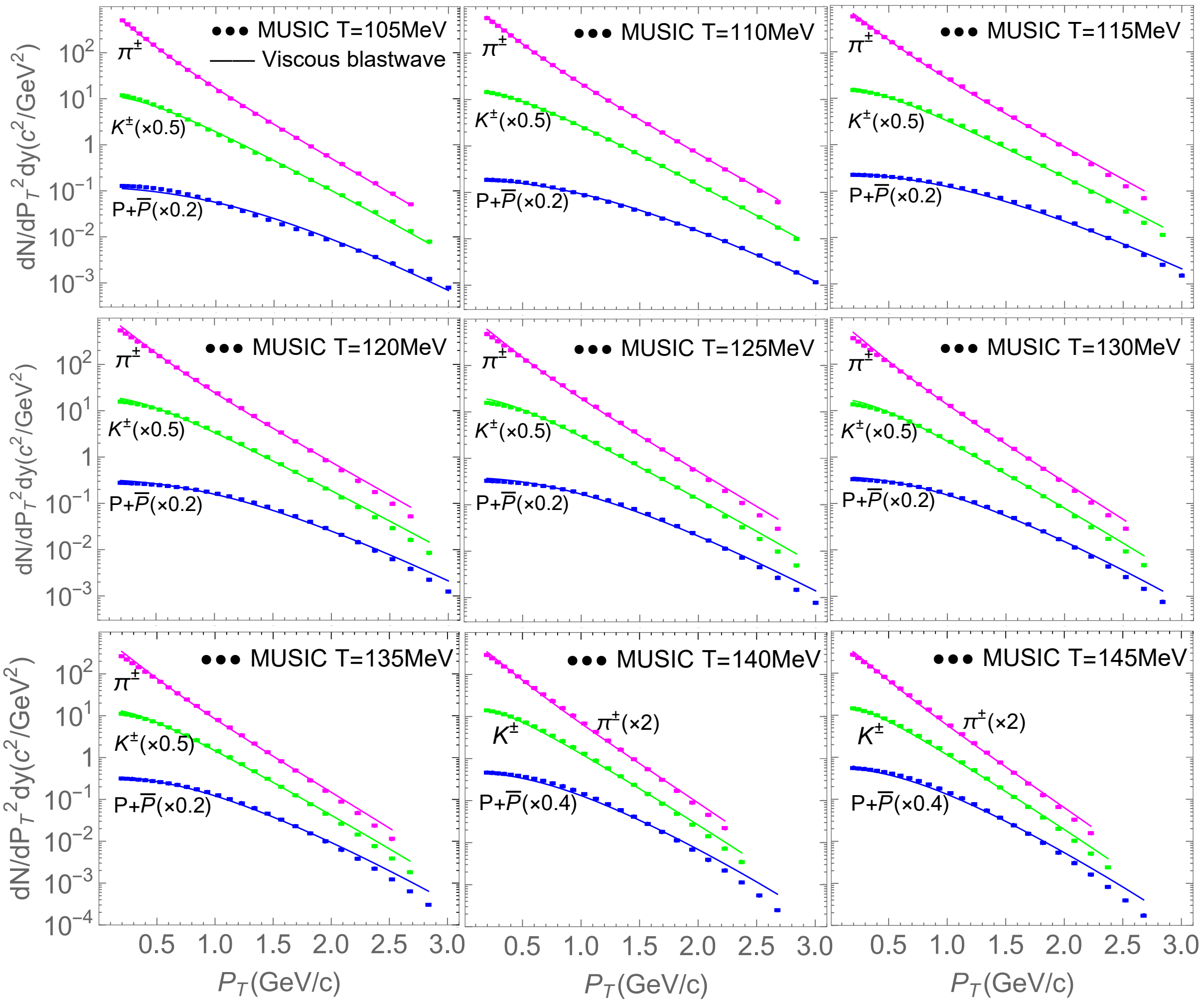

Figure 3.4: Transverse momentum spectra for MUSIC pseudo data in different freeze-out temperature T. Solid lines are blastwave calculations using extracted paramteres.

is about 15 MeV low for hydro events at high temperature (or peripheral collisions). For events at low freeze-out temperature (or central collisions), the extracted $T_{\rm fo}$ are very close to the true temperature within ±5 MeV. We also notice the uncertainty is much larger for hydro events at low freeze-out temperature than events at high temperature. Low T seem to have large uncertainties because they are very sensitive to changing n.

3.4 Mapping Hydro Event onto Blastwave

Once we extract parameters through blastwave, the next step is to build a map $(T, \eta/s)_{\rm hydro} \rightarrow (T, \eta/s)_{\rm bw}$ so that we can map temperature and viscosity of "true" hydro events onto blastwave fits.

MUSIC	small n			large n		
	n	T(MeV)	$4\pi\eta/s$	n	T(MeV)	$4\pi\eta/s$
105	0.81	109.3	6.73	0.91	113.0	4.77
110	0.82	112.2	6.71	0.92	116.1	4.25
115	0.76	111.5	5.90	0.86	113.2	3.31
120	0.79	114.1	4.52	0.89	113.7	2.93
125	0.83	118.2	3.62	0.93	117.2.	2.38
130	0.83	116.4	3.26	0.93	117.8	1.81
135	0.87	120.5	2.45	0.97	120.5	1.75
140	0.91	122.8	1.75	1.01	122.7	1.33
145	0.95	126.3	1.34	1.05	126.4	1.10

Table 3.6: The extracted values of T and η/s for different n. We vary the values of n by adding or subtracting 0.05 from the default ones.

MUSIC	4% uncertainty		6% uncertainty	
	T(MeV)	$4\pi\eta/s$	T(MeV)	$4\pi\eta/s$
105	112.4	5.92	108.7	4.92
110	114.4	5.54	114.0	5.43
115	111.8	4.49	113.0	4.67
120	112.9	3.61	114.9	3.83
125	117.3	3.01	118.4	3.07
130	116.2	2.43	117.8	2.62
135	120.2	2.08	120.8	2.12
140	124.2	1.60	122.0	1.52
145	127.4	1.24	125.2	1.19

Table 3.7: The extracted values of T and η/s for different uncertainties assigned to MUSIC pseudo spectra data. The uncertainty for v_2 is 2% with a pedestal 0.002. The uncertainty for spectra is changed to 4% and 6% as shown in the table.

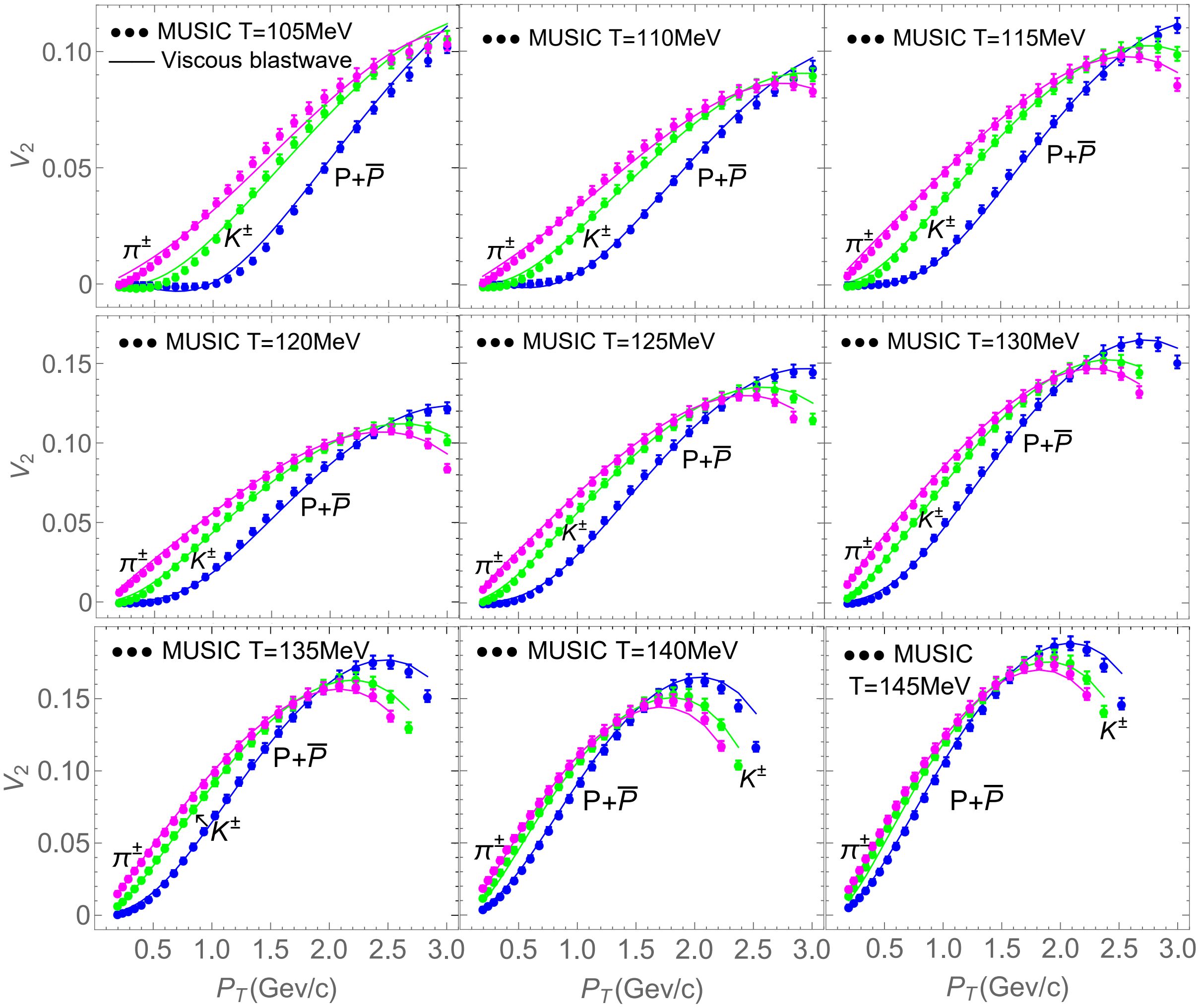

Figure 3.5: Elliptic flow v_2 for MUSIC pseudo data in different freeze-out temperature T. Solid lines are blastwave calculations using extracted paramteres.

To do that, first we write input and fit results in matrix form in $(T, \eta/s)$-space

$$A^T = \begin{bmatrix} 105 & 110 & 115 & 120 & 125 & 130 & 135 & 140 & 145 \\ 6.03 & 5.28 & 4.52 & 3.77 & 3.02 & 2.51 & 2.01 & 1.51 & 1.01 \end{bmatrix}$$

$$B^T = \begin{bmatrix} 111.2 & 114.0 & 112.7 & 113.9 & 117.7 & 117.2 & 120.0 & 123.0 & 126.3 \\ 5.83 & 5.43 & 4.67 & 3.75 & 3.01 & 2.59 & 2.07 & 1.55 & 1.23 \end{bmatrix}$$

here A, B are the matrices of MUSIC and blastwave results respectively. The first column is the

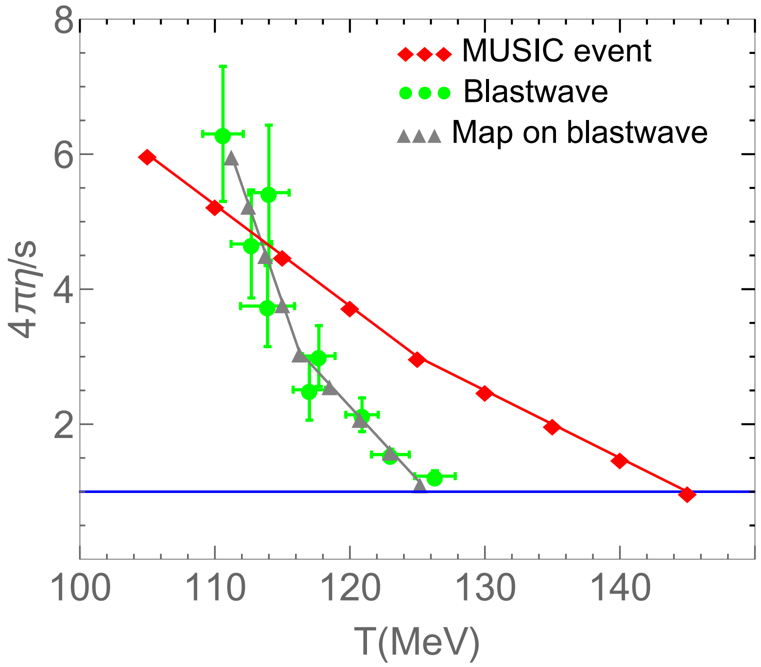

Figure 3.6: Comparison of extracted freeze-out temperature and shear viscosity from blastwave and values used in MUSIC events. Gray line shows the values of mapping MUSIC parameters using our matrix parameterization.

freeze-out temperature in MeV and the second column is the specific shear viscosity in units of $1/4\pi$. It turns out that a linear map between A and B has sufficient accuracy for our purpose. Now the issue becomes a simple math problem, i. e. , we need to find a transformation matrix M so that

$$\begin{pmatrix} T \\ \eta/s \end{pmatrix}_{\text{bw}} \approx M \begin{pmatrix} T \\ \eta/s \end{pmatrix}_{\text{hydro}} \tag{3.1}$$

or in $(T, \eta/s)$-space

$$B^T \approx MA^T \tag{3.2}$$

where M is a 2×2 matrix. We write $\approx$ because the equation for M is over-determined and we look for the optimal approximate solution. Multiplying from the right with A yields

$$B^T A = MA^T A \tag{3.3}$$

The solution of the new equation is the approximation of the original one and its existence is guaranteed. The solution is

$$M = \begin{bmatrix} 0.8365 & 3.90 \\ 0.0011 & 0.98 \end{bmatrix}$$

Using this M, we can calculate the values $B' = (MA^T)^T$ and compare with the target results B. This is shown in Fig. 3.6. The map M describes the fitted values rather well within uncertainties. In other words, the matrix M is a good approximation of the mapping of hydro events onto blastwave.

We rewrite Eq. (3.2) as

$$A^T = M^{-1} B^T \tag{3.4}$$

where the inverse of matrix M maps the blastwave onto hydro event

$$M^{-1} = \begin{bmatrix} 1.2017 & -4.78 \\ -0.0013 & 1.03 \end{bmatrix} .$$

We will use this inverse map below.

To validate matrix M, we generate two more sets of MUSIC pseudo data and extract their blastwave parameters; see Tab. 3.8 and Tab. 3.9. They are generated by increasing and decreasing η/s compared to Tab. 3.2 to create a band in T-η/s space. We then solve the mapping equation Eq. (3.3) and finally obtain matrices M_2 and M_3.

MUSIC	T (MeV)	105	110	115	120	125	130	135	140	145
	$4\pi\eta/s$	5.28	4.52	3.77	3.02	2.51	2.01	1.51	1.01	0.05
Blastwave	T (MeV)	110.7	113.8	111.9	113.4	118.5	117.5	121.4	124.6	128.4
	$4\pi\eta/s$	5.23	4.79	3.73	3.14	2.84	2.36	1.55	1.10	0.60

Table 3.8: Second set of MUSIC events, using the same impact parameters and freeze-out temperature as Tab. 3.2 but with smaller viscosity. The T_{fo} and η/s extracted from blastwave are also shown.

MUSIC	T (MeV)	105	110	115	120	125	130	135	140	145
	$4\pi\eta/s$	6.79	6.03	5.28	4.52	3.77	3.02	2.51	2.01	1.51
BlastWave	T (MeV)	111.9	114.4	113.0	113.8	118.2	117.6	120.7	123.7	124.4
	$4\pi\eta/s$	6.50	6.11	5.21	4.06	3.62	2.78	2.55	1.80	1.44

Table 3.9: Third set of MUSIC events, using the same impact parameters and freeze-out temperature as Tab. 3.2 but with larger viscosity. The T_{fo} and η/s extracted from blastwave are also shown.

$$M_2 = \begin{bmatrix} 0.8611 & 3.81 \\ 0.0012 & 1.00 \end{bmatrix} \qquad M_3 = \begin{bmatrix} 0.8227 & 3.75 \\ -0.0007 & 0.99 \end{bmatrix}$$

We observe that M_2 and M_3 are very close to M. Again using M_2 and M_3, we can calculate the values $B' = (M_{2,3}A^T)^T$ and compare with the target results B. This is shown in Fig. 3.7 and 3.8. The map $M_{2,3}$ describes the fitted values rather well within uncertainties. We will use M_2 and M_3 below to help estimate uncertainties.

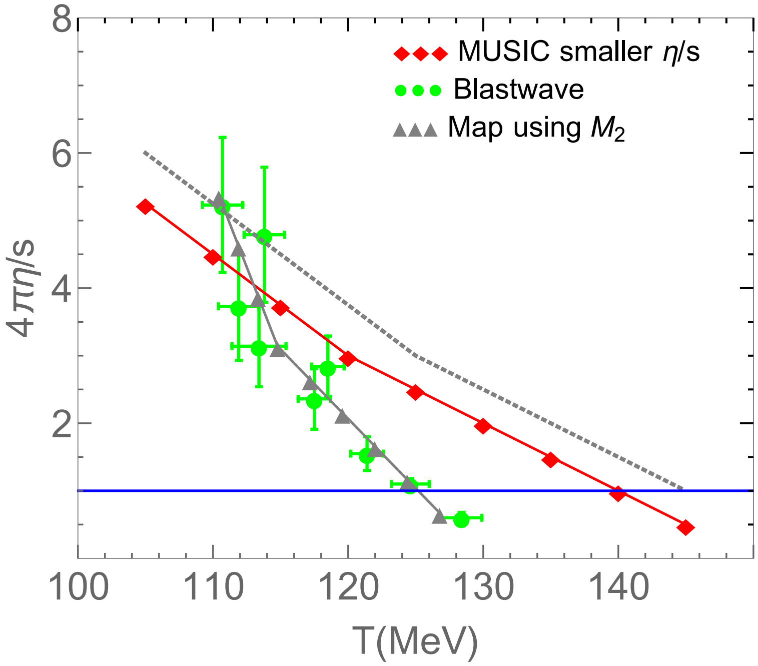

Figure 3.7: Comparison of extracted freeze-out temperature and shear viscosity from blastwave and values used in MUSIC event set 2. Dotted line is MUSIC set 1.

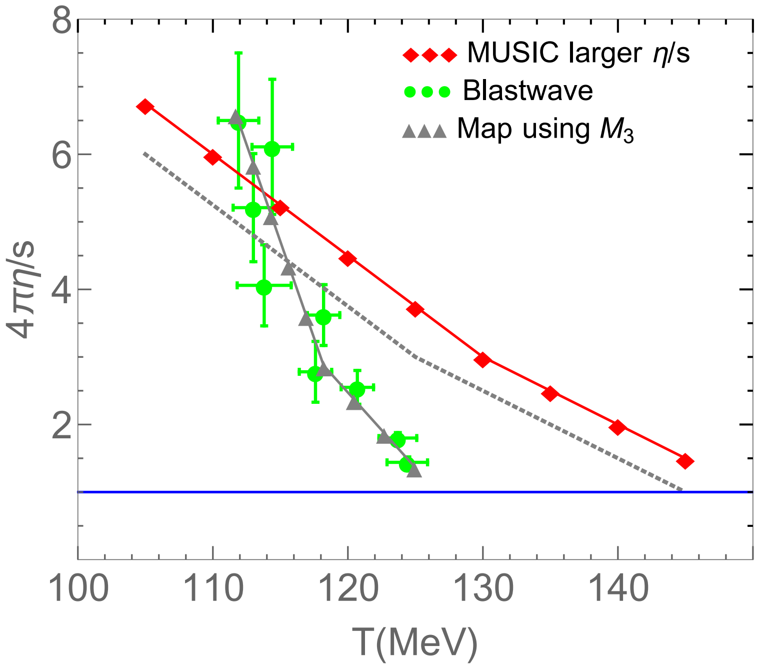

Figure 3.8: Comparison of extracted freeze-out temperature and shear viscosity from blastwave and values used in MUSIC event set 3. Dotted line is MUSIC set 1.

For completeness, we have also run a similar analysis for hydrodynamics pseudo data created for Pb+Pb collisions at LHC energies. We use the same T-η/s points as given in Tab. 3.2 with slightly different impact parameters. We find consistent extracted freeze-out temperature and shear viscosity from blastwave. For example, for hydro event $(T, \eta/s)$ = (125 MeV, 3.0/4π), we extract $(T, \eta/s)$ = (118 MeV, 3.0/4π) for Au+Au collisions and $(T, \eta/s)$ = (122 MeV, 3.3/4π) for Pb+Pb collisions. For hydro event $(T, \eta/s)$ = (140 MeV, 1.5/4π), we extract $(T, \eta/s)$ = (123 MeV, 1.6/4π) for Au+Au collisions and $(T, \eta/s)$ = (127 MeV, 1.5/4π) for Pb+Pb collisions.

There are few MeV differences for the extracted freeze-out temperature and little differences for extracted shear viscosity. We obtain the map matrix M_{Pb} for Pb+Pb collisions at LHC energies and find M_{Pb} to be consistent with M, within the uncertainties already estimated for M. As a first step, we choose the matrix M here as an universal mapping matrix to be applied to both RHIC and LHC data. In the future, we would like to check the dependence of mapping on particle species and collision energies in more detail.

3.5 Unfolding Experimental Fit Results

The blastwave fit results for LHC and RHIC measurements will be presented in detail in chapter 4. We argue that there are systematic biases introduced by the simplistic freeze-out hypersurface and flow field, which can be quantitatively estimated and removed by comparing with hydrodynamics. Suppose we have extracted values $(T, \eta/s)_{data}$ using a blastwave fit, we can use the map from previous section to undo the bias:

$$\begin{pmatrix} T \\ \eta/s \end{pmatrix}_{\text{true}} \approx M^{-1} \begin{pmatrix} T \\ \eta/s \end{pmatrix}_{\text{data}} \tag{3.5}$$

The "true" here refers to values that could have been inferred using hydrodynamic calculations. Of course it still would suffer from shortcomings of a hydrodynamic treatment of freeze-out, which is beyond the scope of this work. As shown in chapter 4, we extract T and η/s from data with assigned Gaussian uncertainties. The 1-σ region before unfolding is given by an ellipse

$$\frac{(x'-a')^2}{\sigma_1^2} + \frac{(y'-b')^2}{\sigma_2^2} = 1 \tag{3.6}$$

where the x-axis is T, the y-axis is η/s, (a', b') is the central value and σ_1, σ_2 are the corresponding Gaussian uncertainties. Assuming x and y are values after unfolding, then

$$\begin{bmatrix} x \\ y \end{bmatrix} = M^{-1} \begin{bmatrix} x' \\ y' \end{bmatrix} = \begin{bmatrix} 1.2017 & -4.78 \\ -0.0013 & 1.03 \end{bmatrix} \begin{bmatrix} x' \\ y' \end{bmatrix} . \tag{3.7}$$

The ellipse in the original data is mapped onto another ellipse around $(a, b) = (1.2017a' - 4.78b', -0.0013a' + 1.03b')$.

Using $(x', y')^T = M(x, y)^T$, we can express x', y' in terms of x, y and plug them into Eq. (3.6), then obtain the expression for the image of the original ellipse

$$\frac{(0.8365x + 3.90y - a')^2}{\sigma_1^2} + \frac{(0.0011x + 0.98y - b')^2}{\sigma_2^2} = 1\,. \tag{3.8}$$

When written in standard form

$$c_1(x-a)^2 + c_2(x-a)(y-b) + c_3(y-b)^2 = 1 \tag{3.9}$$

We recognize it indeed as an ellipse with center (a, b). By doing this, the initial uncertainties can be mapped to the $(T, \eta/s)_{true}$ plane. Note however that the main axes of the new ellipse are no longer along the x and y-axes, see Fig. 3.9.

We also need to consider the effects of uncertainties in the mapping matrix M. Recall that we have obtained three maps M, M_2, M_3 representing the band in the $(T, \eta/s)$ plane. We will interpret the alternative unfolded results using M_2 and M_3 as indications of an average expected uncertainty in M; see Fig. 3.9. The combined distribution is given by

$$f(x,y) = \int f_1(x - x_0, y - y_0) f_2(x_0 - a, y_0 - b) dx_0 dy_0 \tag{3.10}$$

where f_1 is the Gaussian distribution calculated from matrix M, f_2 is a Gaussian distribution of center around (a, b) inferred from M_2, M_3. The integral Eq. (3.10) gives a Gaussian distribution representing combined errors from the data analysis and unfolding.

The results of unfolding the main result of chapter 4 are shown in Fig. 3.10. From Fig. 3.10, we can see the uncorrected extracted temperature is roughly between 110 MeV to 140 MeV with η/s reaching the proposed lower bound at the latter temperature. After correcting the bias, our extracted η/s reach the proposed lower bound around the pseudo critical temperature T_c. Overall these results together are consistent with the idea of a minimum of the specific shear viscosity around T_c.

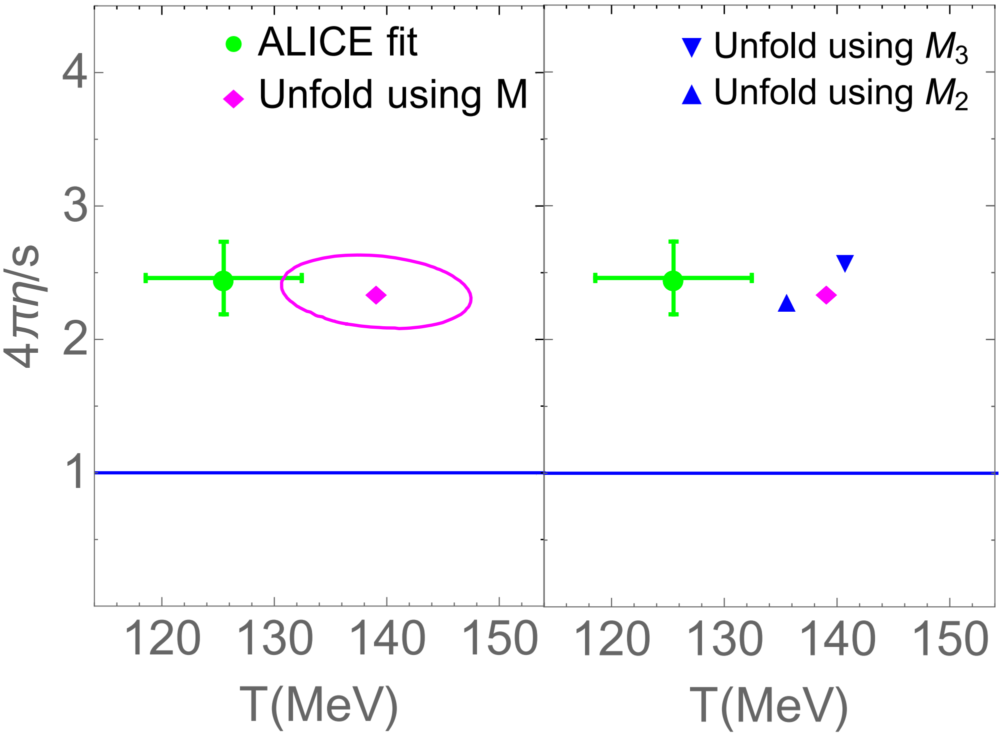

Figure 3.9: Example for the unfolding of a blastwave fit result. The left panel shows initial data points and uncertainty mapped using the inverse of M. The right panel shows the variance in the center value due to slight variations in the mapping matrix. Example is the ALICE 40-50% fit result, T= 126 MeV and $4\pi\eta/s$= 2.5 with uncertainties σ_T= 7 MeV and σ_η= 0.24.

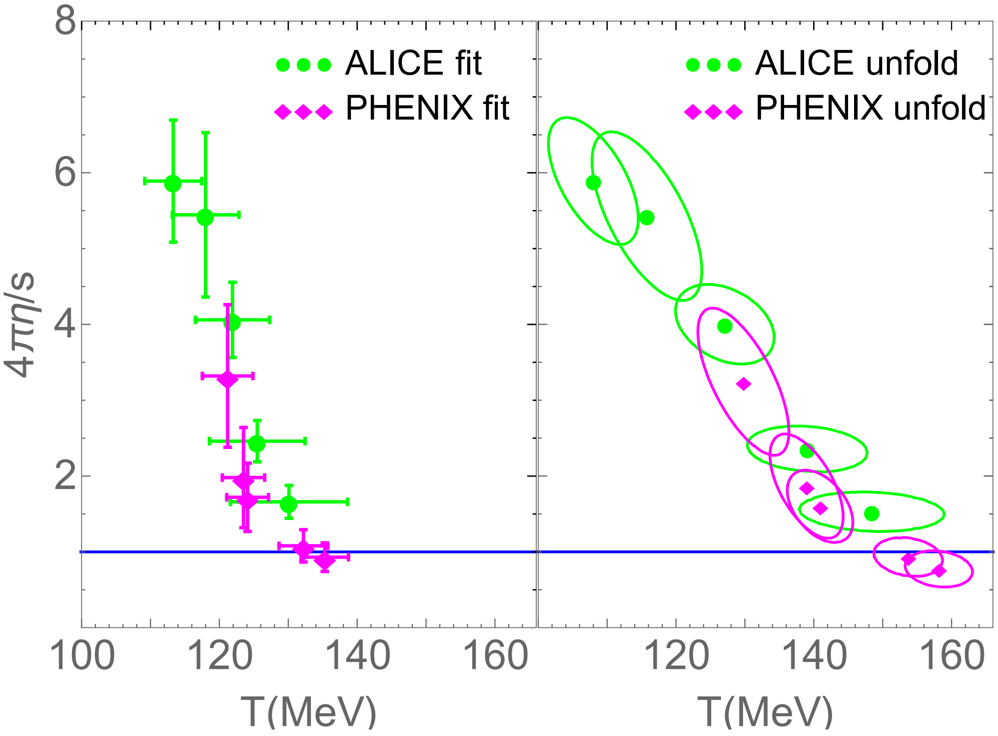

Figure 3.10: Specific shear viscosity η/s at corresponding kinetic freeze-out temperature T extracted from ALICE and PHENIX before removing blastwave bias (left panel) and final values after unfolded (right panel).

4. EXTRACTION OF THE SHEAR VISCOSITY OF HOT HADRONIC MATTER *

In this chapter, we use the viscous blastwave to extract the specific shear viscosity η/s of hot hadronic matter at the kinetic freeze-out T_{fo}. The main effect of the time evolution of the system before freeze-out is the build-up of a flow field u^μ which leads to the system expanding and cooling. Viscous corrections to first order are given by gradients of the flow field. Computing the flow field in fluid dynamics introduces additional dependences on initial conditions and the equation of state. Using a blastwave, we can *fit* the final flow field, together with the temperature and system size at kinetic freeze-out. The specific shear viscosity is then a parameter at just one fixed temperature T_{fo} and a set of chemical potentials $\mu_{\text{fo}} = (\mu_B, \mu_\pi, \ldots)$.

Such an extraction is complementary to fluid dynamics, which integrates over the effects of shear viscosity over a wide temperature range. Some of the uncertainties in both approaches are the same. For example, the assumption of a sharp kinetic freeze-out at a fixed temperature is common to both approaches and is only an approximation. Other uncertainties are different in both approaches. For example, the dependence of fluid dynamic calculations on initial conditions, which themselves are not well constrained experimentally [12], is not present in our approach. We will discuss these uncertainties in more detail below.

Here we present the results for Au+Au collisions at top RHIC energies and Pb+Pb collisions at LHC where the baryon chemical potential vanishes $\mu_B \approx 0$. However, non-vanishing chemical potentials μ_π, μ_K and μ_p are present at kinetic freeze-out, determined by the chemical freeze-out at higher temperatures.

4.1 Data Selection

The viscous blastwave has already been presented in chapter 2. We carry out the analysis using data on identified protons and antiprotons, kaons and pions from LHC and RHIC. We utilize both transverse momentum spectra around mid-rapidity, and elliptic flow v_2, the leading harmonic

---

*Part of this chapter is reprinted with permissions from "Extraction of the Specific Shear Viscosity of Hot Hadron Gas" by Zhidong Yang and Rainer J. Fries, 2018, *preprint*, arXiv:nucl-th/1807.03410, Copyright 2018 by arXiv.

deformation of the spectrum in azimuthal momentum space angle θ in the transverse plane, as functions of hadron transverse momentum p_T. They are calculated from Eq. (2.19) as

$$\begin{aligned} \frac{dN}{2\pi p_T dp_T dy} &= \frac{1}{2\pi}\int d\theta \frac{dN}{dy d^2 p_T}\,, && (4.1) \\ v_2(p_T) &= \left(\frac{dN}{2\pi p_T dp_T dy}\right)^{-1} \frac{1}{2\pi}\int d\theta \cos(2\theta)\frac{dN}{dy d^2 p_T}\,, && (4.2) \end{aligned}$$

respectively. Note that the blastwave does not incorporate fluctuations. This is one reason why we will not analyze the most central and peripheral centrality bins available which are known to exhibit large effects due to fluctuations. All expressions in the blastwave are taken at rapidity $y = 0$ and we have utilized matching data sets that have been taken around midrapidity.

We use data from the ALICE collaboration for Pb+Pb collisions at 2.76 TeV [53, 71, 65], in 10% centrality bins, and from the PHENIX collaboration for Au+Au collisions at 200 GeV [52, 72]. The PHENIX data is binned in 10 or 20% centrality bins for the spectra and 10% centrality bins for elliptic flow. For this analysis, if the PHENIX spectrum is only available in a coarser bin we combine a given 10% bin for elliptic flow together with the overlapping 20% bin for the spectrum. We find that centralities that share the coarser spectrum bins give results for temperature and specific shear viscosity that agree very well with each other within estimated uncertainties. E.g. from Fig. 4.8 (will present later) we can read off that the results for the 20-30% v_2 and 20-40% spectrum bins are consistent with the same quantities extracted from the 30-40% v_2 and 20-40% spectrum bins. The same is found for the bins spanning the 40-60% centrality spectra bin. We conclude that the increased uncertainty from the slight misalignment of bins is well covered by the other estimated uncertainties to be discussed below.

The selection of data points for the fit can introduce a bias that we try to quantify as an uncertainty. The following general principles were applied in the selection. We expect the blastwave parameterization to extract inaccurate parameters at too low momenta where resonance decays dominate the spectrum [73]. We also expect it to fail at too large momenta where gradient corrections become large, and hadrons from other production channels, like hard processes, start to dominate soft particles from the bulk of the fireball. The maximum momentum p_T described by the blastwave increases from peripheral to more central collisions, since particles are expected to be more thermalized when volumes and lifetimes are larger. In addition, flow pushes particles with the same velocity to higher momentum if their mass is larger. Thus fit ranges for heavier particles can extend farther.

Using these guiding principles, we choose a preferred fit range in transverse momentum for each centrality, collision energy and particle species. We call this selection the regular fit range (RFR). For example, the regular fit range for ALICE data in the 30-40% centrality bin uses data points for the spectra in the p_T-intervals 0.525-1.65 GeV/c, 0.225-2.25 GeV/c and 0.325-3.10 GeV/c for pions, kaons and protons, respectively. The RFR for all data sets used here is shown in Tab. 4.1. The v_2 data points included in this analysis are chosen to be consistent with the spectrum data points.

Centrality	proton (GeV/c)	kaon (GeV/c)	pion (GeV/c)	b (fm)	c_s^2	c_τ
ALICE 2.76 TeV						
10-20%	0.325-3.3	0.225-2.55	0.525-1.85	6.05	0.158	0.783
20-30%	0.325-3.1	0.225-2.35	0.525-1.75	7.81	0.162	0.755
30-40%	0.325-3.1	0.225-2.25	0.525-1.65	9.23	0.166	0.720
40-50%	0.325-2.95	0.225-2.15	0.525-1.45	10.47	0.170	0.679
50-60%	0.325-2.55	0.225-1.85	0.525-1.25	11.58	0.174	0.633
PHENIX 0.2 TeV						
10-20%	0.55-2.9	0.55-1.85	0.55-1.65	5.70	0.164	0.780
20-40%	0.55-2.7	0.55-1.75	0.55-1.55	8.10 (7.4, 8.7)	0.170	0.735
40-60%	0.55-2.5	0.55-1.65	0.55-1.45	10.5 (9.9, 11,0)	0.178	0.660

Table 4.1: Regular fit range (RFR) selected for each ALICE and PHENIX centrality bin for the spectra of all three particle species. The bins for elliptic flow data are chosen consistently. We also show the average impact parameter b from Glauber Monte Carlo calculations quoted by the experiments, and the speed of sound squared c_s^2 and the expansion parameter c_τ determined for each data set. For PHENIX data the average impact parameter for the two 10% bins included in a given 20% bin are quoted in parentheses.

We note that our fit ranges for ALICE data extend to higher momentum compared to the fit ranges previously used by the ALICE collaboration for their blastwave fits without viscous corrections [52]. In Ref. [52], the fit ranges for spectra are 0.5-1 GeV/c, 0.2-1.5 GeV/c, 0.3-3 GeV/c for pions, kaons and protons, respectively. For each data set we supplement the regular fit ranges with lower (LFR) and higher (HFR) fit ranges in an attempt to quantify uncertainties from fit range selection. This will be discussed in detail in the next section.

As discussed in chapter 2, not all parameters are good fit parameters and we are often interested in parameters that reflect the main features of the blastwave model; others are less interesting. We constrain R_x, R_y and T_{fo} by fitting the ratio R_y/R_x, the time τ_{fo} and by adding the simple geometric estimate (also mentioned in Eq. (2.62))

$$R_x \approx (R_0 - b/2) + \tau_{\text{fo}} c_\tau (\alpha_0 + \alpha_2)\,, \tag{4.3}$$

for the propagation of the fireball boundary in the x-direction. Here R_0 is the radius of the colliding nucleus and b is the impact parameter. The expansion parameter $c_\tau = \bar{\alpha}_0/\alpha_0$ relates the *time-averaged* surface velocity $\bar{\alpha}_0$ with its final value α_0 at freeze-out. The boundary velocity parameters α_0 and α_2 at freeze out are fitted to data. c_τ can be estimated to be between 0.6 and 0.8 going from the most peripheral bin to the most central bin in the analysis. This can be inferred from typical radial velocity-vs-time curves obtained in fluid dynamic simulations [74]. As this is a simple model we vary c_τ in the next section to explore the uncertainties from this choice of parameter reduction, see Tab. 4.9. The impact parameter b used for each centrality bin is taken from Glauber Monte Carlo simulations used by the corresponding experiment [53, 75].

The parameter λ is related to the scalar momentum dependence in δf. In principle, one could choose it as a fit parameter. We have run analysis with different values of λ which indicated that a value around $\lambda \sim 2$ is preferred. For example, for the 30-40% ALICE centrality we have varied λ in a step of 0.25 around 2. We find the best fits (largest likelihood) for $\lambda = 2$ ... 2.25 with significant drops of likelihood outside of this region. We conclude that $\lambda = 2$ is a good choice for this work. This is also an assumption widely used in literature [26, 14, 54]. Of course, it would be interesting to explore the effect more systematically in the future. Here we will set $\lambda = 2$.

The speed of sound squared c_s^2 for a hadronic matter is discussed e.g. in [76, 77]. We use [76] to adjust c_s^2 iteratively with the temperature found for each fitted centrality and collision system. The values we find are given in Tab. 4.1 for quick reference. Further below we will explore the dependence of the extracted shear viscosity and temperature on our choice of speed of sound by varying c_s^2. The relevant chemical potentials are not quite settled in the literature [78, 79, 80, 81, 76]. Typical values of μ_π= 60-80 MeV and μ_K= 100-130 MeV at kinetic freeze-out T_k= 110-120 MeV. We find good fits for chemical potentials for pions roughly consistent with [81, 76]. The values for (μ_π, μ_K, μ_p) for each data set are summarized in Tab. 4.2. Again we account for the uncertainties by varying the chosen values in the uncertainty analysis in the next section.

centrality	μ_π (MeV)	μ_K (MeV)	μ_p (MeV)	T (MeV)
ALICE 2.76 TeV				
10-20%	70	100	245	113
20-30%	64	85	220	118
30-40%	61	73	203	121
40-50%	58	63	190	126
50-60%	55	47	170	130
PHENIX 0.2 TeV				
10-20%	65	62	200	121
20-40%	61	51	188	124
40-60%	53	22	138	134

Table 4.2: Chemical potentials for pion, kaon and proton for each ALICE and PHENIX data set in its regular fit range, together with the extracted freeze-out temperatures.

Error bars for experimental data are crucial inputs for the statistical analysis. In the absence of further details about correlations between error bars we use the statistical and systematic errors quoted by experiments, summed in quadrature, for each momentum bin. This is the uncertainty input to the MADAI analysis. This procedure works well for ALICE data (here "works well" means we obtain reasonable results from MADAI analysis).

Total error	ALICE	PHENIX		
	30-40%	10-20%	20-40%	40-60%
spectra(%)	5.65	1.23	0.89	0.92
v_2(%)	3.24	6.71	3.13, 3.29	3.27, 3.80

Table 4.3: Typical error percentage, defined as the median for all bins in the RFR, for PHENIX data. The statistical error only is shown for the spectra. For comparison we also show one centrality bin of ALICE data. When two values for the error on v_2 are given they refer to the values in the smaller 10%-wide centrality bin covered.

Systematic errors for PHENIX identified hadron p_T-spectra are discussed in [52] but numbers are not included in the published data files. We thus start with the provided statistical errors and scale them up. Interestingly, we find that the statistical analysis also strongly suggests that statistical error bars alone for the PHENIX p_T-spectra are insufficient in the presence of much larger uncertainties for elliptic flow. This comes about because there is a competition between fits to p_T-spectra and v_2 regarding the best value of η/s. Momentum spectra prefer small viscous corrections, while v_2 data typically prefer large viscous corrections. The optimized η/s will be a balance between these constraints. If error bars are unbalanced between spectra and v_2, we see large likelihoods but nevertheless ill-fitting approximations for the quantity with larger error bars. We have to assume that the extraction of η/s is then biased in one direction. This suggests that if there is an imbalance, say the spectrum has much smaller relative error bars than elliptic flow, we *increase* the error bars on the quantity with tighter error constraints. This amounts to accepting an overall larger uncertainty for possibly less bias in the analysis. As a result of these considerations we multiply the statistical error given for PHENIX spectra by factors of 1.5, 3 and 4 for the 10-20%, 20-40% and 40-60% centrality bins, respectively. Table 4.3 shows the typical relative error in some data sets in the regular fit range (RFR), before adjustments are made. The typical value is defined as the median value within the RFR for all three hadron species.

4.2 Fit Results

With the preparations from the previous sections in place we go ahead and analyze the available data for each energy and centrality bin. We use the statistical analysis package MADAI to determine fit parameters, which we have introduced in chapter 3. The fit results are generally of good quality despite the relatively large RFR fit range. As an example, we discuss here the 30-40% centrality bin for ALICE data in detail. Fig. 4.1 shows the results for the fit parameter set $\mathcal{P}$ from the statistical analysis for fits in the RFR of this data set.

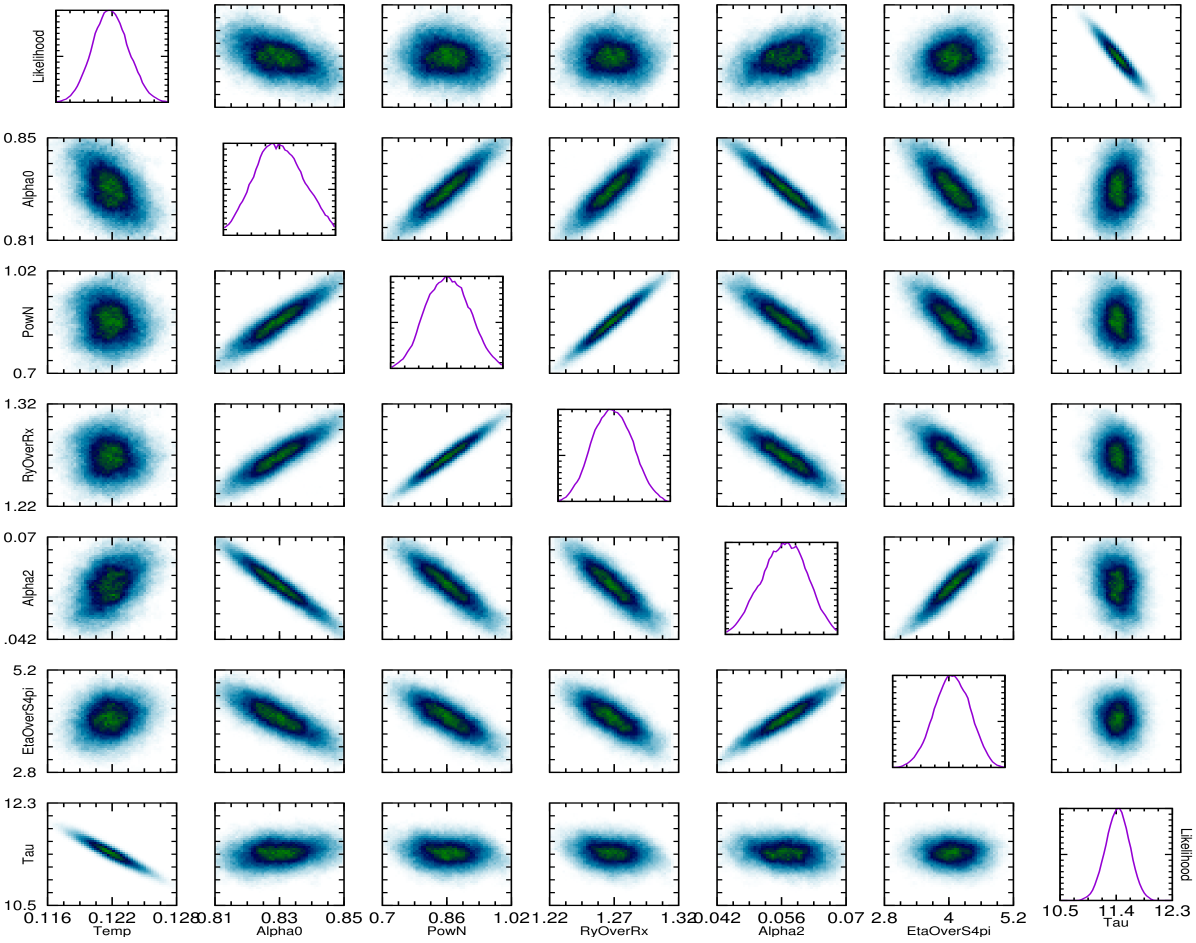

Figure 4.1: Likelihood analysis for ALICE data in the 30-40% centrality bin provided by the MADAI package. The diagonal show posterior likelihood distributions. The off-diagonal plots show correlations between parameters.

The horizontal and vertical axes show the chosen prior ranges for the parameters $\mathcal{P}$. From left to right (top to bottom): T (MeV), α_0, n, R_y/R_x, α_2, η/s, τ (fm/c). Plots on the diagonal show posterior likelihood distributions. The off-diagonal plots show correlations between parameters.

The likelihood plots on the diagonal of Fig. 4.1 show well defined peaks. Based on the output of the MADAI package, the preferred (average) values for this ALICE centrality bin are $\tau = 11.4$ fm/c, T=122 MeV, α_0=0.830c, n=0.87, R_y/R_x=1.27, α_2=0.056c, η/s=4.1/4π. The fit range and the values for the external parameters c_τ, c_s^2 and chemical potentials are given in Tab. 4.1 and Tab. 4.2, respectively.

Although we have already eliminated some parameters from the blastwave, there are still correlations between the remaining parameters in $\mathcal{P}$. Most prominently, there is an expected anti-correlation between freeze-out time and temperature which comes from the constraint on the overall number of particles. Surprisingly there is no pronounced anti-correlation between temperature and radial flow parameter α_0, which means that the choice of three different hadrons to fit, and the sizes of the fit ranges, are sufficient to cleanly separate thermal and collective motion. We note a correlation between the elliptic flow parameter α_2 and η/s. As expected, for larger values of p_T these two parameters move the elliptic flow in different directions, i.e. an increase in one of these parameters will necessitate an increase in the other one. The correlations seen in this centrality bin are found to be qualitatively true for the other energies and centrality bins as well.

Using the preferred parameters, we calculate the transverse momentum spectra and elliptic flow v_2 for the 30-40% ALICE centrality bin. We show these calculations together with the data in Fig. 4.2. The bottom of the figure shows the ratio of calculation over data. For the majority of p_T-bins the deviation is less than 5%, and it rarely exceeds 20%. If the experimental error bars are included, the ratio is consistent with one almost everywhere in the RFR.

We analyze other centrality bins of ALICE analogously. The results for all ALICE centrality bins are summarized in Tab. 4.4 and the fits with preferred parameter values are shown in Fig. 4.4 and Fig. 4.5. We note that the general trends of parameters as functions of centrality are consistent with expectations. The freeze-out temperature T_{fo} rises toward smaller systems. The boundary velocity α_0 reduces slightly at the same time. The spatially averaged radial velocity is given by

$$\langle v_T \rangle = \frac{\int \alpha_0 \rho^n d^2 r}{\int d^2 r} = \frac{2}{2+n}\,\alpha_0 \tag{4.4}$$

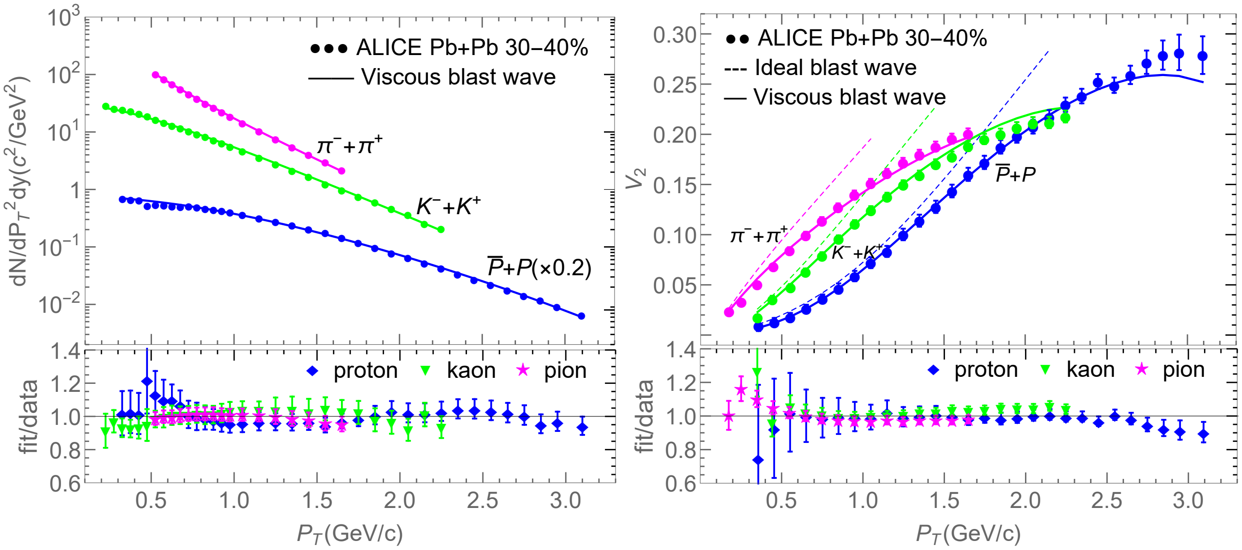

Figure 4.2: Left panel: Transverse momentum spectra for pions, kaons and protons (solid lines), respectively, using the extracted, preferred fit parameters for the ALICE 30-40% centrality bin. Right panel: Elliptic flow v_2 for the same parameters, together with ALICE data (circles). Ratios of calculations to data are shown below the panels.

which drops more significantly due to the concurrent change in the radial shape parameter n, as shown in Fig. 4.3. These systematic trends give an important qualitative check of the fit results. However, we will not be interested in further interpretation of fit parameters other than the temperature and specific shear viscosity. The ALICE data sets provide us with a range of temperatures from roughly 113 MeV to 130 MeV.

The sensitivity of the calculated elliptic flow on η/s at freeze-out is shown in Fig. 4.2. As expected, at large p_T the corrections from δf are largest; thus extracted values of η/s are very sensitive to v_2 at large p_T. As discussed earlier, δf cannot be too large and higher order corrections in shear stress would have to be taken into account if $\delta f \approx f$. We have chosen the RFR such that v_2 starts to deviate from the equilibrium behavior at large p_T, but we generally exclude points for which the slope of v_2 turns negative. In the RFR, we find that the viscous correction is largest for protons, topping out at 19% for the largest p_T-bin in the spectrum for the 40-50% centrality bin. For kaons and pions the largest corrections for the spectra are 11% and 4%, respectively. The typical size of viscous corrections is much smaller than the maximum numbers quoted here.

Centrality	τ (fm/c)	T (MeV)	α_0/c	n	R_y/R_x	α_2/c	$4\pi\eta/s$
ALICE 2.76 TeV							
10-20%	14.8	113	0.856	0.78	1.14	0.036	5.9
20-30%	13.1	118	0.839	0.80	1.20	0.052	5.5
30-40%	11.4	122	0.830	0.87	1.27	0.056	4.1
40-50%	10.0	126	0.835	1.07	1.36	0.047	2.5
50-60%	8.7	130	0.823	1.27	1.43	0.043	1.7
PHENIX 0.2 TeV							
10-20%	10.9	121	0.734	0.80	1.09	0.046	3.3
20-30%	9.3	124	0.742	0.94	1.17	0.053	2.0
30-40%	9.1	124	0.733	0.90	1.23	0.058	1.6
40-50%	7.2	132	0.704	1.03	1.31	0.063	1.1
50-60%	7.0	135	0.689	1.00	1.35	0.063	0.9

Table 4.4: Preferred values for the parameter set $\mathcal{P}$ obtained for different centrality bins for ALICE and PHENIX data in the regular fit range.

We repeat the analysis with data from PHENIX in 200 GeV Au+Au collisions. The preferred, average values are also summarized in Tab. 4.4. The fits with preferred parameter values are shown in Fig. 4.6 and Fig. 4.7 together with PHENIX data. The behavior of the parameters as a function of centrality is similar to the one discussed for the ALICE data sets. The extracted temperatures range, roughly 122 MeV to 136 MeV, overlaps with ALICE.

It is an important consistency check that the extracted values for η/s are consistent between ALICE data taken at $\sqrt{s_{NN}} = 2.76$ TeV and PHENIX data taken at $\sqrt{s_{NN}} = 0.2$ TeV, within uncertainties. We summarize the results for η/s vs temperature T from all data sets in Fig. 4.8. The main qualitative feature is a decrease in η/s with increasing temperature, as would be expected from general principles. However, values close to the lower bound for η/s are already reached at the upper end of the temperature range.

4.3 Uncertainty Analysis

Let us now turn to a discussion of the uncertainties in our analysis. We can group them into four categories, ranging from basic statistical errors to rather fundamental in nature: (I) Fundamental limitations in our freeze-out ansatz that are shared between blastwave and fluid dynamics, e.g.

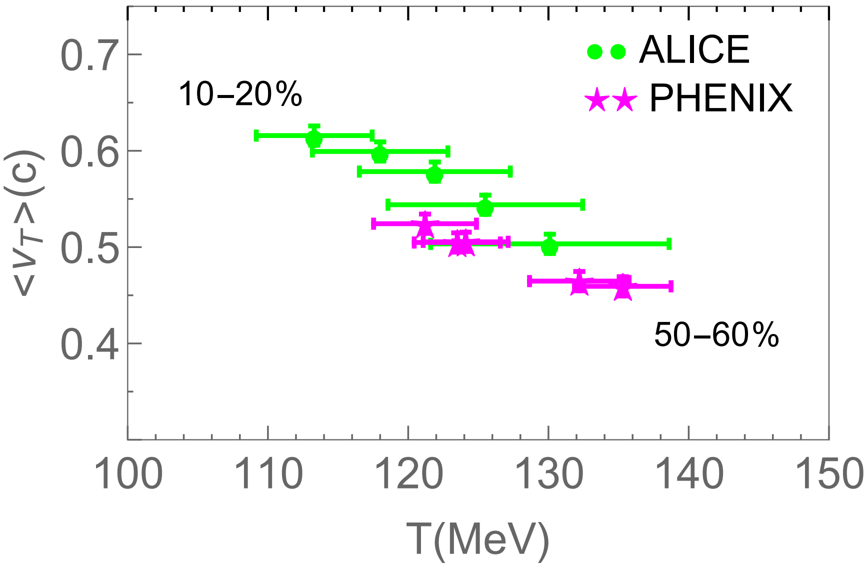

Figure 4.3: The spatially averaged radial velocity $\langle v_T \rangle$ from blastwave calculation using extracted parameters. Centrality increases from left to right.

from the validity of the Navier-Stokes approximation, and the assumption of a sharp freeze-out hypersurface. (II) Uncertainties and biases from assumptions made specifically in our blastwave model, e.g. the simple ansatz for the freeze-out hypersurface and the flow field, and the lack of resonance decays and bulk stress effects. (III) Uncertainties from our choice of external parameters and choice of fit ranges. (IV) Uncertainties from the errors in experimental data and the quality of the Gaussian emulator. A thorough analysis of item (I) is beyond the scope of this work and cannot be achieved within the blastwave model. However we will attempt to analyze the other three sources of uncertainty.

Uncertainties in extracted parameters from the error bars in our data sets and statistical analysis (type IV), are provided by the MADAI code. We quote the widths σ_T^{stat}, $\sigma_\eta^{\mathrm{stat}}$ of temperature and specific shear viscosity for each centrality bin and energy. We estimate uncertainties summarized under (III) by systematically varying the underlying assumptions. E.g., as discussed earlier we choose alternative fit ranges which are shifted to lower (LFR) or larger (HFR) p_T. Limitations apply as we do not want to push too far into regions where we expect our blastwave to fail, see the

Centrality	low fit range (GeV/c)			high fit range (GeV/c)		
	proton	kaon	pion	proton	kaon	pion
ALICE 2.76 TeV						
10-20%	0.325-2.05	0.225-1.45	0.19-0.975	1.25-3.3	0.775-2.65	0.875-2.05
20-30%	0.325-2.05	0.225-1.35	0.19-0.925	1.25-3.1	0.775-2.35	0.875-1.95
30-40%	0.325-2.05	0.225-1.25	0.19-0.825	1.25-3.1	0.725-2.25	0.825-1.85
40-50%	0.325-1.95	0.225-1.15	0.19-0.825	1.25-2.95	0.725-2.15	0.825-1.75
50-60%	0.325-1.95	0.225-1.15	0.19-0.725	1.05-2.75	0.725-2.05	0.825-1.55
PHENIX 0.2 TeV						
10-20%	0.65-2.5	0.55-1.55	0.55-1.35	0.65-2.9	0.55-1.85	0.65-1.85
20-40%	0.65-2.3	0.55-1.45	0.55-1.25	0.65-2.7	0.55-1.75	0.55-1.75
40-60%	0.65-2.1	0.55-1.35	0.55-1.15	0.65-2.5	0.55-1.65	0.55-1.65

Table 4.5: Definitions of lower fit range (LFR) and higher fit range (HFR) for ALICE and PHENIX spectrum data in different centrality bin. The ranges for v_2 data are chosen commensurately.

discussion of fit ranges in Sec. 4.1.

We discuss results once more for the 30-40% ALICE centrality bin as an example. For the uncertainty analysis we focus on the results for the extracted temperature and specific shear viscosity. Table 4.5 shows the three fit ranges, LFR, RFR, HFR for all three particle species for this data set. Both temperature and η/s show moderate dependencies on the fit range. This is expected for the temperature, where a change in p_T samples different admixtures of resonance decays in spectra with different slopes and thus apparent temperatures. We parameterize the deviations seen from the RFR values as Gaussian fluctuations with widths σ_k^{range} ($k = T, \eta$). We repeat this analysis for all other centralities and energies with qualitatively similar results.

As discussed earlier, we also study the effects of variations in the chemical potential, speed of sound squared, and the expansion parameter c_τ. Tab. 4.7 shows the values for T and η/s extracted for the 30-40% ALICE centrality bin for ± 15 MeV variations in the pion chemical potential. We find that the temperature is rather insensitive to variations of μ_π while η/s displays moderate sensitivity. We again assign Gaussian widths σ_k^μ ($k = T, \eta$) for the uncertainty from this source. We proceed similarly with variations in c_s^2 (Tab. 4.8) and c_τ (Tab. 4.9). In both cases we find again very little influence on the extracted temperature. Finally we combine the uncertainties of types

Centrality	low fit range		high fit range	
	T (MeV)	$4\pi\eta/s$	T (MeV)	$4\pi\eta/s$
ALICE 2.76 TeV				
10-20%	108.3	5.83	117.2	5.11
20-30%	110.8	5.40	121.4	4.94
30-40%	113.4	3.85	125.2	3.43
40-50%	115.5	2.42	131.3	2.10
50-60%	118.2	1.73	137.4	1.44
PHENIX 0.2 TeV				
10-20%	116.1	2.61	124.8	3.24
20-30%	121.7	2.77	128.2	2.38
30-40%	122.9	2.31	129.1	1.89
40-50%	128.6	1.10	135.9	1.21
50-60%	132.7	1.07	139.1	0.97

Table 4.6: Extracted temperature and specific shear viscosity for lower fit range (LFR) and higher fit range (HFR) for ALICE spectrum data in different centrality bin.

(III) and (IV) by adding the individual widths σ_T^i and σ_η^i in quadrature. Note that this assumption of Gaussian behavior here is simply an approximation. The error bars in T and η/s shown in Fig. 4.8 are the result of this analysis. Tab. 4.10 and Tab. 4.11 summarize the uncertainties. The left panel of Fig. 3.10 shows our best fit results for ALICE and PHENIX data with combined uncertainties of types (III) and (IV).

Finally we discuss the impact of uncertainties of type (II) on our result. Our blastwave is compared to viscous fluid dynamics in detail in chapter 3. We briefly summarize the results relevant for this chapter. In order to quantify what happens when complex final states are fitted by blastwaves, one can compare particle spectra and elliptic flow from output of the viscous fluid dynamic code MUSIC, and subsequently apply the same analysis that we have carried out for experimental data. The key is that in the case of MUSIC we know the precise temperature of freeze-out and the specific shear viscosity set in the code. Let us recall that the there are four main simplifications compared to fluid dynamics in our blastwave: (a) simplified hypersurface, (b) simplified flow field, (c) absence of resonance production and decay, and (d) absence of bulk stress corrections to particle distributions. While we focus on the compound effect here one could in principle study the

Centrality	small μ_{fo}			large μ_{fo}		
	μ_π (MeV)	T (MeV)	$4\pi\eta/s$	μ_π (MeV)	T (MeV)	$4\pi\eta/s$
ALICE 2.76 TeV						
10-20%	55	112.4	6.14	85	114.5	5.64
20-30%	49	117.0	5.91	79	119.1	5.46
30-40%	46	121.0	4.01	76	122.7	3.82
40-50%	43	124.5	2.59	73	126.6	2.37
50-60%	40	127.5	1.76	70	131.5	1.58
PHENIX 0.2 TeV						
10-20%	50	121.3	4.35	80	122.5	3.80
20-30%	46	125.0	1.90	76	126.3	1.79
30-40%	46	125.5	1.51	76	126.4	1.39
40-50%	38	133.5	1.29	68	134.4	1.10
50-60%	38	134.7	1.00	68	136.2	0.97

Table 4.7: The freeze-out temperature T and specific shear viscosity η/s extracted for different values of pion chemical potential μ_π. We vary the values of μ_π by adding or subtracting 15 MeV from the regular ones.

Centrality	small c_s^2			large c_s^2		
	$c_s^2(c^2)$	T (MeV)	$4\pi\eta/s$	$c_s^2(c^2)$	T (MeV)	$4\pi\eta/s$
ALICE 2.76 TeV						
10-20%	0.142	113.1	5.92	0.174	113.7	5.74
20-30%	0.146	117.3	5.42	0.178	118.2	5.61
30-40%	0.15	121.8	4.27	0.182	122.0	3.85
40-50%	0.154	125.4	2.54	0.186	125.4	2.38
50-60%	0.158	130.5	1.70	0.19	130.4	1.63
PHENIX 0.2 TeV						
10-20%	0.148	121.3	4.35	0.18	122.5	3.80
20-30%	0.154	125.7	2.19	0.186	125.8	1.76
30-40%	0.154	125.9	1.67	0.186	126.0	1.37
40-50%	0.162	132.0	1.07	0.194	132.6	0.99
50-60%	0.162	134.6	0.96	0.194	135.5	0.87

Table 4.8: The same as Tab. 4.7 for a variation of the speed of sound squared c_s^2. We vary the values of c_s^2 by adding or subtracting 0.016 from the regular ones.

Centrality	small c_τ			large c_τ		
	c_τ	T (MeV)	$4\pi\eta/s$	c_τ	T (MeV)	$4\pi\eta/s$
ALICE 2.76 TeV						
10-20%	0.737	113.8	5.91	0.832	113.3	6.04
20-30%	0.706	117.9	5.40	0.81	117.5	5.95
30-40%	0.666	121.6	3.82	0.781	121.2	4.12
40-50%	0.62	125.5	2.37	0.744	125.7	2.57
50-60%	0.568	130.3	1.59	0.706	129.3	1.72
PHENIX 0.2 TeV						
10-20%	0.722	121.9	4.31	0.846	121.6	2.96
20-30%	0.668	125.7	1.77	0.815	125.4	2.02
30-40%	0.665	125.9	1.33	0.812	125.9	1.64
40-50%	0.586	133.5	1.29	0.76	134.4	1.10
50-60%	0.583	135.3	0.86	0.757	135.4	0.98

Table 4.9: The same as Tab. 4.7 for a variation of time-averaged surface velocity parameter c_τ.

effect of each of these simplifications separately. In chapter 3, a map $(T,\eta/s)_{\text{hydro}} \to (T,\eta/s)_{\text{bw}}$ is created from an array of blastwave fits to fluid dynamic calculations on a grid of $(T,\eta/s)_{\text{hydro}}$ settings. We choose the T ranges and error bars for the analysis of MUSIC pseudo-data to be roughly consistent with the T ranges used in the actual data analyses. We also determine uncertainties analogous to the procedure used for fits to experimental data. We find that the extracted specific shear viscosities are mostly consistent with true values within uncertainties. However, the extracted temperature can be distorted and underestimates the true temperature significantly at high T. The map can be parameterized to very good approximation in the region of interest by a simple linear matrix M in $(T,\eta/s)$-space

$$\begin{pmatrix} T \\ \eta/s \end{pmatrix}_{\text{bw}} = \begin{pmatrix} 0.8365 & 3.90 \\ 0.0011 & 0.98 \end{pmatrix} \begin{pmatrix} T \\ \eta/s \end{pmatrix}_{\text{hydro}} \tag{4.5}$$

where temperatures are measured in MeV and η/s is in units of $1/4\pi$. By inverting M we can correct the results $(T,\eta/s)_{\text{extracted}}$ in this work and undo the bias introduced by the blastwave approximations: $(T,\eta/s)_{\text{extracted}} \to (T,\eta/s)_{\text{corrected}}$. $(T,\eta/s)_{\text{extracted}}$ are the results from our fits together

Centrality	uncertainties for $4\pi\eta/s$					
	Stat. analysis	fit range	μ_π	c_s^2	c_τ	total σ_η
ALICE 2.76 TeV						
10-20%	0.686	0.354	0.207	0.076	0.065	0.81
20-30%	1.005	0.228	0.214	0.083	0.247	1.08
30-40%	0.347	0.262	0.103	0.172	0.128	0.50
40-50%	0.169	0.161	0.09	0.066	0.081	0.27
50-60%	0.150	0.124	0.074	0.029	0.053	0.22
PHENIX 0.2 TeV						
10-20%	0.784	0.482	0.262	0.434	0.556	1.11
20-30%	0.431	0.360	0.050	0.180	0.102	0.60
30-40%	0.306	0.280	0.098	0.133	0.144	0.47
40-50%	0.193	0.060	0.097	0.038	0.074	0.24
50-60%	0.162	0.062	0.033	0.037	0.049	0.19

Table 4.10: A summary of uncertainties σ_η^i for specific shear viscosity. Here i refers to the different contributions discussed in the text.

with uncertainties of type (III) and (IV). As a result of removing the bias from the blastwave fit η/s drops more slowly with increasing temperature. We also propagate the error of our results through M^{-1} and add the uncertainty from the determination of M. This is the error shown in our final result discussed in the next section.

4.4 Discussion

We have introduced a blastwave model with viscous corrections due to shear stress in the Navier-Stokes approximation. The blastwave model can obtain excellent fits to hadron spectra and v_2 over a large range of p_T. The viscous correction term helps to describe the slow down of the growth of v_2 with p_T. This model provides a reliable instrument that can give useful snapshots of the dynamically evolving fireball.

To further demonstrate the usefulness we plot predictions for the spectra and v_2 for two more particles, the Λ baryon and the deuteron d, in a mid-central bin as examples. The results are shown in Fig. 4.9, Fig. 4.10 and Fig. 4.11 together with ALICE data [82, 83, 65]. Note that our calculation is a prediction in the sense that the Λ and deuteron data have not been used to fix the blastwave

Centrality	uncertainties for T (MeV)					
	Stat. analysis	fit range	μ_π	c_s^2	c_τ	total σ_T
ALICE 2.76 TeV						
10-20%	1.70	3.64	0.86	0.25	0.24	4.1
20-30%	1.70	4.42	0.86	0.39	0.22	4.8
30-40%	1.90	4.97	0.69	0.08	0.29	5.4
40-50%	2.20	6.53	0.86	0.05	0.09	6.9
50-60%	2.60	7.91	1.66	0.17	0.43	8.5
PHENIX 0.2 TeV						
10-20%	1.17	3.61	0.49	0.09	0.12	3.8
20-30%	1.62	2.67	0.53	0.08	0.12	3.2
30-40%	1.76	2.54	0.44	0.26	0.28	3.2
40-50%	2.13	3.03	0.42	0.62	0.33	3.8
50-60%	2.11	2.62	0.62	0.45	0.12	3.5

Table 4.11: A summary of uncertainties σ_T^i for temperature. Here i refers to the different contributions discussed in the text.

parameters. Chemical potentials for both species have been fixed, for example in 30-40% they are 344 and 314 MeV. We find overall good agreement for this centrality bin. This is interesting since there have been questions in both cases about the validity of a common freeze-out with stable hadrons. In particular, the deuteron is often thought to be emerging from coalescence processes after freeze-out [82, 84, 85]. We find that, whatever the detailed mechanism of deuteron creation, the spectra and elliptic flow are described reasonably well by the same temperature and flow field that also describes stable hadrons, at least in mid-central collisions.

Let us now turn to a discussion of the particular application of our blastwave we have focused on here. From two different collision systems, Pb+Pb at LHC energy and Au+Au at top RHIC energy we have extracted several η/s-vs-T points that are consistent with each other within estimated uncertainties. They give us a first (uncorrected) temperature dependence of η/s between roughly 110 MeV to 140 MeV, reaching the proposed lower bound at the latter temperature. We have carefully analyzed the uncertainties of type (II) that come specifically from the simplifying assumptions made in blastwave models. We find a systematic bias that underestimates the temperature T at larger temperatures. When we correct for this bias, we find the final result shown by the dots and stars in Fig. 4.12 with the compound uncertainties shown as ellipses.

We also show results for η/s for the hadronic phase from hadronic cascades UrQMD [35], B3D [86] and SMASH [37]. They generally show larger values of η/s above $T \sim 100$ MeV. One could speculate that below $T \sim 100$ MeV the results might converge within uncertainties, as the UrQMD and SMASH results switch their behavior to a temperature slope similar to our results. Unfortunately we do not have the data points to confirm this. After the work for this thesis was completed, a new result by Dash et al. using hadronic transport was published [87]. They obtain rather small values of η/s and are roughly consistent with our results. We also show several calculations of the specific shear viscosity in the QGP phase, from lattice QCD [41, 42, 44] and using next-to-leading perturbative QCD [47]. After correcting the bias, our extracted η/s reaches the proposed lower bound around the pseudocritical temperature T_c. Overall these results together are consistent with the idea of a minimum of the specific shear viscosity around T_c. Our result specifically would indicate that interactions in the hadronic phase continue to be strong just below T_c while hadronic transport suggests a more abrupt change below T_c. The gray band in Fig. 4.12 represents a simple parameterization of our result. The center line is $\eta/s = 1.6 \times 10^2 \times (0.160 - T)^2 + 0.08$ where T is measured in GeV. This is the preferred value of η/s as a function of T between 100 and 150 MeV temperature.

We need to keep in mind that relatively large chemical potentials for stable hadrons build up in the collision systems that we have analyzed here. E.g. the chemical potential for pions is as large as 70 MeV at the lowest temperature points we have extracted. Thus Fig. 4.12 is a projection of a more complicated plot with additional chemical potential axes. Studies with hadronic transport have indicated that finite chemical potentials can indeed lead to smaller values of η/s [35] in this picture.

The fate of η/s in the hadronic phase continues to be intriguing. We have added a scenario, based on extraction from data, that predicts a gradual rise of η/s while the temperature drops from 150 to 110 MeV and chemical potentials increase. Our approach is based on data taken in heavy ion collisions but has built in uncertainties. We have quantified the more accessible uncertainties (IV) and (III) related to the analysis itself and to systemic uncertainties from choices made during the analysis. We have also made a first attempt to estimate the weaknesses of the blastwave compared to a full fluid dynamic simulation, i.e. uncertainties of type (II). More fundamental uncertainties remain which may be quantified elsewhere.

Certain aspects of the current analysis will be improved in the near term future. For example, the detailed energy dependence of the shear stress term, parameterized by λ, and the effects of bulk stress could be included, albeit at the expense of adding two parameters to the analysis. One could also include an analysis of the asymmetry coefficient v_4, which requires a generalization of both hypersurface and flow field of the blastwave. Lastly, resonances and their decays could in principle be included in the calculation.

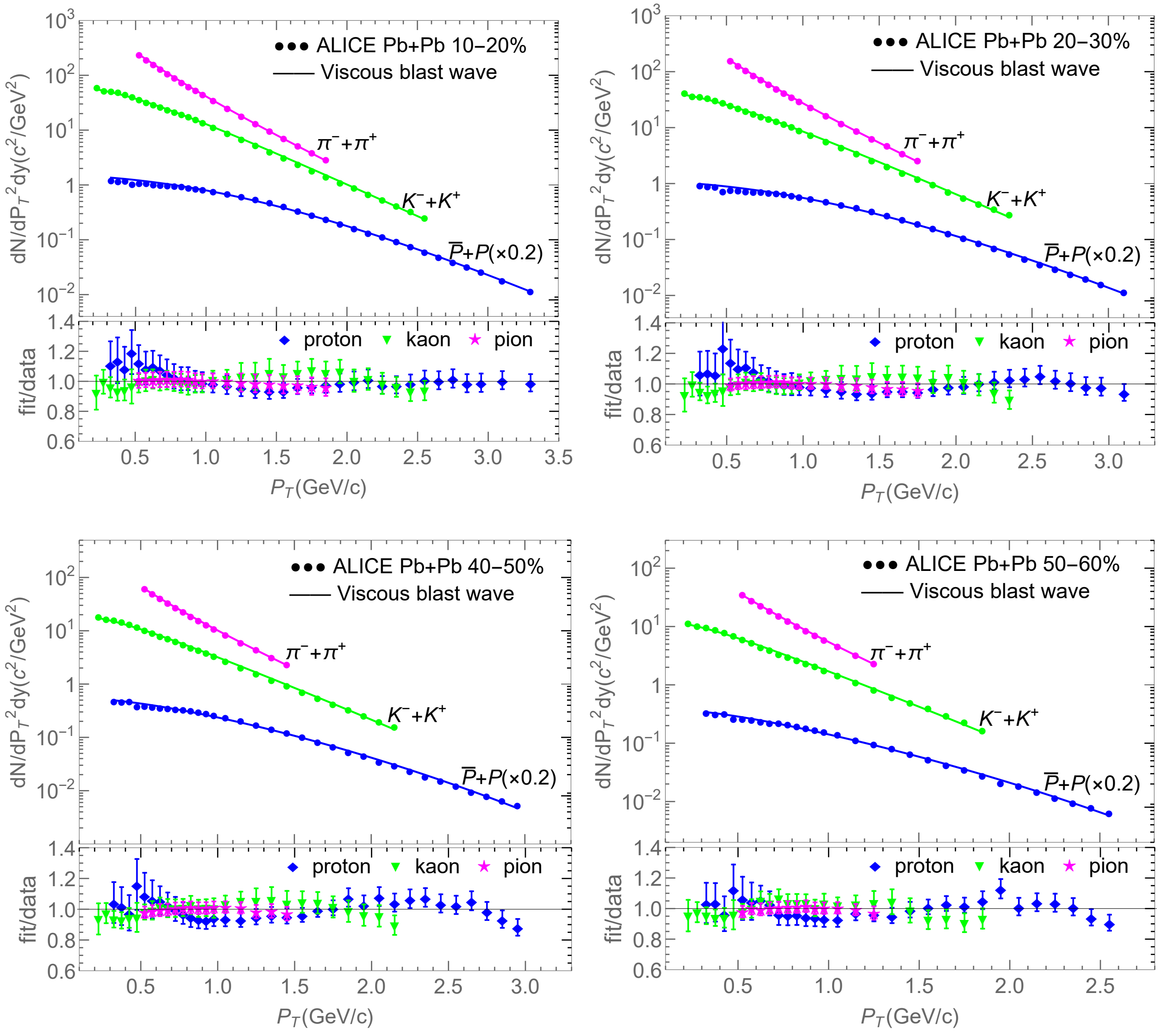

Figure 4.4: Transverse momentum spectra for pions, kaons and protons (solid lines), respectively, together with ALICE data (circles) in different centrality bins. Solid lines are blastwave calculation using extracted paramteres. Ratios of calculations to data are shown below the panels.

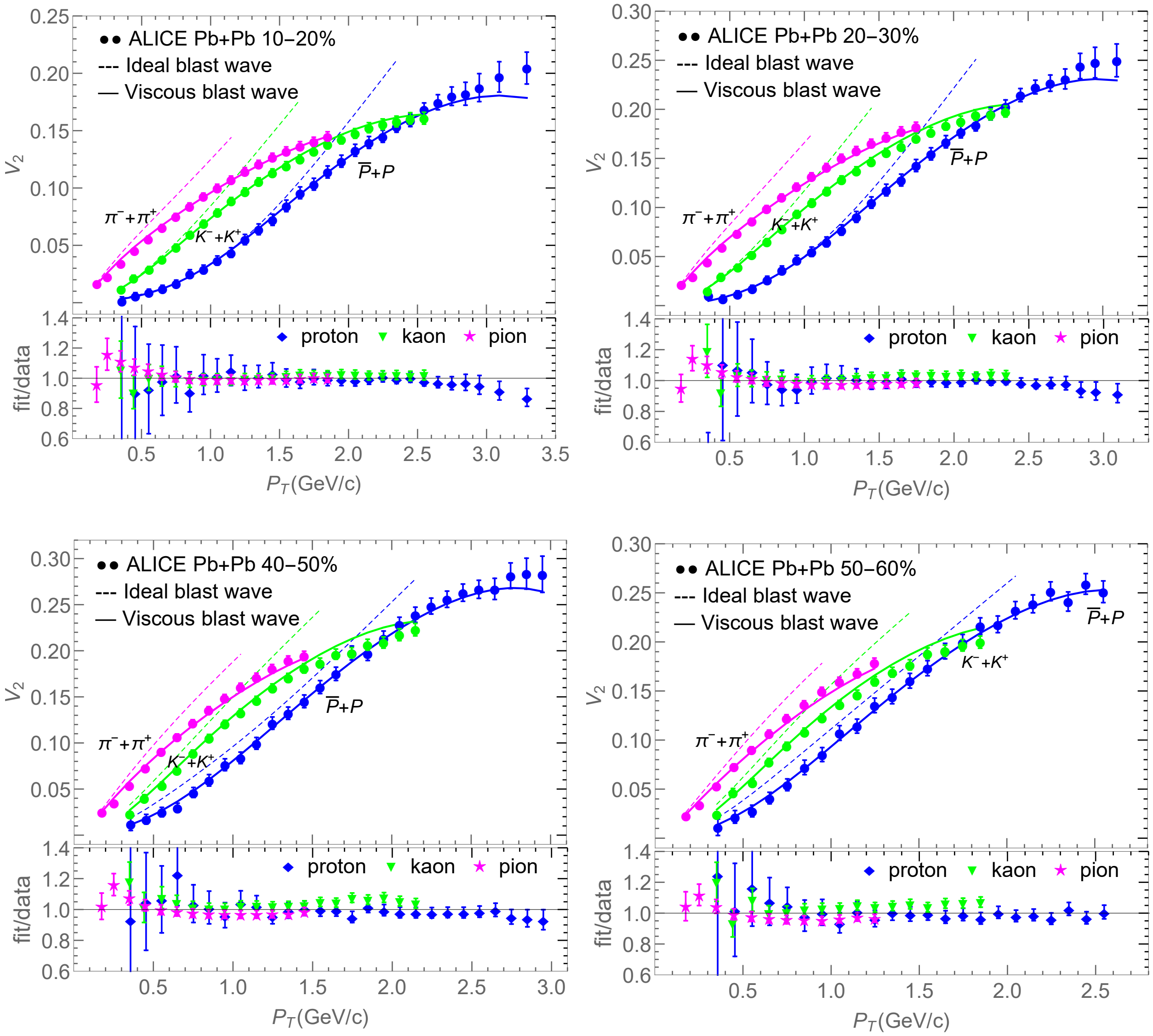

Figure 4.5: Elliptic flow v_2 for pions, kaons and protons (solid lines), respectively, together with ALICE data (circles) in different centrality bins. Solid lines are blastwave calculation using extracted parameters. Ratios of calculations to data are shown below the panels.

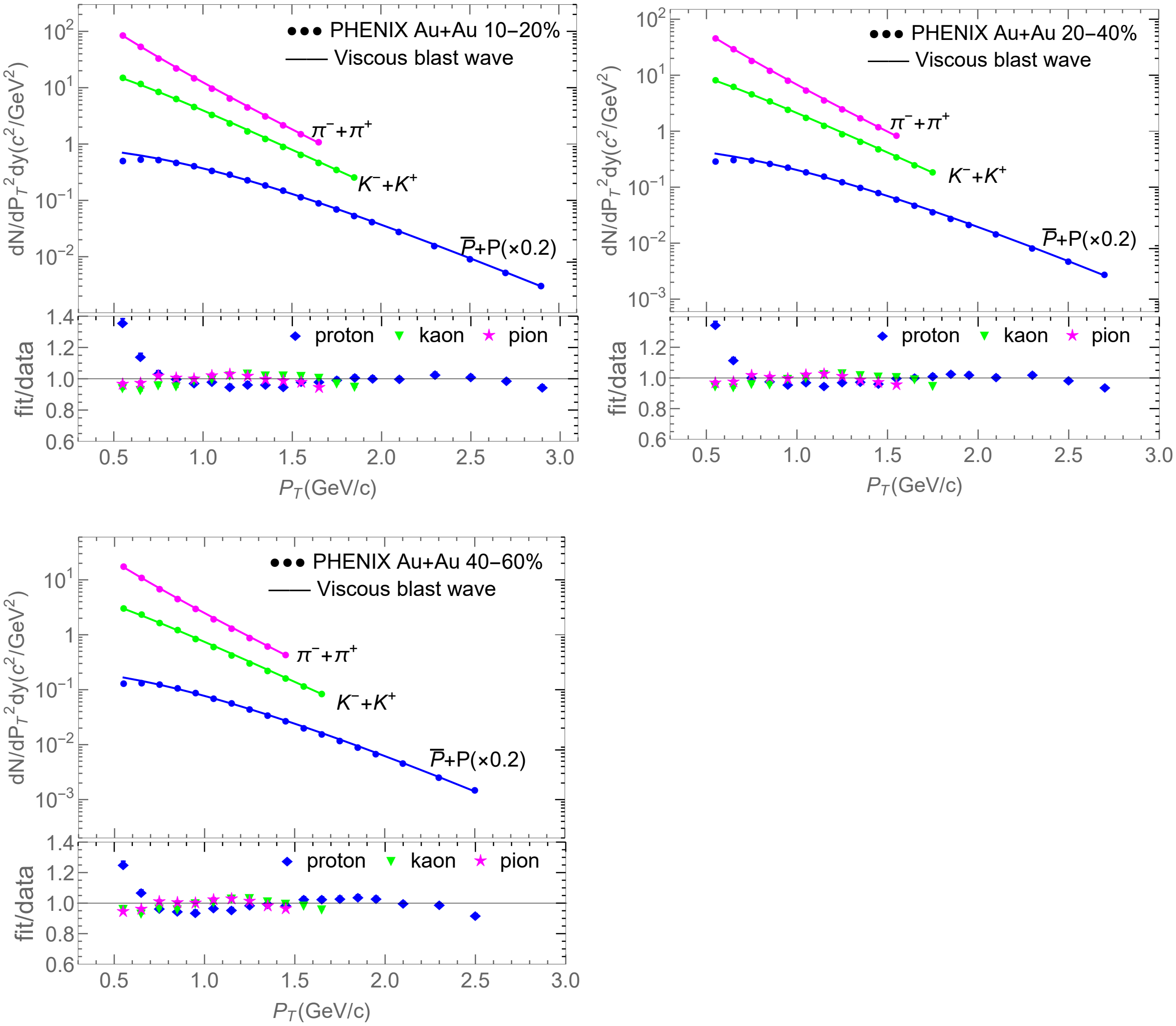

Figure 4.6: Transverse momentum spectra for pions, kaons and protons (solid lines), respectively, together with PHENIX data (circles) in different centrality bins.

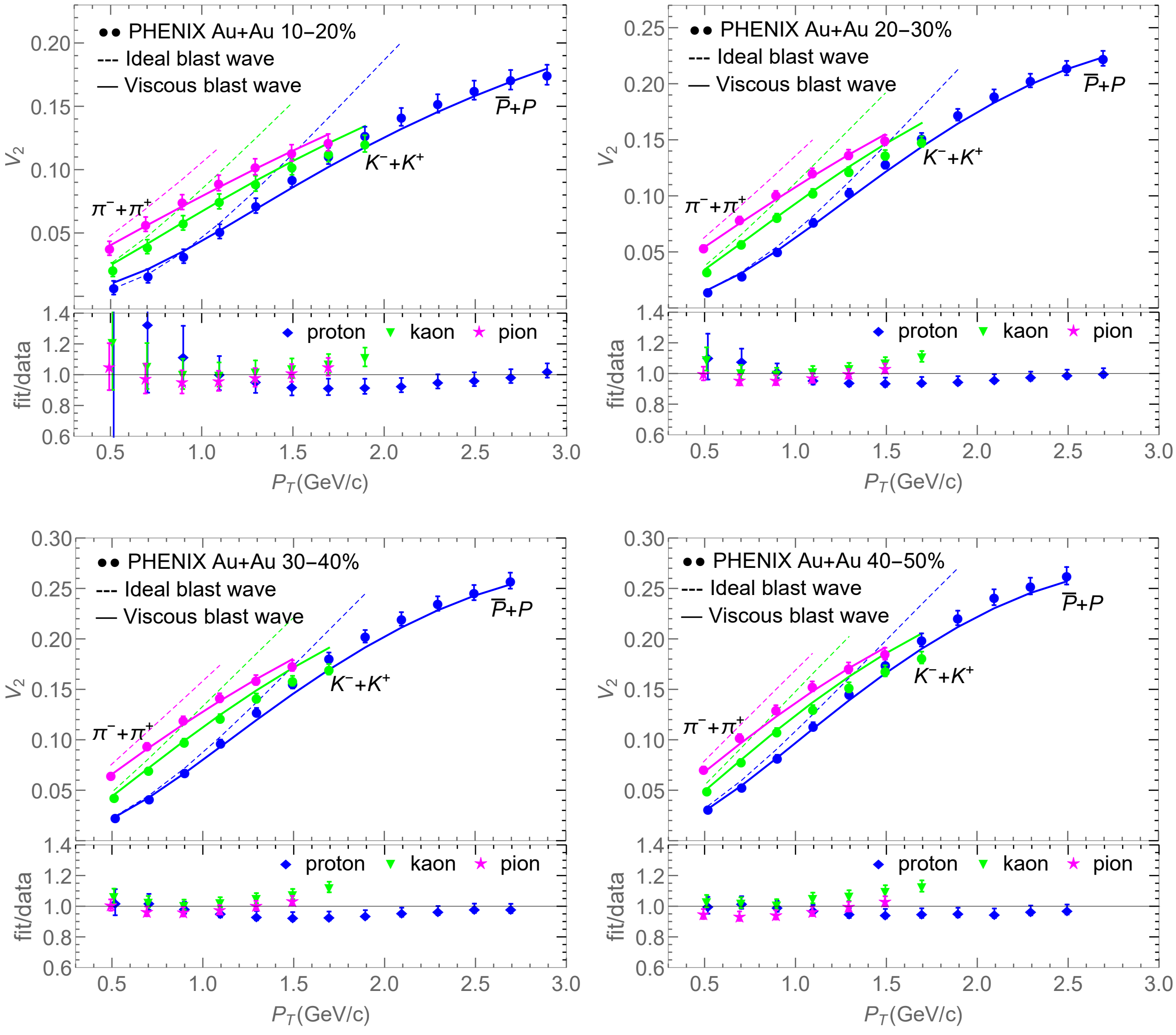

Figure 4.7: Elliptic flow v_2 for pions, kaons and protons (solid lines), respectively, together with PHENIX data (circles) in different centrality bins.

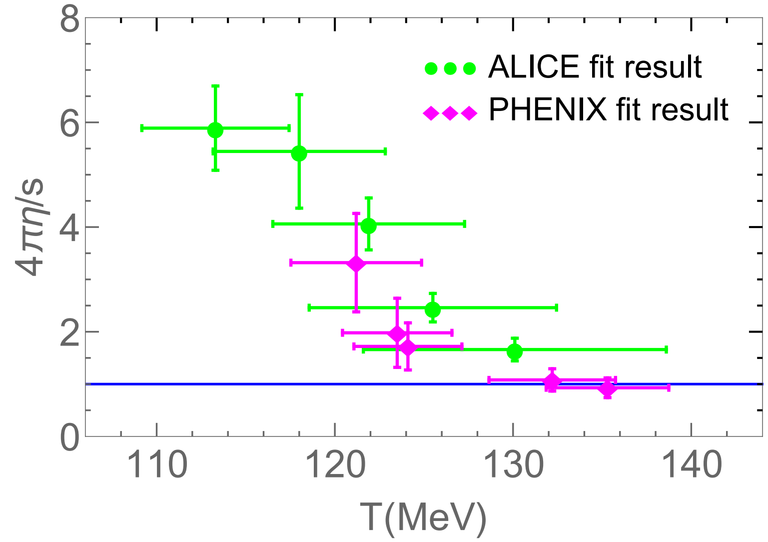

Figure 4.8: Specific shear viscosity η/s at corresponding kinetic freeze-out temperature T extracted from the available ALICE and PHENIX centrality bins before removing blastwave bias. Uncertainties shown are combined uncertainties of type (III) and (IV) explained in the text. Note that the values of the chemical potentials for stable hadrons are non-zero for all of these points.

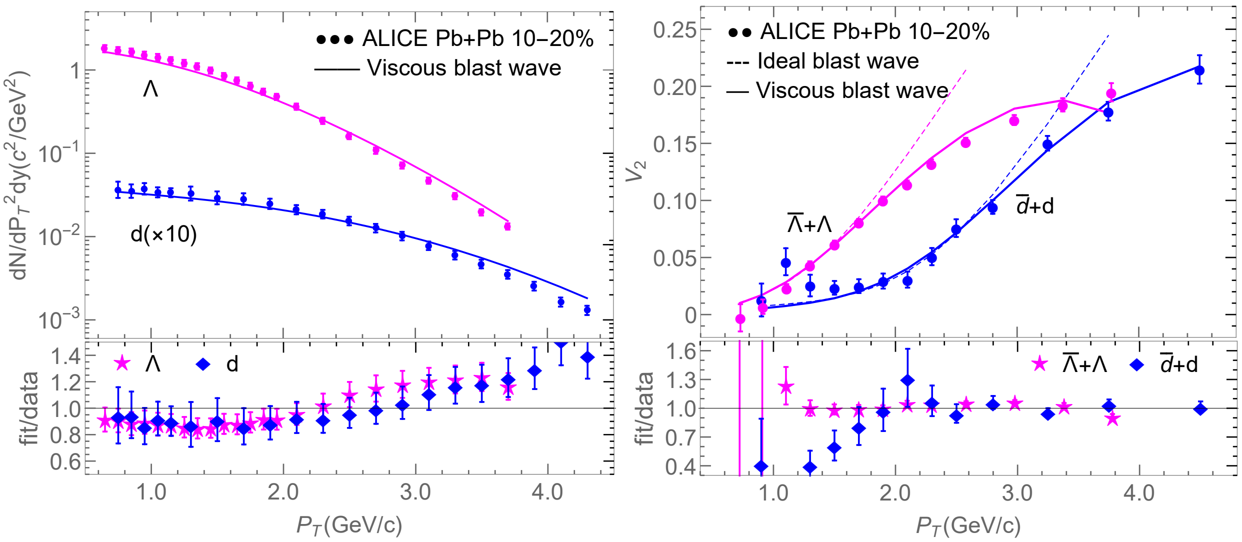

Figure 4.9: Left panel: Transverse momentum spectra for Λs and deuterons (solid lines), respectively, calculated for the 10-20% centrality bin in Pb+Pb collisions together with ALICE data (symbols). Right panel: Elliptic flow v_2 for $\Lambda + \bar{\Lambda}$ and $d + \bar{d}$ (solid lines) in the 10-20% centrality bin together with ALICE data (circles). We again show the elliptic flow calculated in the ideal case as well. In both cases the preferred parameters for the 10-20% centrality bin extracted for stable charged hadrons have been used.

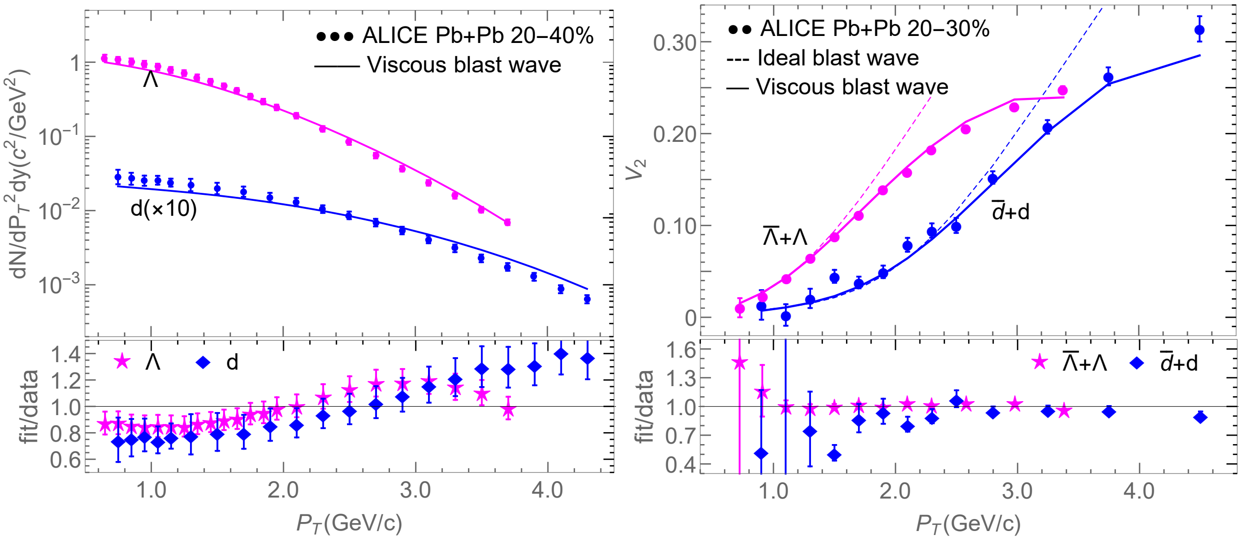

Figure 4.10: Same as 4.9 for the 20-40% centrality bin (20-30% for elliptic flow).

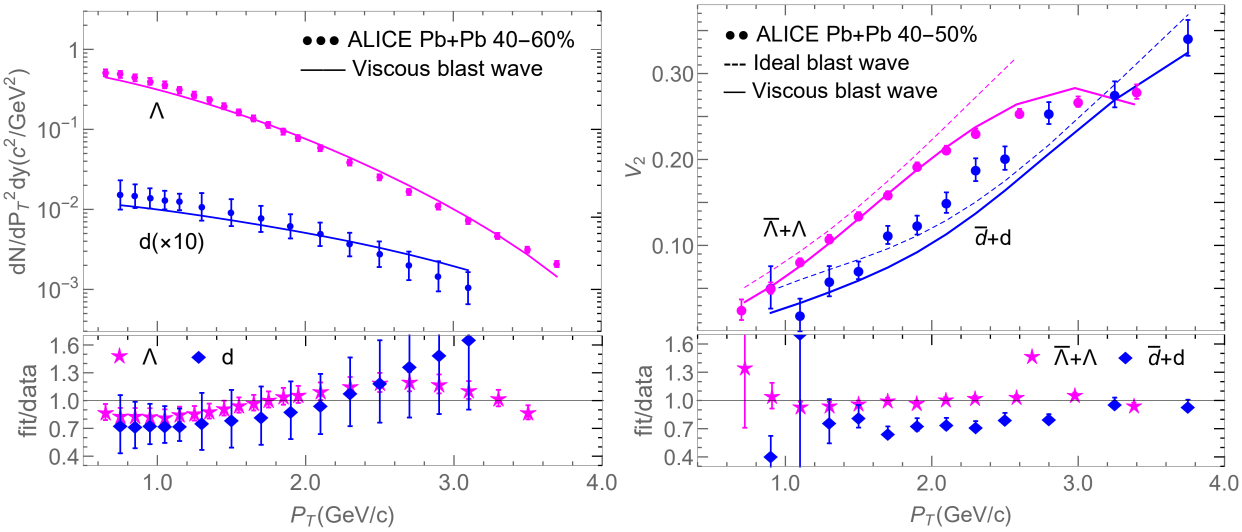

Figure 4.11: Same as 4.9 for the 40-60% centrality bin (40-50% for elliptic flow).

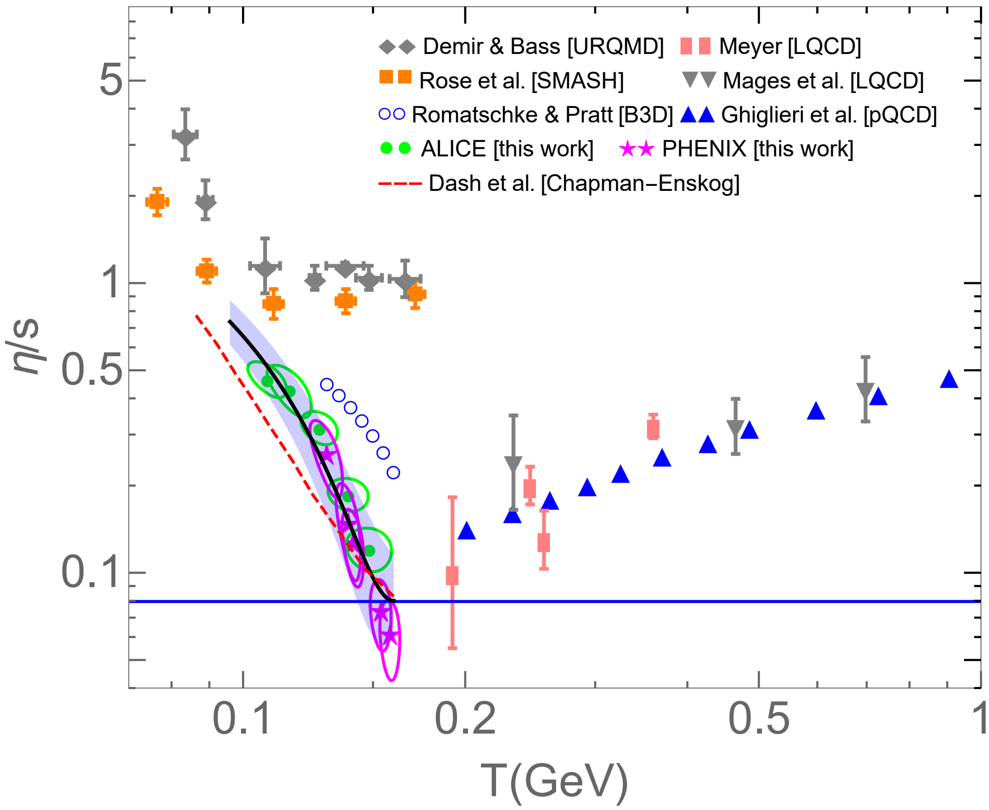

Figure 4.12: The main results of this chapter compared to various calculations of the specific shear viscosity η/s as a function of temperature. A line and uncertainty band have been drawn through our points to guide the eye. Details in the text.

5. QUARK RECOMBINATION

In this chapter, we will generalize the calculations in Refs. [58, 59, 60] and use our improved blastwave as an input for quark recombination. In that case, the blastwave parameterizes the behavior of quarks at the critical temperature T_c. Note this is different from chapter 4, in which the blastwave was applied to hadrons at T_{kin}. With a viscous blastwave, we expect to provide a more realistic quark space-momentum distribution compared to [60]. In particular we use the viscous corrections in the blastwave to account for deviations from ideal elliptic flow, i.e. the plateau in $v_2(p_T)$ at intermediate transverse momenta using a systematic and physical approach.

We use the viscous blastwave model to fit spectra and elliptic flow v_2 of identified hadrons at intermediate transverse momentum, 2 GeV/c $< p_T <$ 6 GeV/c. Note that this momentum range is above the one discussed in chapter 4. For each hadron species considered there is no overlap between the RFR and the intermediate momentum range here (except some minimal overlap in central collisions). The big picture is that at low p_T hadrons are created at T_c, possibly through recombination, but continue to interact and form a cooling and expanding hadronic matter close to kinetic equilibrium. On the other hand, hadrons in the intermediate p_T range might form through quark recombination and experience little rescattering so that the information from their properties around $T = T_c$ are encoded in their observed spectra and elliptic flow. Also, keep in mind that while we carried out precision fits in chapter 4, the current chapter is rather an exploratory study to demonstrate the viability of quark recombination with modern data sets that have become available after Ref. [60] was published.

We check the constituent quark number scaling (QNS) law by fitting v_2 of different hadrons at a variety of collision energies and impact parameters. For RHIC, we fit v_2 of $\pi^{\pm}$, $\mathrm{K}^{\pm}$, p+$\overline{\mathrm{p}}$ and ϕ, and also calculate results for Λ, Ξ^- and Ω^-. For LHC, we fit v_2 of $\pi^{\pm}$, $\mathrm{K}^{\pm}$, p+$\overline{\mathrm{p}}$, ϕ, Λ+$\overline{\Lambda}$, Ξ^-+$\overline{\Xi}^+$ and Ω^-+$\overline{\Omega}^+$. The overall description is rather good.

We also apply our blastwave as an input to the resonance recombination model (RRM) and calculate the elliptic flow of ϕ meson with the same blastwave parameters fitted before. Interestingly, we find rather compatible results with the instantaneous recombination model.

This chapter is organized as follows: in section 5.1 we summarize the formalism for instantaneous recombination model. In section 5.2 we discuss parameters and data selection. In section 5.3 we present the fits results with data. In section 5.4 we introduce the resonance recombination model.

5.1 Quark Recombination Formalism

In this section, we summarize the formalism for instantaneous quark recombination. For details, we recommend the reader to check Ref. [60]. We start from the number of mesons

$$N_M = C_M \int \frac{d^3p}{(2\pi)^3} \left\langle M;\mathbf{P}\right| \hat{\rho} \left|M;\mathbf{P}\right\rangle \tag{5.1}$$

here $\hat{\rho}$ is the density matrix quarks and $|M;\mathbf{P}\rangle$ is a meson state with momentum $\mathbf{P}$ and C_M is the degeneracy factor of mesons. We insert full sets of space coordinates

$$N_M = \int \frac{d^3p}{(2\pi)^3} d^3\hat{r}_1 d^3\hat{r}'_1 d^3\hat{r}_2 d^3\hat{r}'_2 \left\langle M;\mathbf{P}\right| \hat{r}_1,\hat{r}_2\rangle \langle \hat{r}_1,\hat{r}_2 \mid \hat{\rho} \mid \hat{r}'_1,\hat{r}'_2\rangle \langle \hat{r}'_1,\hat{r}'_2|M;\mathbf{P}\rangle. \tag{5.2}$$

and change the coordinates to $\mathbf{r}_{1,2} = (\hat{\mathbf{r}}_{1,2} + \hat{\mathbf{r}}'_{1,2})/2$ and $\mathbf{r}'_{1,2} = \hat{\mathbf{r}}_{1,2} - \hat{\mathbf{r}}'_{1,2}$. We write the 2-parton Wigner function $W_{ab}(\mathbf{r}_1,\mathbf{r}_2;\mathbf{p}_1,\mathbf{p}_2)$ as

$$\left\langle \mathbf{r}_1 - \frac{\mathbf{r}'_1}{2}, \mathbf{r}_2 - \frac{\mathbf{r}'_2}{2} \middle| \hat{\rho} \middle| \mathbf{r}_1 + \frac{\mathbf{r}'_1}{2}, \mathbf{r}_2 + \frac{\mathbf{r}'_2}{2} \right\rangle = \int \frac{d^3p_1}{(2\pi)^3}\frac{d^3p_2}{(2\pi)^3} e^{-i\mathbf{p}_1\cdot\mathbf{r}'_1} e^{-i\mathbf{p}_2\cdot\mathbf{r}'_2} W_{ab}(\mathbf{r}_1,\mathbf{r}_2;\mathbf{p}_1,\mathbf{p}_2) \tag{5.3}$$

and write the meson wave function φ_M as

$$\left\langle \mathbf{r}_1 + \frac{\mathbf{r}'_1}{2}, \mathbf{r}_2 + \frac{\mathbf{r}'_2}{2} \middle| \pi;\mathbf{P} \right\rangle = e^{-i\mathbf{P}\cdot(\mathbf{R}+\mathbf{R}'/2)}\, \varphi_M\!\left(\mathbf{r} - \frac{\mathbf{r}'}{2}\right) \tag{5.4}$$

We then change variables again to

$$\mathbf{R}^{(\prime)} = (\mathbf{r}_1^{(\prime)} + \mathbf{r}_2^{(\prime)})/2, \qquad \mathbf{r}^{(\prime)} = \mathbf{r}_1^{(\prime)} - \mathbf{r}_2^{(\prime)} \tag{5.5}$$

$$\mathbf{P} = \mathbf{p_1} + \mathbf{p_2}, \qquad \mathbf{q} = (\mathbf{p_1} - \mathbf{p_2})/\mathbf{2} \tag{5.6}$$

We define Φ_M as

$$\Phi_M(\mathbf{r}, \mathbf{q}) = \int d^3r' e^{-i\mathbf{q}\cdot\mathbf{r}'} \varphi_M\left(\mathbf{r} + \frac{\mathbf{r}'}{2}\right) \varphi_M^*\left(\mathbf{r} - \frac{\mathbf{r}'}{2}\right) \tag{5.7}$$

and integrate over $\mathbf{R}'$, then obtain

$$\frac{dN_M}{d^3P} = \int \frac{d^3\mathbf{q}\,\mathbf{d^3R}}{(2\pi)^3} \mathit{\Phi}_M(\mathbf{R}, \mathbf{q}) \mathbf{W_{q\bar{q}}}(\mathbf{p}, \mathbf{q}; \mathbf{R}) \tag{5.8}$$

With light cone coordinates and integrating over d^3r, the spectra of mesons are finally expressed as

$$E\frac{dN_M}{d^3P} = C_M \int_\Sigma \frac{p^\mu \cdot d\sigma_\mu}{(2\pi)^3} \int_0^1 dx_1 dx_2 \Phi_M(x_1, x_2) W_{q\bar{q}}(x_1\mathbf{P}, x_2\mathbf{P}; \mathbf{R}) \tag{5.9}$$

where C_M is the spin degeneracy factor of mesons, $d\sigma$ is the hypersurface of hadronization, $\mathit{\Phi}_M = \varphi_M^* \varphi_M$ is the meson wave function squared, $W_{q\bar{q}}$ is the two-parton Wigner function, and x_1, x_2 are light cone coordinates (defined as $\mathbf{p}_{1,2} = x_{1,2}\mathbf{P}$, the fraction of parton momentum). Note that two simplifications had been applied in Ref. [60]. First, the integral d^3r can be taken assuming that the average fireball is weakly varying within the size of a hadron. Second, since only momentum above $2..3$ GeV/c are used it is assumed that the hadrons and quarks are essentially ultra-relativistic and traveling along the light cone.

A similar expression can be derived for baryons

$$E\frac{dN_B}{d^3P} = C_B \int_\Sigma \frac{p^\mu \cdot d\sigma_\mu}{(2\pi)^3} \int_0^1 dx_1 dx_2 dx_3 \Phi_M(x_1, x_2, x_3) W_{q_1 q_2 q_3}(x_1\mathbf{P}, x_2\mathbf{P}, x_3\mathbf{P}; \mathbf{R}) \tag{5.10}$$

where C_B is the spin degeneracy factor, $\mathit{\Phi}_B$ is the baryon wave function squared and x_1, x_2, x_3 are light cone coordinates. Later we will use $C_M = 2$ for $\pi^\pm$ and $\mathrm{K}^\pm$, $C_M = 3$ for ϕ, $C_B = 4$ for p+$\overline{\mathrm{p}}$,

$C_B = 2$ for Λ^0 and Ξ^-, and $C_B = 4$ for Ω^-.

The wave functions of hadrons in this situation are only poorly known. In the extreme light cone limit is it possible to parameterize the wave function as polynomial [59, 60, 88]. An alternative option is to use a Gaussian ansatz

$$\Phi_M(x_1, x_2) = Ae^{\frac{(x_1-x_a)^2+(x_2-x_b)^2}{\sigma_M^2}}\delta(x_1 + x_2 - 1) \tag{5.11}$$

$$\Phi_B(x_1, x_2, x_3) = Be^{\frac{(x_1-x_a)^2+(x_2-x_b)^2+(x_3-x_c)^2}{\sigma_B^2}}\delta(x_1 + x_2 + x_3 - 1) \tag{5.12}$$

here $A(B)$ is a fixed constant so the integral over Φ_M (Φ_B) is normalized to unity and x_a, x_b (x_c) are the peak values. Φ_M should reach its maximum when the average velocity of the quarks is the same, so x_a, x_b are proportional to the corresponding quark masses

$$x_a = \frac{m_1}{m_1 + m_2}, \quad x_b = \frac{m_2}{m_1 + m_2} \tag{5.13}$$

Similar expressions can be used for baryons

$$x_a = \frac{m_1}{m_1 + m_2 + m_3}, \qquad x_b = \frac{m_2}{m_1 + m_2 + m_3}, \qquad x_c = \frac{m_3}{m_1 + m_2 + m_3} \tag{5.14}$$

We have carried out calculations for both light cone (polynomial) and Gaussian wave functions. We have used Gaussian wave functions in the final analysis in this chapter. It turns out the shape of hadron wave function does influence observables. We find a narrower wave function increases the hadron yield and elliptic flow. The transverse momentum spectra may increase by 50% and elliptic flow may increase by 10% compared to a much wider wave function. we also notice that polynomial and Gaussian wave functions give similar results if parameters are adjusted. Indeed if we give a very large power to polynomial wave functions, or give a very small width $\sigma_{M,B}$ to Gaussian wave functions, both will reach the limiting case of a δ-shaped wave function

$$\Phi_M(x_1, x_2) \sim \delta(x_1 - x_a) \tag{5.15}$$

$$\Phi_B(x_1, x_2, x_3) \sim \delta(x_1 - x_a)\delta(x_2 - x_b)\,. \tag{5.16}$$

For the Wigner function of quarks, we assume quarks are quasi-free and neglect interactions between them. We then factorize $W_{q\bar{q}}$ into classical single-particle phase space distributions

$$W_{q\bar{q}}(r_a, p_a; r_b, p_b) = f_q(r_a, p_a) f_{\bar{q}}(r_b, p_b)\,. \tag{5.17}$$

In the previous work [58, 59, 60], quark distributions were first assumed to be in thermal equilibrium. However, if one uses thermal equilibrium distributions, one cannot describe the saturation of elliptic flow growth with p_T. In order to break prefect thermal equilibrium, the natural way is to add viscous corrections. Indeed this was one of our motivations to develop a viscous blastwave. As in chapter 2, with viscous corrections the distribution function becomes

$$f_a(r,p) = f_0(r,p) + \delta f(r,p), \qquad f_0(r,p) = \frac{1}{e^{p^\mu \cdot u_\mu / T} \mp 1}\,. \tag{5.18}$$

where f_0 is the equilibrium Bose/Fermi-distribution with "-" for Bosons and "+" for Fermions and δf is a gradient correction of Navier-Stokes type. For the δf term, we use

$$\delta f(r,p) = \frac{\eta}{s} \frac{\Gamma(6)}{\Gamma(4+\lambda)} \left(\frac{E}{T}\right)^{\lambda-2} \frac{p_\mu p_\nu}{T^3} \sigma^{\mu\nu} f_0(r,p) \tag{5.19}$$

which follows from a generalized Grad ansatz [67]. The details for the viscous corrections have already been presented in chapter 2 and will not be repeated here. We utilize our blastwave to provide quark distributions at the critical temperature T_c. Fig. 5.1 shows the spectrum and elliptic flow of up/down and strange quarks. One can find the dependence of spectra and elliptic flow on the viscous corrections.

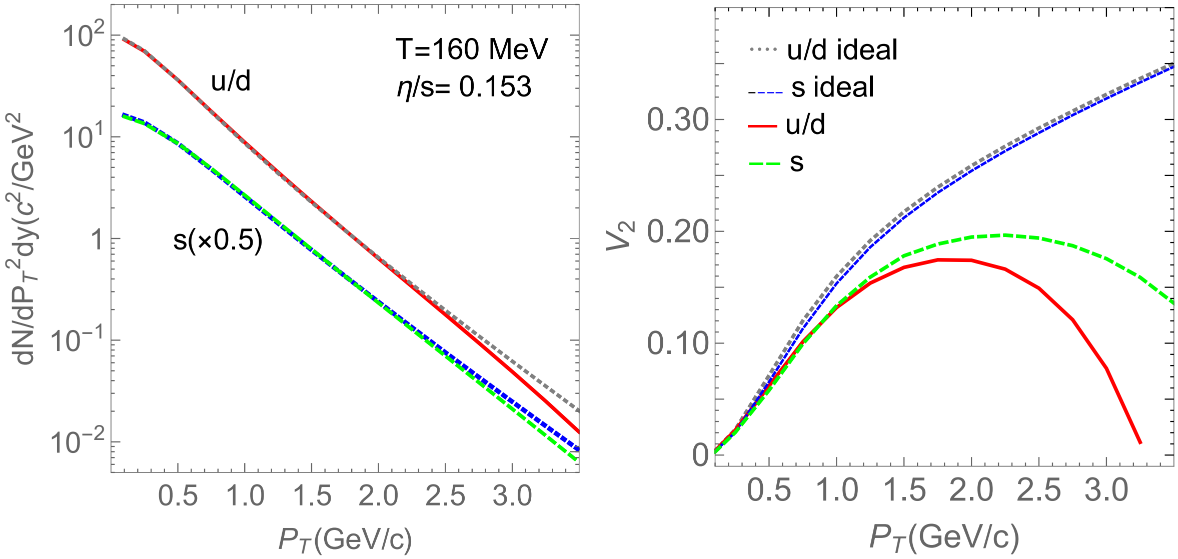

Figure 5.1: Transverse momentum spectra (left panel) and elliptic flow (right panel) for up/down quark and strange quark. Parameters are from ALICE 30-40% fit results. The case without viscous corrections is also shown.

5.2 Parameters and Data Selection

Similar to chapter 4, we utilize both transverse momentum spectra around mid-rapidity, and elliptic flow v_2 as our experimental observables. They are calculated from Eq. (5.9), (5.10) as

$$\frac{dN}{2\pi p_T dp_T dy} = \frac{1}{2\pi}\int d\theta \frac{dN}{dyd^2p_T}\,, \tag{5.20}$$

$$v_2(p_T) = \left(\frac{dN}{2\pi p_T dp_T dy}\right)^{-1} \frac{1}{2\pi}\int d\theta \cos(2\theta)\frac{dN}{dyd^2p_T}\,, \tag{5.21}$$

respectively. Note all expressions in the blastwave are taken at rapidity $y = 0$ and we have utilized matching data sets that have been taken around midrapidity.

We use data from the ALICE collaboration for Pb+Pb collisions at 2.76 TeV [53, 71, 65], in 10% centrality bins (20% for spectra of Λ, Ξ and Ω), and from the PHENIX collaboration for Au+Au collisions at 200 GeV [52, 89], in 20% centrality (10% for spectra of ϕ). For LHC, we fit seven different hadrons: $\pi^{\pm}$, K$^{\pm}$, p+$\overline{\text{p}}$, ϕ, Λ+$\overline{\Lambda}$, Ξ^-+$\overline{\Xi}^+$ and Ω^-+$\overline{\Omega}^+$. For RHIC, we fit $\pi^{\pm}$, K$^{\pm}$, p+$\overline{\mathrm{p}}$ and ϕ, then calculate Λ, Ξ^- and Ω^-. The fit ranges of spectra and v_2 are roughly 2 GeV/c $< p_T <$ 4 GeV/c for mesons and 3 GeV/c $< p_T <$ 6 GeV/c for baryons. The fit ranges for different hadrons in the same centrality bin, or for the same hadron in different centrality bins, are slightly different.

Before presenting the results, let us discuss the fit parameters used in the model. The initial parameters entering the model are $(\mu, c_s^2, \lambda, \tau, T, R_y/R_x, n, \alpha_0, \alpha_2, \eta/s)$, see chapter 2 for details. Since our main purpose here is simply a viable description of experimental data, not a precision fit of parton phase parameters, we will not focus on the precise quantities of some of the parameters but fix them at reasonable values as long as our final conclusion is not sensitive to them.

For example, we fix the temperature to be $T_c = 160$ MeV and $\mu_B = 0$, $c_s^2 = 0.15$. The value of η/s should be universal with a fixed value at T_c and $\mu_B = 0$. A preliminary round of fits for individual data sets with η/s as a fit parameter yields $2.33/4\pi$ for ALICE 20-30% centrality and $1.66/4\pi$ for ALICE 50-60% centrality. We also obtain $2.10/4\pi$ for PHENIX 20-40% centrality and $1.83/4\pi$ for PHENIX 40-60%. Thus we fit η/s to be $2/4\pi$ and we take the deviations we saw in the preliminary fits as indicative of uncertainties in the η/s extraction. A precise evaluation of η/s at T_c of course is an interesting topic and requires a more precise treatment in the future.

We carry out a similar preliminary study for λ, the scalar momentum dependence in δf. For a full theoretical understanding of λ, a microscopic calculation of the relaxation to equilibrium needs to be performed [90]. Since the departure from equilibrium is generally species-dependent, we may choose different λ for up/down quark and strange quark. In our preliminary study, we find that strange quark prefers smaller $\lambda \sim 1.5$ and up/down quark prefers values slightly above 2. We fix $\lambda = 1.5$ for strange quark and $\lambda = 2.5$ for up/down quark. We have checked that for $\lambda = 2$ which is widely used for freeze out from hydrodynamics, we get very similar final results. Following the same idea, we study the meson wave function width σ_M and baryon wave function width σ_B. Using this study we set $\sigma_M = 0.42$, $\sigma_B = 0.18$.

Valence quark mass are also fixed to be $m_{u/d} = 300$ MeV, $m_s = 480$ MeV, which are close to values used in the other literature. Since we focus here on elliptic flow and the QNS law, we do not attempt to fit the overall yield of hadrons correctly. We introduce fugacity factors $\gamma_{u/d}$ for up/down quarks and γ_s for strange quarks to enable fits to spectra at intermediate p_T. We find that $\gamma_{u/d} \approx 3\gamma_s$ consistently.

In summary, we fix the critical temperature $T_c = 160$ MeV and quark masses $m_{u/d} = 300$ MeV, $m_s = 480$ MeV. We use a viscous correction factor $\lambda = 1.5$ for strange quarks and $\lambda = 2.5$ for up/down quarks. We also set hadron wave function widths to $\sigma_M = 0.42$, $\sigma_B = 0.18$. The parameters left in our model are surface velocity α_0, velocity deformation α_2, velocity profile power n and ratio of event plane radii R_y/R_x, which will be determined by Bayesian fits to data, similar to chapter 3 and chapter 4.

5.3 Fit Results and Quarks Number Scaling

In this section we use quark recombination of the viscous blastwave at $T = T_c$ to fit experimental data and extract blastwave parameters at T_c. By doing so, we neglect the interactions between the hadrons after coalescence. In principle, elliptic flow is influenced by both the evolution in the early, partonic stages of the system and the rescattering processes in the hadronic stage. However the rescattering of intermediate p_T hadrons is suppressed as they preferentially sit in the outer layers of the fireball, with large radial flow to the outside. Thus, there is the intriguing possibility to directly probe the partonic character of anisotropic flow. The fit results are given in Tab. 5.1.

We can find that the lifetime of the fireball decreases from central to peripheral collisions, the surface velocity α_0 does not change much between different centralities and ratio of event plane radii R_y/R_x and the velocity deformation α_2 increase from central to peripheral collisions. This is expected because more peripheral collisions means less overlapping nucleons of the target and projectile, thus large initial event plane eccentricity $R_y^{(0)}/R_x^{(0)}$. As a result, one expects larger final R_y/R_x and α_2. We find that the velocity profile power n decreases from central to peripheral collisions, which means an increase of average transverse flow.

We can use the above parameters to calculate transverse momentum spectra and elliptic flow for a variety of hadrons and compare with experimental data. Fig. 5.2, 5.3 show our results for transverse momentum spectra in ALICE 30-40% and PHENIX 20-40% centrality. Fig. 5.4, 5.5

Centrality	τ (fm/c)	α_0/c	n	R_y/R_x	α_2/c
ALICE 2.76 TeV					
10-20%	12	0.818	1.37	1.397	0.0118
20-30%	10	0.822	1.37	1.542	0.0174
30-40%	8.5	0.819	1.19	1.620	0.0205
40-50%	7	0.827	1.23	1.622	0.0261
50-60%	6	0.831	1.16	1.625	0.0261
PHENIX 0.2 TeV					
10-20%	8.6	0.765	0.97	1.313	0.0142
20-40%	7.2	0.759	0.73	1.464	0.0215
40-60%	5.6	0.764	0.66	1.494	0.0332

Table 5.1: Fit parameters obtained from different centrality bins for ALICE and PHENIX data, τ is set based on proton spectra. We use critical temperature $T_c = 160$ MeV and specific shear viscosity $\eta/s = 2/4\pi$.

show our results for elliptic flow in ALICE 30-40% and PHENIX 20-40% centrality. The results for other centrality bins are provided in APPENDIX A and APPENDIX B. As one can see from Fig. 5.2, 5.3,5.4, 5.5, we obtain a rather good description via this quark recombination model.

Fig. 5.4, 5.5 are plotted with respect to transverse momentum p_T. In order to show the constituent quark number scaling, a more common way is to plot data with respect to transverse kinetic energy, $KE_T \equiv m_T - m_0$, where m_0 is the hadron mass and $m_T = \sqrt{p_T^2 + m_0^2}$ is the hadron's transverse mass, and divide v_2 and KE_T by the constituent quark number n_q. Fig. 5.6, 5.7, 5.8 show our results. For the right panel of Fig. 5.6, 5.7, 5.8, the upper lines are mesons and the bottom lines are baryons, which clearly show the deviations between mesons and baryons when $KE_T >$ 0.5 GeV, as observed in experiment. Thus our results clearly demonstrate that quark number scaling can be broken in quark recombination, and that a consistent picture can exist between RHIC and LHC data despite the varying degree of violation of the QNS law.

5.4 Resonance Recombination

In order to extend instantaneous recombination to low p_T, we introduce resonance recombination model in this section. For details, we recommend the reader to check Ref. [62, 63, 57]. Below, the 4-momentum of meson M is written as $p^\mu = (p^0,\ \mathbf{p})$, with energy $E_M = p^0 = \sqrt{m^2 + p^2}$ and

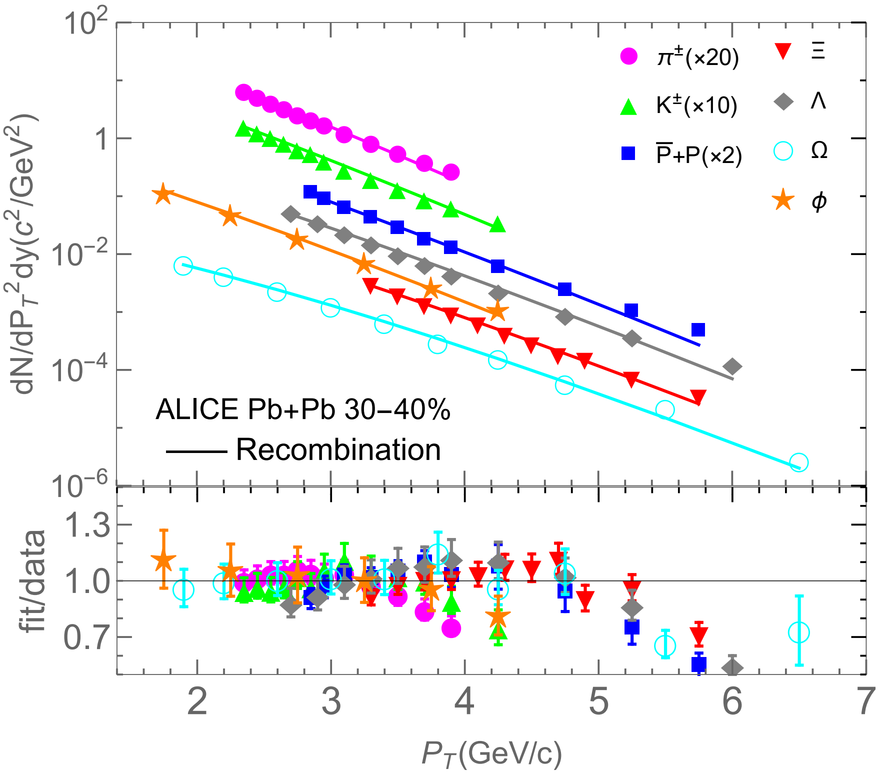

Figure 5.2: Transverse momentum spectra for $\pi^{\pm}$, K$^{\pm}$, p+$\bar{\text{p}}$, ϕ, Λ+$\overline{\Lambda}$, Ξ^-+$\overline{\Xi}^+$ and Ω^-+$\overline{\Omega}^+$ in the ALICE 30-40% centrality bin. Λ, Ξ and Ω are from 20-40% centrality bin. Symbols are experimental data, solid lines are recombination calculation. Parameters are given Tab. 5.1.

3-momentum $\mathbf{p}$ and meson mass m. The 4-momentum of quark q and anti-quark $\bar{q}$ are written as $p_1^\mu = (E_1,\ \mathbf{p_1})$ and $p_2^\mu = (E_2,\ \mathbf{p_2})$ with $E_1 = \sqrt{m_1^2 + p_1^2}$, $E_2 = \sqrt{m_2^2 + p_2^2}$ respectively together with quark masses m_1 and m_2.

In Ref. [62, 63, 57], quark coalescence was interpreted as a process similar to the formation of resonances, $q + \overline{q} \rightleftharpoons M$, and described through a Boltzmann equation

$$p^\mu \partial_\mu f_M(t, \mathbf{x}, \mathbf{p}) = -m\Gamma f_M(t, \mathbf{x}, \mathbf{p}) + p^0 \beta(\mathbf{x}, \mathbf{p}), \tag{5.22}$$

where $f_M(t, \mathbf{x}, \mathbf{p})$ is the phase-space distribution of the meson, $\mathbf{x}$ is its 3-position and the gain term

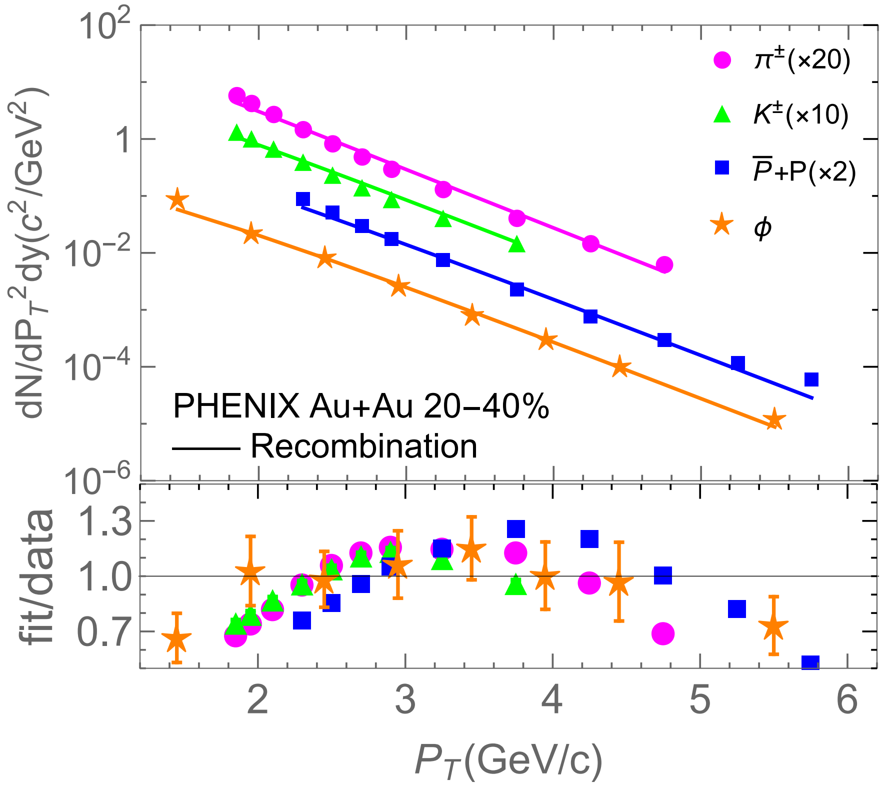

Figure 5.3: Same as Fig. 5.2 in the PHENIX 20-40% centrality bin. ϕ is from 20-30% centrality bin.

is given by

$$\beta(\mathbf{x},\mathbf{p}) = \int \frac{d^3p_1 d^3p_2}{(2\pi)^6}\; f_q(\mathbf{x},\mathbf{p_1}) f_{\bar{q}}(\mathbf{x},\mathbf{p_2})\; \sigma(s)\; v_{\rm rel}(\mathbf{p_1},\mathbf{p_2})\; \delta^3(\mathbf{p}-\mathbf{p_1}-\mathbf{p_2}), \tag{5.23}$$

where $\sigma(s)$ is the cross section for the process $q+\bar{q}\to M$ at center-of-mass (CM) energy squared $s=(p_1^\mu+p_2^\mu)^2$, $f_{q,\bar{q}}$ are quark and anti-quark phase space distribution functions and the relative velocity is $v_{\rm rel}=|\frac{\mathbf{p_1}}{E_1}-\frac{\mathbf{p_2}}{E_2}|$. The explicit cross section automatically satisfies energy-momentum conservation and can be modeled by a relativistic Breit-Wigner form,

$$\sigma(s) = g_\sigma \frac{4\pi}{k^2}\frac{(\Gamma m)^2}{(s-m^2)^2+(\Gamma m)^2}, \tag{5.24}$$

where g_σ is the spin degeneracy factor, Γ is the reaction rate, same as the first term on the right-

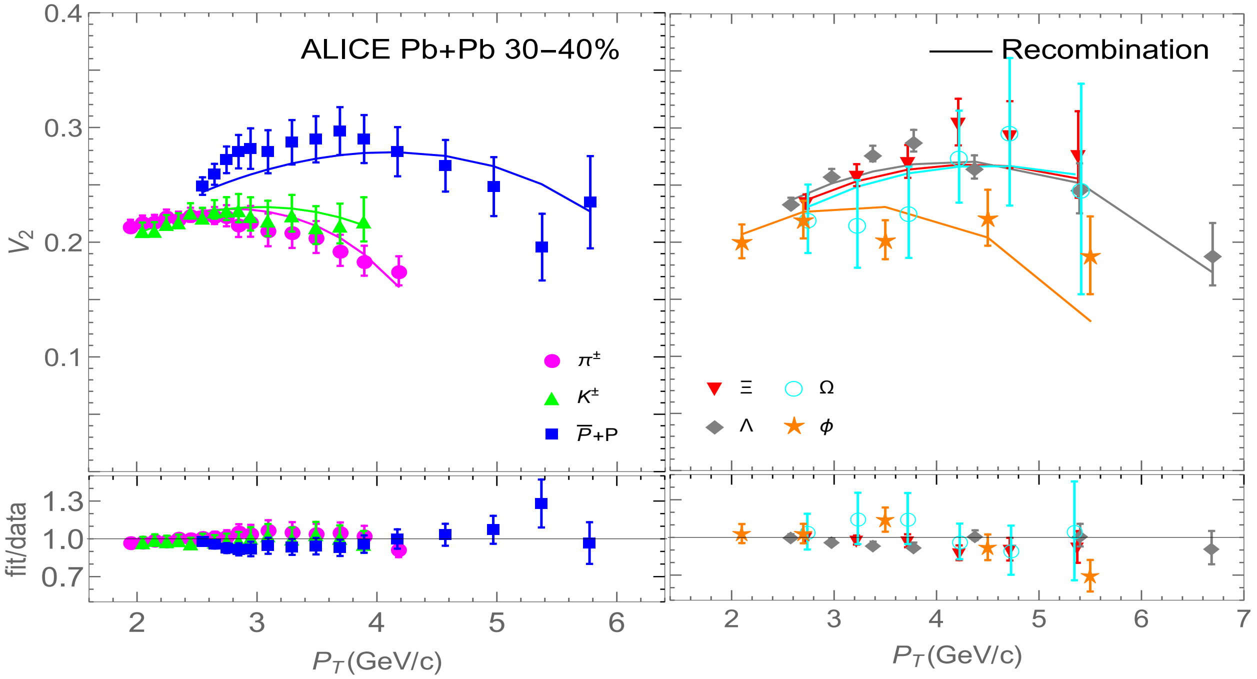

Figure 5.4: Elliptic flow v_2 for $\pi^{\pm}$, K$^{\pm}$ and p+$\overline{\text{p}}$ (left panel) and ϕ, Λ+$\overline{\Lambda}$, Ξ^-+$\overline{\Xi}^+$ and Ω^-+$\overline{\Omega}^+$ (right panel) in the ALICE 30-40% centrality bin. Symbols are experimental data, solid lines are recombination calculation. Parameters are given Tab. 5.1.

hand-side (RHS) of Eq. (5.22), and k denotes the quark 3-momentum in the CM frame. Introducing the notation $\mathbf{p} = \mathbf{p_1} + \mathbf{p_2}, \mathbf{q} = \frac{1}{2}(\mathbf{p_1} - \mathbf{p_2})$, we can rewrite Eq. (5.23) as

$$\beta(\mathbf{x}, \mathbf{p}) = \int \frac{d^3q}{(2\pi)^3} f_q(\mathbf{x}, \mathbf{p}, \mathbf{q}) f_{\bar{q}}(\mathbf{x}, \mathbf{p}, \mathbf{q}) \, \sigma(s) \, v_{rel}(\mathbf{p}, \mathbf{q}) \tag{5.25}$$

Integrating Eq. (5.22) over the fireball volume, the integral of the left-hand-side (LHS) gives

$$p^0 \frac{\partial}{\partial t} \int d^3x f_M(t, \mathbf{x}, \mathbf{p}) + \mathbf{p} \cdot \int d^3x \nabla f_M(t, \mathbf{x}, \mathbf{p}) = p^0 \frac{\partial}{\partial t} f_M^{(p)}(t, \mathbf{p}) \tag{5.26}$$

here $f_M^{(p)}(t, \mathbf{p}) = \int d^3x f_M(t, \mathbf{x}, \mathbf{p})$ is the momentum distribution of the meson and the second term vanishes due to

$$\mathbf{p} \cdot \int d^3x \nabla f_M(t, \mathbf{x}, \mathbf{p}) = \int d^3x \nabla [\mathbf{p} f_M(t, \mathbf{x}, \mathbf{p})] = 0 \tag{5.27}$$

If hadronization is rapid enough to produce hadrons in equilibrium, e.g. in the long-time limit,

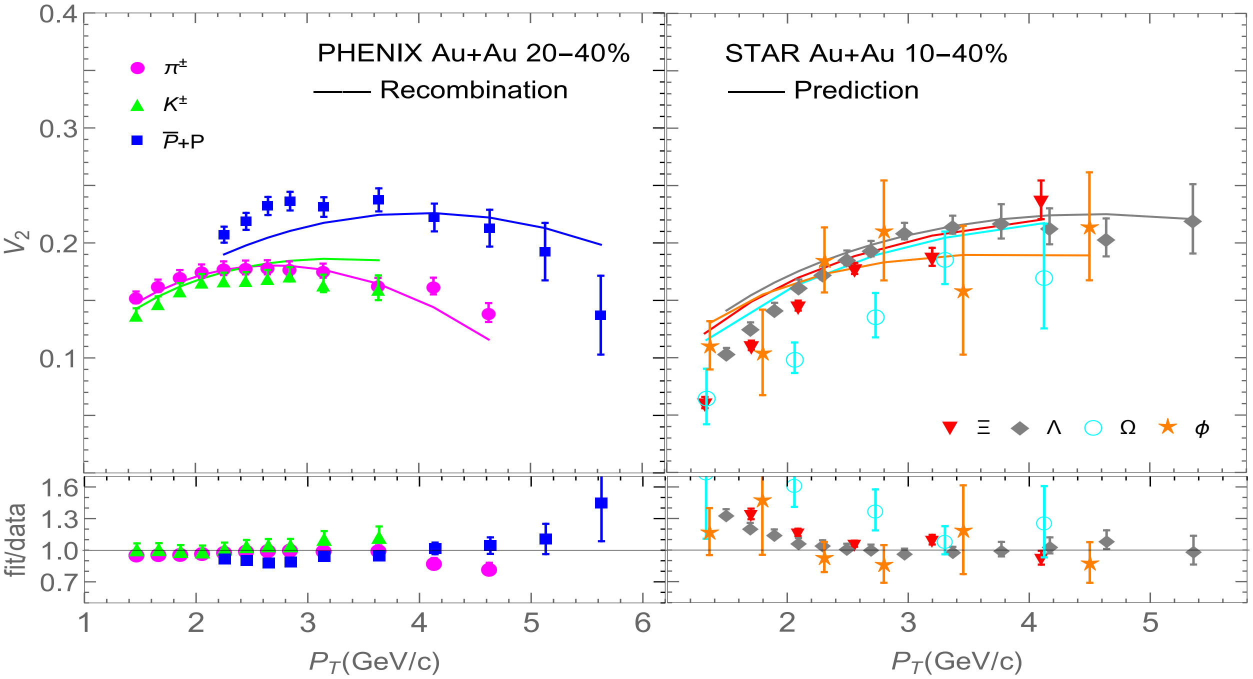

Figure 5.5: Elliptic flow v_2 for $\pi^\pm$, $\mathrm{K}^\pm$ and p+$\overline{\mathrm{p}}$ in the PHENIX 20-40% centrality bin (left panel) and ϕ, Λ+$\overline{\Lambda}$, Ξ^-+$\overline{\Xi}^+$ and Ω^-+$\overline{\Omega}^+$ in the STAR 10-40% centrality bin (right panel). Ω is from the STAR 0-80% centrality bin. Symbols are experimental data, solid lines are recombination calculation. Note: we only fit π, K and p, right panel is calculated using the same parameter as left panel.

$1/\Gamma \ll \Delta\tau$, we have the equilibrium limit condition

$$\frac{\partial}{\partial t} f_M^{(p)}(t, \mathbf{p}) = 0 \tag{5.28}$$

Using Eq. (5.26)(5.28), the integral of the LHS of Eq. 5.22 vanishes and the integral of the RHS gives

$$\int d^3x f_M^{eq}(\mathbf{x}, \mathbf{p}) - \int d^3x \frac{p^0}{m\Gamma}\beta(\mathbf{x}, \mathbf{p}) = 0 \tag{5.29}$$

Using the above equation, the number of mesons is given by

$$N_M^{eq} = \int \frac{d^3x\ d^3p}{(2\pi)^3} f_M^{eq}(\mathbf{x}, \mathbf{p}) = \int \frac{d^3x\ d^3p}{(2\pi)^3} \frac{p^0}{m\Gamma}\beta(\mathbf{x}, \mathbf{p}) \tag{5.30}$$

and the invariant transverse momentum spectra

$$p^0 \frac{dN_M}{d^3p} = \frac{dN_M}{d^2p_T\, dy} = p^0 \int \frac{d^3x}{(2\pi)^3} \frac{p^0}{m\Gamma} \beta(\mathbf{x}, \mathbf{p}) \tag{5.31}$$

Now, what left is to work out the expression of CM energy squared s and 3-momentum k. From $\mathbf{p} = \mathbf{p_1} + \mathbf{p_2}, \mathbf{q} = \frac{1}{2}(\mathbf{p_1} - \mathbf{p_2})$, we can easily write

$$\mathbf{p_1} = \frac{1}{2}\mathbf{p} + \mathbf{q}, \qquad \mathbf{p_2} = \frac{1}{2}\mathbf{p} - \mathbf{q}. \tag{5.32}$$

with Eq. (5.32) we can rewrite expressions in terms of $\mathbf{p}$ and $\mathbf{q}$. In the lab frame, the center-of-mass (CM) energy squared is

$$s = (E_1 + E_2)^2 - (\mathbf{p_1} + \mathbf{p_2})^2 = (E_1 + E_2)^2 - \mathbf{p^2} \tag{5.33}$$

which is a Lorentz invariant. In the CM frame, the quark 4-momentum can be written as

$$p_1' = (\sqrt{m_1^2 + k^2}, \mathbf{k}), \qquad p_2' = (\sqrt{m_2^2 + k^2}, -\mathbf{k}) \tag{5.34}$$

$$s = (p_1' + p_2')^2 = (\sqrt{m_1^2 + k^2} + \sqrt{m_2^2 + k^2})^2 \tag{5.35}$$

thus we get the expression for $\mathbf{k}$

$$k^2 = \frac{1}{4s}(s + m_1^2 - m_2^2)^2 - m_1^2. \tag{5.36}$$

This concludes the overview of the RRM model. Now we apply RRM to the blastwave at T_c extracted earlier in order to calculate the elliptic flow of ϕ mesons with the same blastwave parameters fitted before. Interestingly, we find rather compatible results with the instantaneous recombination model, see Fig. 5.9, 5.10. From Fig. 5.9, 5.10, we can find the elliptic flow of instantaneous and RRM recombination are the same when there is no viscous corrections δf. And when δf is included, the deviations occur only at high transverse momentum. In the future, we plan to explore similarities between instantaneous and RRM recombination in greater detail.

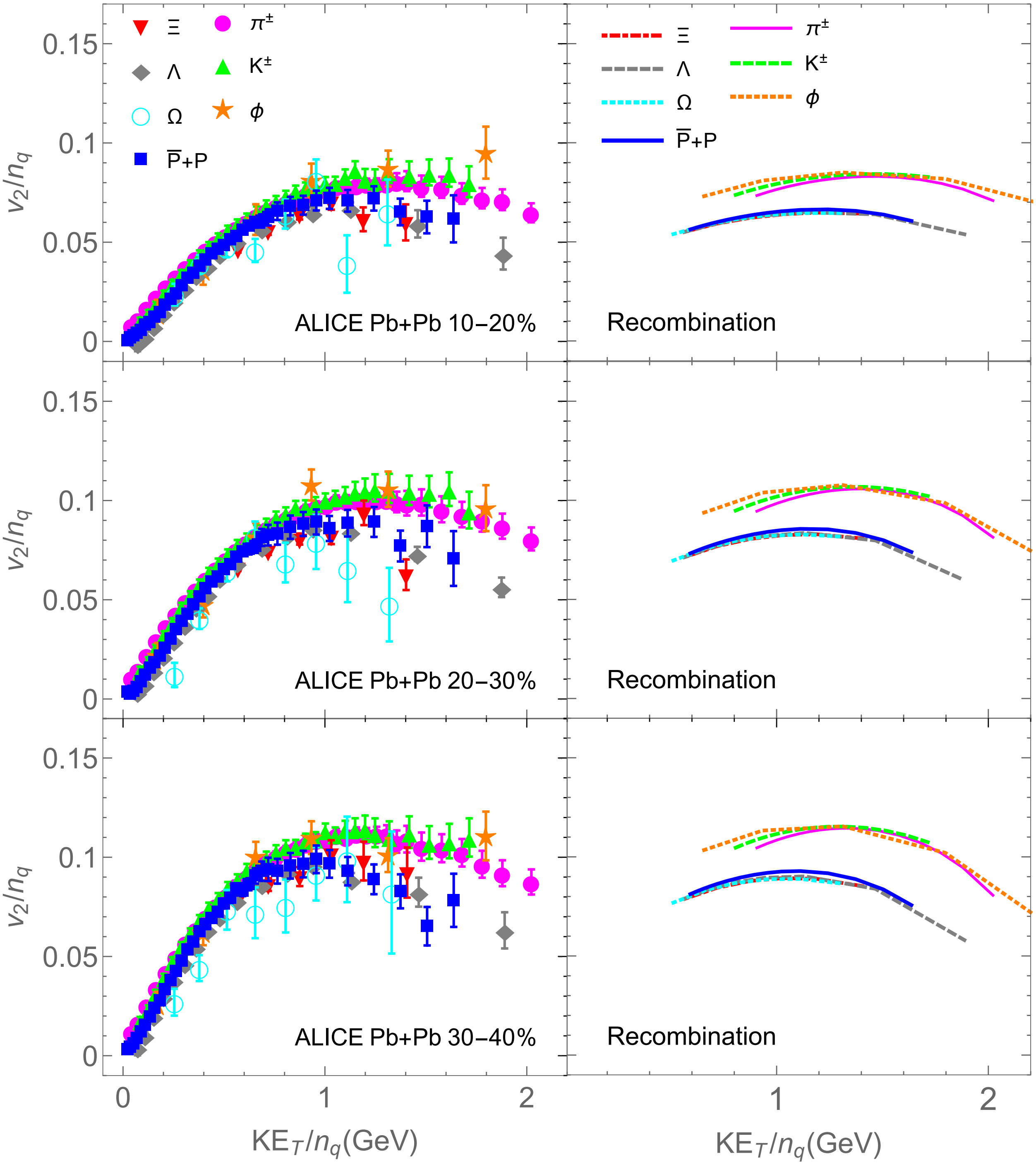

Figure 5.6: Elliptic flow for $\pi^{\pm}$, K$^{\pm}$, p+$\overline{\text{p}}$, ϕ, Λ+$\overline{\Lambda}$, Ξ^{-}+$\overline{\Xi}^{+}$ and Ω^{-}+$\overline{\Omega}^{+}$ in the ALICE 10-20% (top), 20-30% (middle) and 30-40% (bottom) centrality bin. Symbols are experimental data (left panel), lines are recombination calculation(right panel). In the right panel, the upper lines are mesons and the lower lines are baryons.

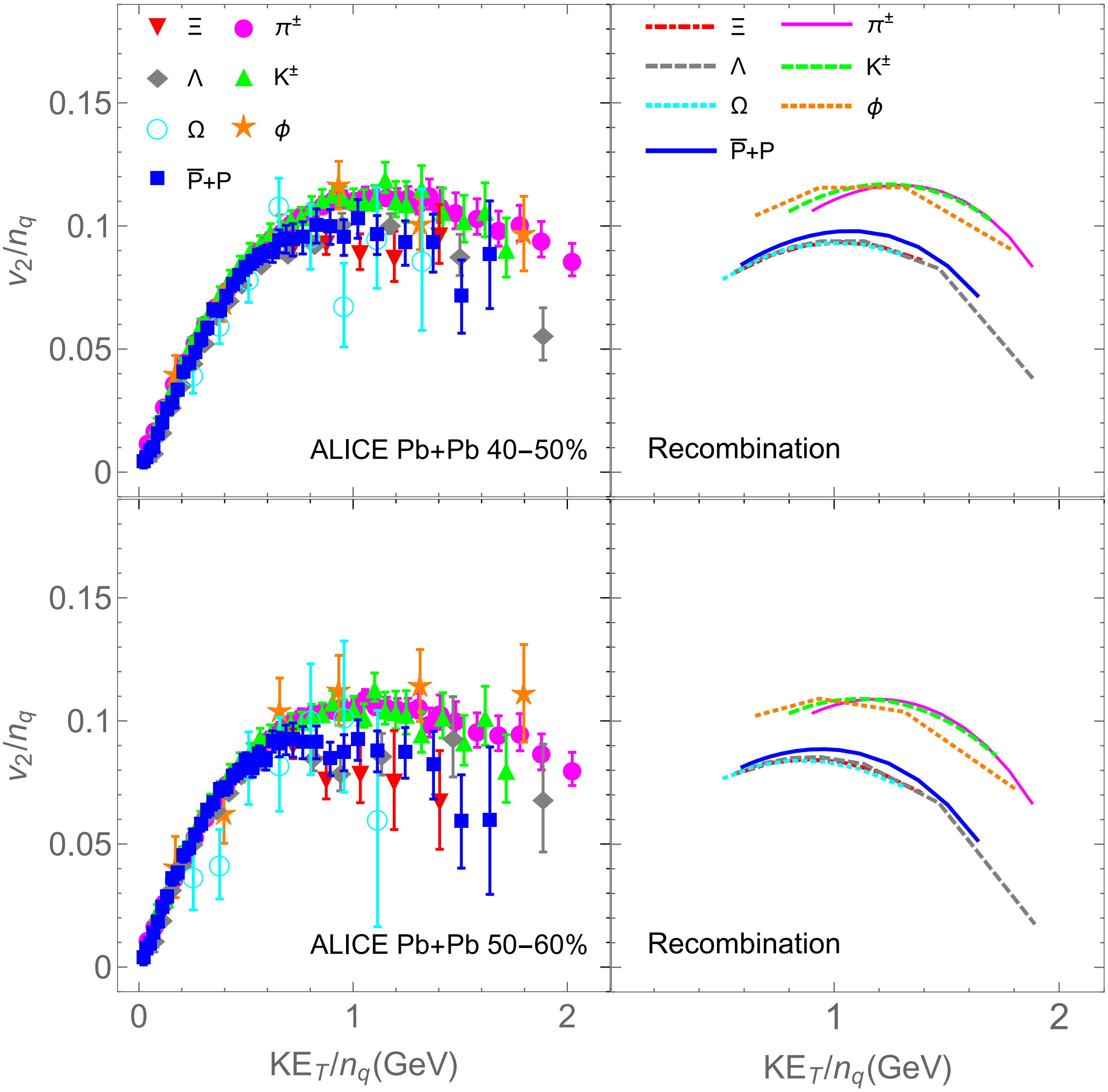

Figure 5.7: Same as Fig. 5.6 in the ALICE 40-50% (top) and 50-60% (bottom) centrality bin. Symbols are experimental data, lines are recombination calculation. In the right panel, the upper lines are mesons and the lower lines are baryons.

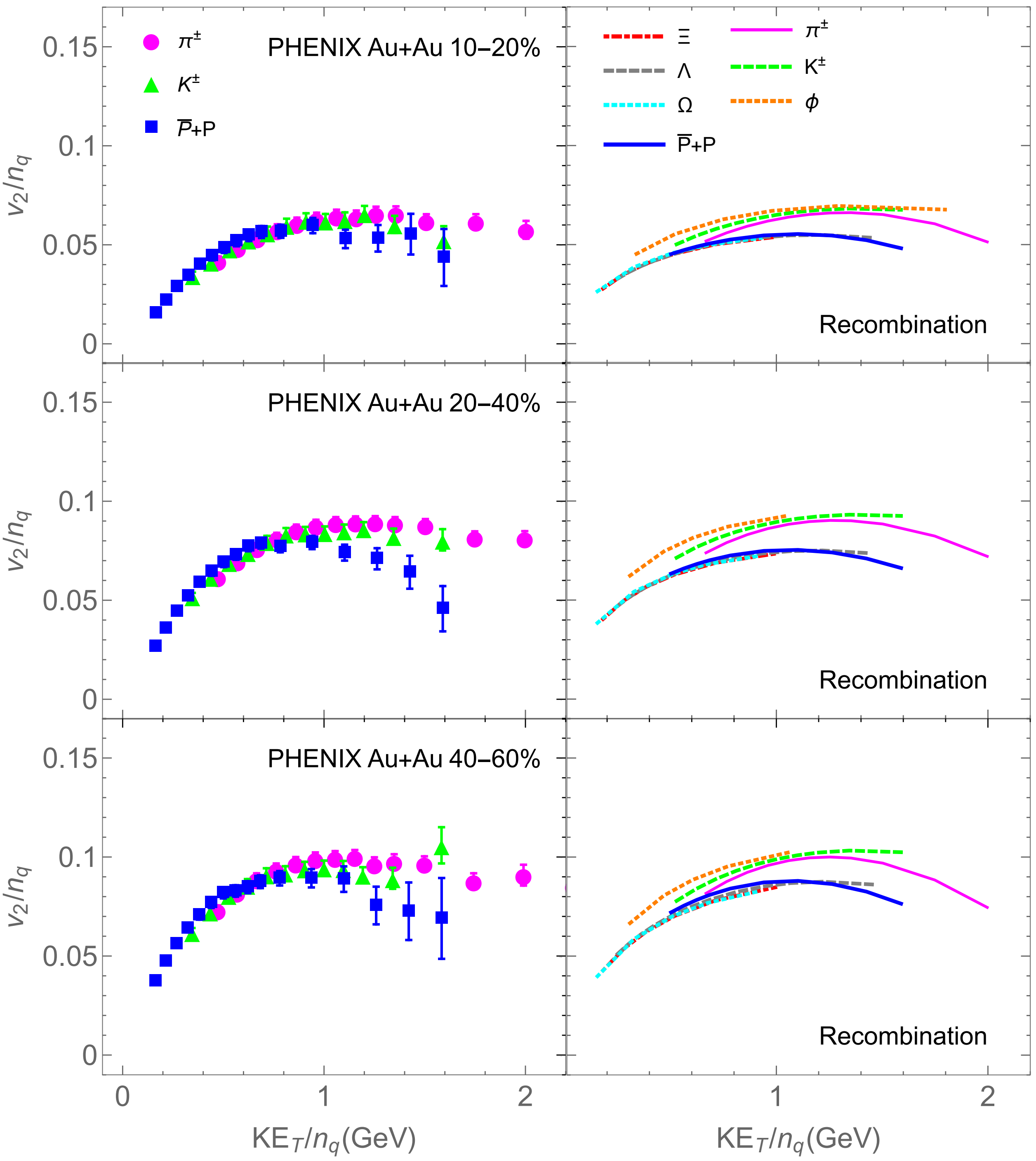

Figure 5.8: Same as Fig. 5.6 in the PHENIX 10-20% (top), 20-40% (middle) and 40-60% (bottom) centrality bin. Symbols are experimental data, lines are recombination calculation. In the right panel, the upper lines are mesons and the lower lines are baryons.

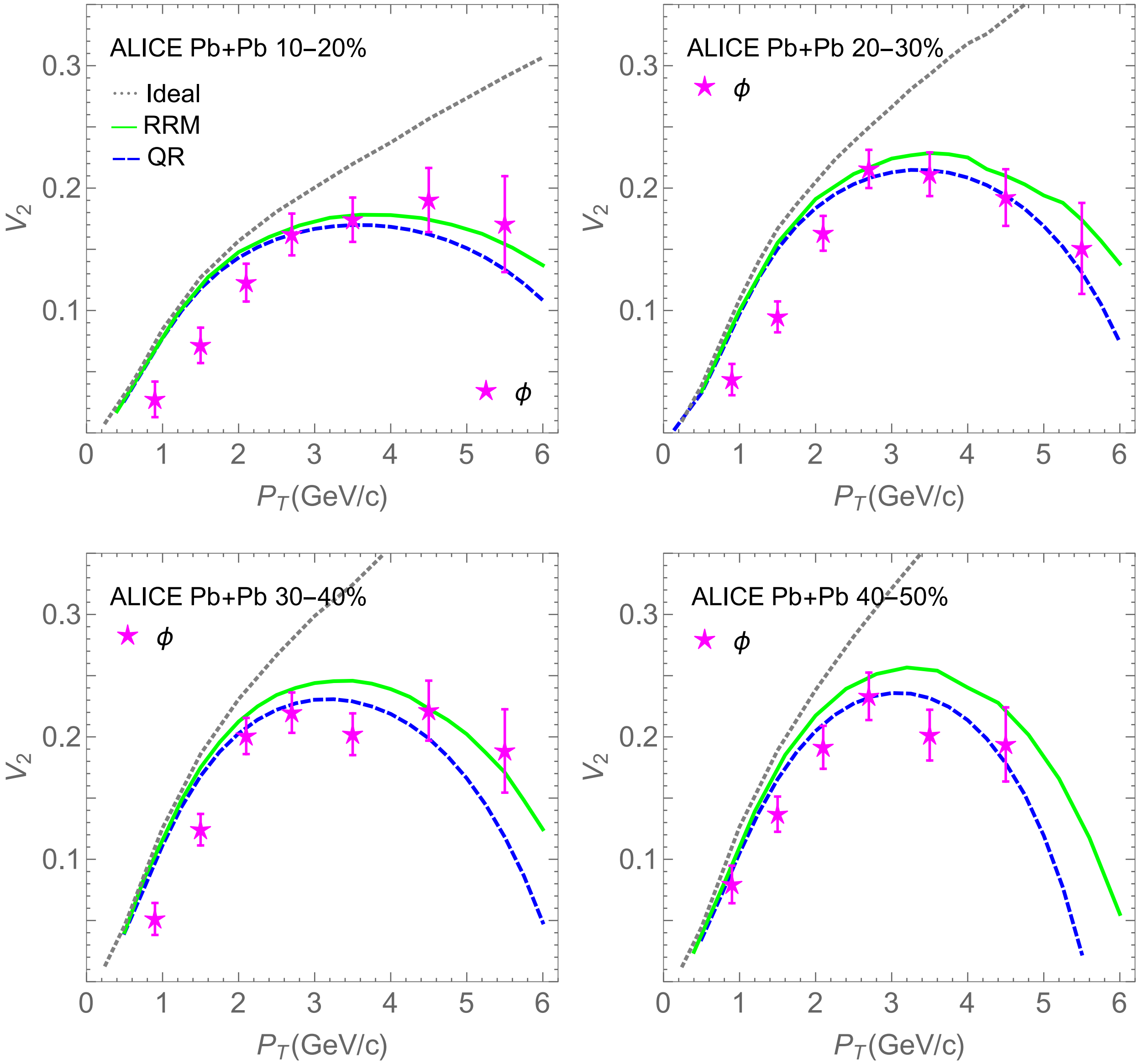

Figure 5.9: Elliptic flow of phi meson from RRM. Parameters are the same as the instantaneous quark recombination fit results. For the case without viscous corrections, both models obtain the same elliptic flow.

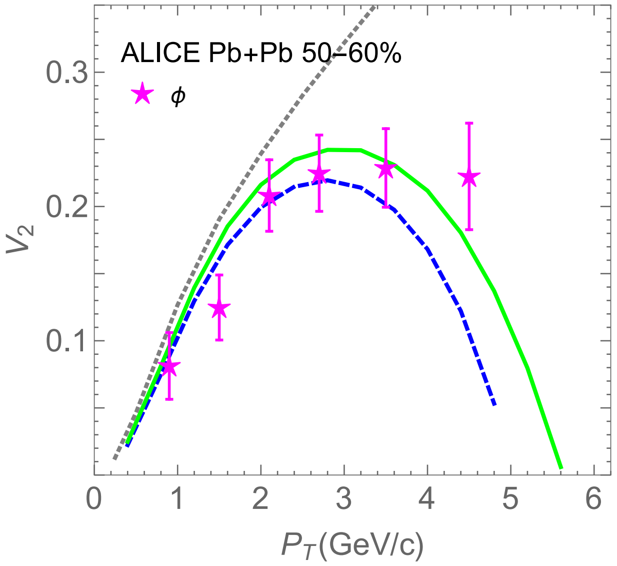

Figure 5.10: Elliptic flow of phi meson from RRM. Parameters are the same as the instantaneous quark recombination fit results. For the case without viscous corrections, both models obtain the same elliptic flow.

6. SUMMARY AND OUTLOOK

In this work, we have constructed a blastwave model with self-consistent viscous corrections based on the Retiere and Lisa (RL) ideal blastwave. The non-equilibrium deformations of particle distributions due to shear viscosity were integrated into the blastwave. We used the Navier-Stokes approximation and calculated the viscous stress tensor from the gradient of the flow field. The spatial derivatives can be obtained directly from the parameterized flow field. The time derivatives can not be given by the blastwave itself, but can be obtained by solving the ideal hydrodynamic equations of motion analytically. It turns out time derivatives are indeed important for viscous stress tensor. In our previous work, we obtained rather small $\eta/s \sim 1/4\pi$ when using free streaming for the time derivatives [66]. By using a more realistic flow field and by calculating the time derivative terms, we provided a more realistic blastwave than previous work.

The parameters in the blastwave are extracted from experimental data (or hydro pseudo data). We have used the statistical analysis package from MADAI project [70] to determine fit parameters. The MADAI package includes a Gaussian process emulator and a Bayesian analysis tool. Basically, we generate a set of training points in parameter space and calculate all fitted observables at each training point. The package then builds a Gaussian process emulator to estimate observables for random parameter values. Finally a Markov Chain Monte Carlo provides a likelihood analysis and gives the maximum likelihood parameters and uncertainties. Comparing with the regular χ^2 method, the statistical package has two benefits. First, the Gaussian emulator saves computing time. Otherwise, one needs to carry out massive computing tasks over the parameter space. It may be proper for a small number of parameters ($n \leq 4$), but not for a large number of parameters ($n \geq 5$). For the statistical package, one only needs to calculate few hundreds or less training points. Second, it provides a likelihood distribution for each parameter and also the correlations between them. With likelihood analysis figures, it is simple and straightforward to find the probabilities and correlations of parameters, which one cannot obtain from the χ^2 method.

Once we have established the blastwave model, we validated it by comparison with hydrodynamic calculations. In particular, we systematically compared our blastwave to hydrodynamic calculations with resonance decays and bulk stress included. If we believe experimental data can be approximated by hydro simulations and hydrodynamic system can be approximated by blastwave, a general question is how well the extracted parameters reflect the "true" values. The "true" here refers to values that could have been inferred using hydrodynamic calculation. To answer this question, we utilized the viscous hydrodynamics code MUSIC and generated a set of events at different temperature and with various specific viscosity in the T_{fo}-η/s-plane. Then we extracted the flow field from spectra and elliptic flow v_2 of these hydrodynamic calculations with our viscous blastwave. Especially we compared the extracted freeze-out temperature T_{fo} and specific viscosity η/s to values used in hydrodynamics and obtained the mapping matrix between them.

We found that the extracted specific shear viscosities were mostly consistent with true values within uncertainties. However the extracted temperature was distorted and it underestimated the true temperature significantly at high T. The extracted T_{fo} is about 15 MeV lower for hydro events at high temperature (or peripheral collisions). For events at low freeze-out temperature (or central collisions), the extracted T_{fo} are very close to the true temperature within ± 5 MeV. We then parameterized a mapping matrix to remove uncertainties and bias from the simplifications of hypersurface and flow field in blastwave and unfolded the blastwave fit results of experiment measurement. In the future we can extend the comparison to other observables such as hypersurface and radial flow at freeze-out.

For further improvement, it is possible to include resonance decays and bulk stress in the blastwave. In principle, blastwave would provide a more realistic description of experimental data if it includes resonance decays and bulk stress. The advantage of blastwave is its simplicity, which provides an alternative option to running numerically expensive hydrodynamics. If one has to include resonance decays, blastwave would become much more complicated and lose some of its simplicity. Of course, even in this case, blastwave is numerically less expensive than hydrodynamics. For the blastwave with resonance decays, we recommend the readers to check Ref. [50, 91, 92]. As far as we know, the blastwave with bulk stress has not been attempted yet. It would be interesting to develop such a blastwave in the future but it is beyond the scope of this work.

As a first major outcome, we have built an improved and viscous blastwave and quantified the uncertainties and biases in temperature and shear viscosity. Blastwaves have been used by theorists and experimentalists in the past. If systematic uncertainties from blastwave fits could be quantified, blastwaves would be a more widely accepted tool for quantitative analyses. This work is a first step in this direction. And in fact, we have shared our code with J. Schukraft from ALICE Collaboration.

As one of the main goals of this work, we applied our blastwave to extract the kinetic freeze-out temperature $T_{\rm fo}$ and the specific shear viscosity η/s of hot hadronic matter from experimental data. The transport properties of this hot hadronic matter are important properties of QCD that we want to learn from the experimental program. They also influence the transport properties extracted for the QGP, because all experimental information on the transport properties of QGP must be extracted from final state hadrons. We have verified it is possible to estimate η/s of the hot hadronic matter at the kinetic freeze-out in a way independent from existing methods. Especially, our approach is complementary to existing extractions from viscous hydrodynamics. The latter is sensitive to an averaged shear viscosity during that time evolution while our analysis is only sensitive to the shear viscosity at kinetic freeze-out. We found that η/s of hadronic matter is consistent with estimates for η/s of QGP around T_c. We also found a smooth and gradual rise of η/s below T_c.

As discussed in chapter 1, AdS/CFT correspondence predicts a universal lower bound of $\eta/s = 1/4\pi$ for the specific shear viscosity [25]. And lattice calculations find η/s to be close to the conjectured lower bound around T_c with a rather slow rise towards higher temperatures [41, 42, 43, 44]. However, pushing these calculations into the hadronic phase below T_c turns out to be difficult. The early calculations used viscous hydrodynamics with a fixed, temperature-independent η/s as a parameter and hydrodynamics was run all the way to kinetic freeze-out at the end of hadronic phase. They find a rather small $\eta/s \sim 2.5/4\pi$ [40]. The value of η/s extracted from this method is averaged over the entire temperature evolution of the QGP and the hot hadronic matter below T_c.

Subsequently, several groups argued that the low viscosity extracted from viscous hydrodynamics originated from the partonic phase and the viscosity would increase rapidly when nuclear matter transit from partonic phase to hadronic phase. In this case, the hadronic phase should be described by hadronic transport models other than viscous hydrodynamics. This argument was aided by estimates of η/s for a hadronic matter from hadronic transport models. While these calculations do not agree quantitatively, they generally find rather large specific shear viscosity for hot hadronic matter. For example, both URQMD [35] and SMASH [37] obtained $\eta/s \gtrsim 10/4\pi$ even very close to T_c.

Two reasons may explain the extremely large value of η/s near T_c in URQMD and SMASH. First, it can partially come from the absence of non-unit fugacities or finite chemical potentials for hadrons. As shown in Ref. [35], by inducing non-unit fugacities $\lambda_{\pi,K}$= exp$(\mu_{\pi,K}/T)$ $\sim$ 1.2-1.7, η/s decreased from $12/4\pi$ to $7/4\pi$ near T_c. Based on our blastwave fit results, finite chemical potentials are necessary to describe experimental data when the system cools down after chemical freeze-out; see Tab. 4.2. The reduction in η/s can be understood, since non-unit fugacity in this case means an increase in particle density and an increased particle density leads to a reduced mean free path, which in turn reduces the viscosity [35].

Second, it comes from the treatment of hadronic interactions through resonances, which have a non-zero lifetime. As shown in Ref. [37], introducing point-like interaction scenarios and adding an overall elastic cross-section σ=10 mb, η/s in a system of pions can decrease from $10/4\pi$ to $4/4\pi$ near T_c. The reduction in η/s can be understood from the relaxation dynamics. From theoretical calculation [93], we have $\eta \sim \rho\tau\bar{v}_{rel}$, where τ is the relaxation time and $\bar{v}_{rel} \approx 1$ here. When the resonance lifetime τ_{life} is much smaller than the mean free time τ_{mft} (the inverse of the scattering rate), the relaxation time τ is not affected by the resonance lifetime and $\tau \sim \tau_{\text{mft}}$. When $\tau_{\text{life}} \gg \tau_{\text{mft}}$, the relaxation to equilibrium from resonance scattering is delayed. In Ref. [37], the authors have checked that by including a large elastic point-like interaction, $\tau \sim \tau_{\text{mft}}$ is restored. In this case, when temperature increases toward T_c, τ_{mft} will decrease (as scattering rate increases) and τ will decrease and reach its minimum near T_c, which in turn gives a minimum value of η/s near T_c. This is similar to the result of B3D [86, 94], which obtains rather small $\eta/s \sim 3/4\pi$ near T_c.

The discrepancies between URQMD, SMASH and B3D are then qualitatively understood. First, both URQMD and SMASH used Green-Kubo formalism to calculate the shear viscosity η and obtained consistent results. The smaller η/s given by SMASH came from the fact that SMASH used a larger $\pi^+\pi^-$ cross section than URQMD, especially at low temperatures $T \sim$ 80-100 MeV [37]. As a comparison, B3D extracted η/s directly from fits of evolution equations of the energy-momentum tensor π^{zz}, calculated from simulation using B3D code [95]. Besides, B3D included an overall elastic cross-section σ=10 mb in addition to resonance cross sections. As discussed in Ref. [37], this may explain why B3D obtained much smaller η/s than other transport models. However, the question remains which model describes physics correctly. Also, the interactions between hadrons are modeled using the cross sections and properties of hadrons at T=0 [96] or from dilepton spectra [97]. From lattice QCD studies, it is known that the transition between QGP and hadronic matter is not a true, sharp phase transition but rather an analytic cross-over transition. As a result, very sharp features in the temperature dependence of η/s are not expected.

Our results suggest that there is no tension between η/s on the QGP and hadronic side of the cross-over. For a long time, the term "hadron gas" was used to name the hadronic matter below T_c, due to the results given by hadronic transport calculations that the viscosity increased rapidly when nuclear matter transit from partonic phase to hadronic phase. However, our results show a smooth and gradual rise of η/s below T_c, which indicates a strong-interaction character of hadronic matter near T_c. This is consistent with results given by Ref. [97], as they found the ρ meson width approaches its mass when the system moves from low temperature toward T_c. For this reason, we would rather use "hadronic matter" instead of "hadron gas". **If confirmed, our results show the hadronic matter just below T_c has a relatively small η/s.**

Another main goal of this work is to use the viscous blastwave to provide realistic input for quark recombination models. The importance of quark recombination is that it allows us to directly probe the partonic characters by extracting blastwave parameters at T_c, such as the p_T spectra and anisotropic flow of partons. In quark recombination models, valence quarks are assumed to be abundant in phase space at $T = T_c$ and recombine to hadrons through quark recombination. In this thesis, we followed the previous work [59, 60]. We parameterize the quark distributions at $T \approx T_c$ using the viscous blastwave and then use recombination to get spectra and elliptic flow v_2 of identified hadrons at intermediate transverse momentum p_T (2 GeV/$c < p_T < 6$ GeV/c). The parameters of the blastwave are fitted to data in this p_T range. This work extended the previous study in the following aspects. In Ref. [59, 60], kinetic equilibrium was broken in a naive way and elliptic flow of quarks was implemented locally, in which space-momentum correlations were neglected. Now by adding viscous corrections, we provided a physical way to break kinetic equilibrium and stop the growth of v_2 at $p_T > 2$ GeV/c and had realistic space-momentum correlations.

In addition, it was widely believed that the constituent quark number scaling (QNS) law was a necessary feature of quark recombination, and that violations of the QNS law found experimentally can be interpreted as evidence against quark recombination. Indeed, data from LHC shows the elliptic flow of identified hadrons following the QNS law to a lesser extent than data from RHIC [64]. Recent publication from ALICE report deviations from QNS law for Pb-Pb collisions [65]. They find significant deviations for the intermediate region $(m_T - m_0)/n_q \sim 0.8 - 2$ GeV/c^2 and the scaling law exhibits deviations at the level of $\pm 20\%$. In this work, we checked the QNS law by fitting v_2 of different hadrons at a variety of collision energies and impact parameters. For RHIC, we fit v_2 of $\pi^{\pm}$, K$^{\pm}$, p+$\overline{\text{p}}$ and ϕ, and also calculate results for Λ, Ξ^- and Ω^-. For LHC, we fit v_2 of $\pi^{\pm}$, K$^{\pm}$, p+$\overline{\text{p}}$, ϕ, Λ+$\overline{\Lambda}$, Ξ^-+$\overline{\Xi}^+$ and Ω^-+$\overline{\Omega}^+$. The overall description was rather good and we find violations of the QNS up to 14% for RHIC and 24% for LHC, which is consistent with experimental data. **Thus we demonstrate that the QNS law is not a necessary feature of quark recombination and that quark recombination remains a viable method to describe hadron production at intermediate momenta in heavy ion collision.**

REFERENCES

[1] Z. Fodor and S. D. Katz, J. High Energy Phys. **0404**, 050 (2004).

[2] PHENIX, A. Adare *et al.*, Phys. Rev. Lett. **98**, 162301 (2007).

[3] STAR, J. Adams *et al.*, Phys. Rev. Lett. **92**, 052302 (2004).

[4] STAR, J. Adams *et al.*, Phys. Rev. Lett. **95**, 122301 (2005).

[5] J. C. Collins and M. J. Perry, Phys. Rev. Lett. **34**, 1353 (1975).

[6] E. V. Shuryak, Phys. Lett. **78B**, 150 (1978), [Yad. Fiz. **28**, 796 (1978)].

[7] M. Gyulassy and L. McLerran, Nucl. Phys. A **750**, 30 (2005).

[8] E. Shuryak, Prog. Part. Nucl. Phys. **62**, 48 (2009).

[9] P. F. Kolb, P. Huovinen, U. W. Heinz, and H. Heiselberg, Phys. Lett. B **500**, 232 (2001).

[10] P. Huovinen, P. F. Kolb, U. W. Heinz, P. V. Ruuskanen, and S. A. Voloshin, Phys. Lett. B **503**, 58 (2001).

[11] P. F. Kolb and U. W. Heinz, *preprint* (2003), arXiv:nucl-th/0305084.

[12] U. Heinz and R. Snellings, Ann. Rev. Nucl. Part. Sci. **63**, 123 (2013).

[13] L. D. Landau, Izv. Akad. Nauk Ser. Fiz. **17**, 51 (1953).

[14] H. Song and U. W. Heinz, Phys. Rev. C **77**, 064901 (2008).

[15] B. Schenke, S. Jeon, and C. Gale, Phys. Rev. C **82**, 014903 (2010).

[16] A. Kovner, L. D. McLerran, and H. Weigert, Phys. Rev. D **52**, 3809 (1995).

[17] G. Chen, R. J. Fries, J. I. Kapusta, and Y. Li, Phys. Rev. C **92**, 064912 (2015).

[18] M. L. Miller, K. Reygers, S. J. Sanders, and P. Steinberg, Ann. Rev. Nucl. Part. Sci. **57**, 205 (2007).

[19] F. Cooper and G. Frye, Phys. Rev. D **10**, 186 (1974).

[20] U. Heinz, Journal of Physics G: Nuclear and Particle Physics **31**, S717 (2005).

[21] W. Israel and J. M. Stewart, Annals Phys. **118**, 341 (1979).

[22] P. Romatschke and U. Romatschke, Phys. Rev. Lett. **99**, 172301 (2007).

[23] K. Dusling and D. Teaney, Phys. Rev. C **77**, 034905 (2008).

[24] B. Schenke, S. Jeon, and C. Gale, Phys. Lett. B **702**, 59 (2011).

[25] P. Kovtun, D. T. Son, and A. O. Starinets, Phys. Rev. Lett. **94**, 111601 (2005).

[26] D. Teaney, Phys. Rev. C **68**, 034913 (2003).

[27] H. Song, S. A. Bass, and U. Heinz, Phys. Rev. C **83**, 024912 (2011).

[28] H. Song, S. A. Bass, U. Heinz, T. Hirano, and C. Shen, Phys. Rev. C **83**, 054910 (2011), [Erratum: Phys. Rev. C **86**, 059903 (2012)].

[29] M. Prakash, M. Prakash, R. Venugopalan, and G. Welke, Phys. Rept. **227**, 321 (1993).

[30] S. Muroya and N. Sasaki, Prog. Theor. Phys. **113**, 457 (2005).

[31] A. Dobado and F. J. Llanes-Estrada, Phys. Rev. D **69**, 116004 (2004).

[32] J.-W. Chen and E. Nakano, Phys. Lett. B **647**, 371 (2007).

[33] K. Itakura, O. Morimatsu, and H. Otomo, Phys. Rev. D **77**, 014014 (2008).

[34] A. Dobado, F. J. Llanes-Estrada, and J. M. Torres-Rincon, Phys. Rev. D **79**, 014002 (2009).

[35] N. Demir and S. A. Bass, Phys. Rev. Lett. **102**, 172302 (2009).

[36] D. Fernandez-Fraile and A. Gomez Nicola, Eur. Phys. J. C **62**, 37 (2009).

[37] J. Rose, J. M. Torres-Rincon, A. Schäfer, D. R. Oliinychenko, and H. Petersen, Phys. Rev. C **97**, 055204 (2018).

[38] H. Niemi, G. S. Denicol, P. Huovinen, E. Molnar, and D. H. Rischke, Phys. Rev. C **86**, 014909 (2012).

[39] J. E. Bernhard *et al.*, Phys. Rev. C **91**, 054910 (2015).

[40] C. Gale, S. Jeon, and B. Schenke, Int. J. Mod. Phys. A **28**, 1340011 (2013).

[41] H. B. Meyer, Phys. Rev. D **76**, 101701 (2007).

[42] H. B. Meyer, Nucl. Phys. A **830**, 641C (2009).

[43] M. Haas, L. Fister, and J. M. Pawlowski, Phys. Rev. D **90**, 091501 (2014).

[44] S. W. Mages, S. Borsányi, Z. Fodor, A. Schäfer, and K. Szabó, Proceedings: 32nd International Symposium on Lattice Field Theory , p232 (2015).

[45] P. B. Arnold, G. D. Moore, and L. G. Yaffe, J. High Energy Phys. **11**, 001 (2000).

[46] P. B. Arnold, G. D. Moore, and L. G. Yaffe, J. High Energy Phys. **05**, 051 (2003).

[47] J. Ghiglieri, G. D. Moore, and D. Teaney, J. High Energy Phys. **03**, 179 (2018).

[48] L. P. Csernai, J. Kapusta, and L. D. McLerran, Phys. Rev. Lett. **97**, 152303 (2006).

[49] G. D. Westfall *et al.*, Phys. Rev. Lett. **37**, 1202 (1976).

[50] E. Schnedermann, J. Sollfrank, and U. W. Heinz, Phys. Rev. C **48**, 2462 (1993).

[51] F. Retiere and M. A. Lisa, Phys. Rev. C **70**, 044907 (2004).

[52] PHENIX, A. Adare *et al.*, Phys. Rev. C **88**, 024906 (2013).

[53] ALICE, B. Abelev *et al.*, Phys. Rev. C **88**, 044910 (2013).

[54] A. Jaiswal and V. Koch, *preprint* (2015), arXiv:nucl-th/1508.05878.

[55] PHENIX, K. Adcox *et al.*, Nucl. Phys. A **757**, 184 (2005).

[56] STAR, J. Adams *et al.*, Nucl. Phys. A **757**, 102 (2005).

[57] M. He, R. J. Fries, and R. Rapp, Phys. Rev. C **82**, 034907 (2010).

[58] V. Greco, C. M. Ko, and P. Levai, Phys. Rev. C **68**, 034904 (2003).

[59] R. J. Fries, B. Muller, C. Nonaka, and S. A. Bass, Phys. Rev. Lett. **90**, 202303 (2003).

[60] R. J. Fries, B. Muller, C. Nonaka, and S. A. Bass, Phys. Rev. C **68**, 044902 (2003).

[61] R. Rapp and E. V. Shuryak, Phys. Rev. D **67**, 074036 (2003).

[62] L. Ravagli and R. Rapp, Phys. Lett. B **655**, 126 (2007).

[63] L. Ravagli, H. van Hees, and R. Rapp, Phys. Rev. C **79**, 064902 (2009).

[64] B. Muller, J. Schukraft, and B. Wyslouch, Ann. Rev. Nucl. Part. Sci. **62**, 361 (2012).

[65] ALICE, B. B. Abelev *et al.*, J. High Energy Phys. **06**, 190 (2015).

[66] Z. Yang and R. J. Fries, J. Phys. Conf. Ser. **832**, 012056 (2017).

[67] M. Damodaran, D. Molnar, G. G. Barnafoldi, D. Berenyi, and M. Ferenc Nagy-Egri, *preprint* (2017), arXiv:nucl-th/1707.00793.

[68] S. Ryu *et al.*, Phys. Rev. Lett. **115**, 132301 (2015).

[69] S. A. Bass *et al.*, MADAI collaboration: https://madai-public.cs.unc.edu/, accessed June, 2016.

[70] J. E. Bernhard, J. S. Moreland, S. A. Bass, J. Liu, and U. Heinz, Phys. Rev. C **94**, 024907 (2016).

[71] ALICE, J. Adam *et al.*, Phys. Rev. C **93**, 034913 (2016).

[72] PHENIX, A. Adare *et al.*, Phys. Rev. C **93**, 051902 (2016).

[73] J. Sollfrank, P. Koch, and U. W. Heinz, Z. Phys. C **52**, 593 (1991).

[74] H. Song and U. W. Heinz, Phys. Rev. C **81**, 024905 (2010).

[75] PHENIX, S. S. Adler *et al.*, Phys. Rev. Lett. **91**, 072301 (2003).

[76] D. Teaney, *preprint* (2002), arXiv:nucl-th/0204023.

[77] P. Huovinen and P. Petreczky, Nucl. Phys. A **837**, 26 (2010).

[78] C. M. Hung and E. V. Shuryak, Phys. Rev. C **57**, 1891 (1998).

[79] R. Rapp and J. Wambach, Eur. Phys. J. A **6**, 415 (1999).

[80] R. Rapp and E. V. Shuryak, Phys. Rev. Lett. **86**, 2980 (2001).

[81] T. Hirano and K. Tsuda, *preprint* (2002), arXiv:nucl-th/0202033.

[82] ALICE, S. Acharya *et al.*, Eur. Phys. J. C **77**, 658 (2017).

[83] ALICE, B. B. Abelev *et al.*, Phys. Lett. B **728**, 216 (2014), [Erratum: Phys. Lett. B **734**, 409 (2014)].

[84] STAR, L. Adamczyk *et al.*, Phys. Rev. C **94**, 034908 (2016).

[85] L. Zhu, H. Zheng, C. Ming Ko, and Y. Sun, Eur. Phys. J. A **54**, 175 (2018).

[86] P. Romatschke and S. Pratt, *preprint* (2014), arXiv:nucl-th/1409.0010.

[87] A. Dash, S. Samanta, and B. Mohanty, Phys. Rev. D **100**, 014025 (2019).

[88] R. J. Fries, V. Greco, and P. Sorensen, Ann. Rev. Nucl. Part. Sci. **58**, 177 (2008).

[89] PHENIX, A. Adare *et al.*, Phys. Rev. C **85**, 064914 (2012).

[90] K. Dusling, G. D. Moore, and D. Teaney, Phys. Rev. C **81**, 034907 (2010).

[91] G. Brown, J. Stachel, and G. Welke, Phys. Lett. B **253**, 19 (1991).

[92] X. Sun, H. Masui, A. M. Poskanzer, and A. Schmah, Phys. Rev. **C 91**, 024903 (2015).

[93] D. Tong, *University of Cambridge Graduate Course*, **Kinetic Theory** (2012).

[94] S. Pratt, A. Baez, and J. Kim, Phys. Rev. C **95**, 024901 (2017).

[95] J. Novak *et al.*, Phys. Rev. C **89**, 034917 (2014).

[96] J. Weil *et al.*, Phys. Rev. C **94**, 054905 (2016).

[97] R. Rapp, J. Wambach, and H. van Hees, Landolt-Bornstein **23**, 134 (2010).

APPENDIX A

HADRON SPECTRA FROM QUARK RECOMBINATION

Transverse momentum spectra of identified hadrons in different centrality bins of ALICE and RHIC, as a supplement to Fig. 5.2, 5.3. Symbols are experimental data, solid lines are recombination calculation. Parameters are given in Tab. 5.1.

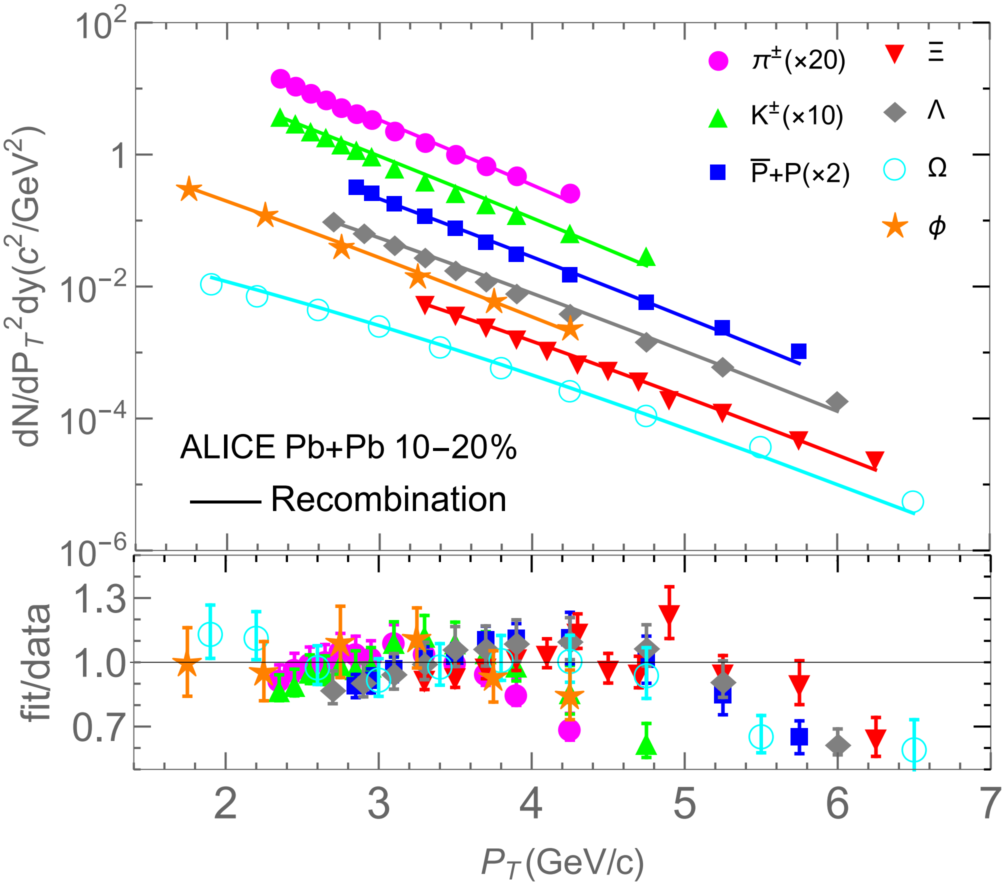

Figure A.1: Transverse momentum spectra for $\pi^{\pm}$, $K^{\pm}$, p+$\overline{p}$, ϕ, Λ+$\overline{\Lambda}$, Ξ^-+$\overline{\Xi}^+$ anΩ^-+$\overline{\Omega}^+$ in the ALICE 10-20% centrality bin. Symbols are experimental data, solid lines are recombination calculation.

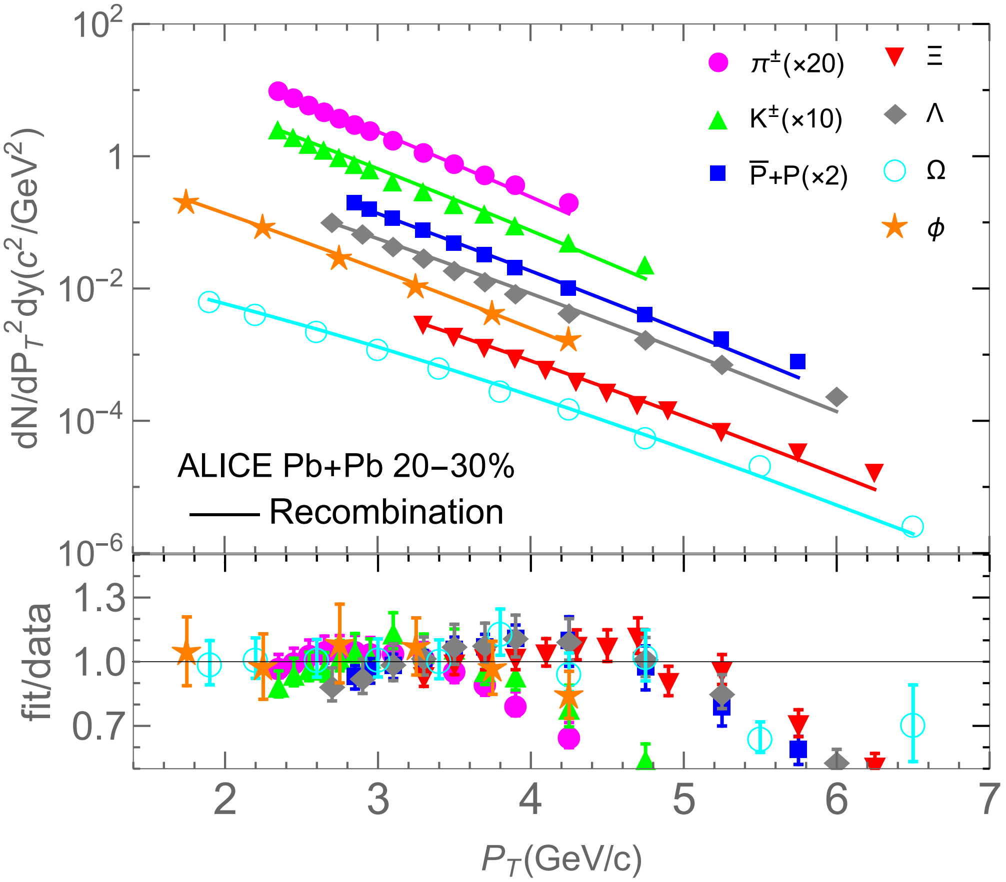

Figure A.2: Same as Fig. A.1 except in the ALICE 20-30% centrality bin. Λ,Ξ and Ω are from 20-40% centrality bin.

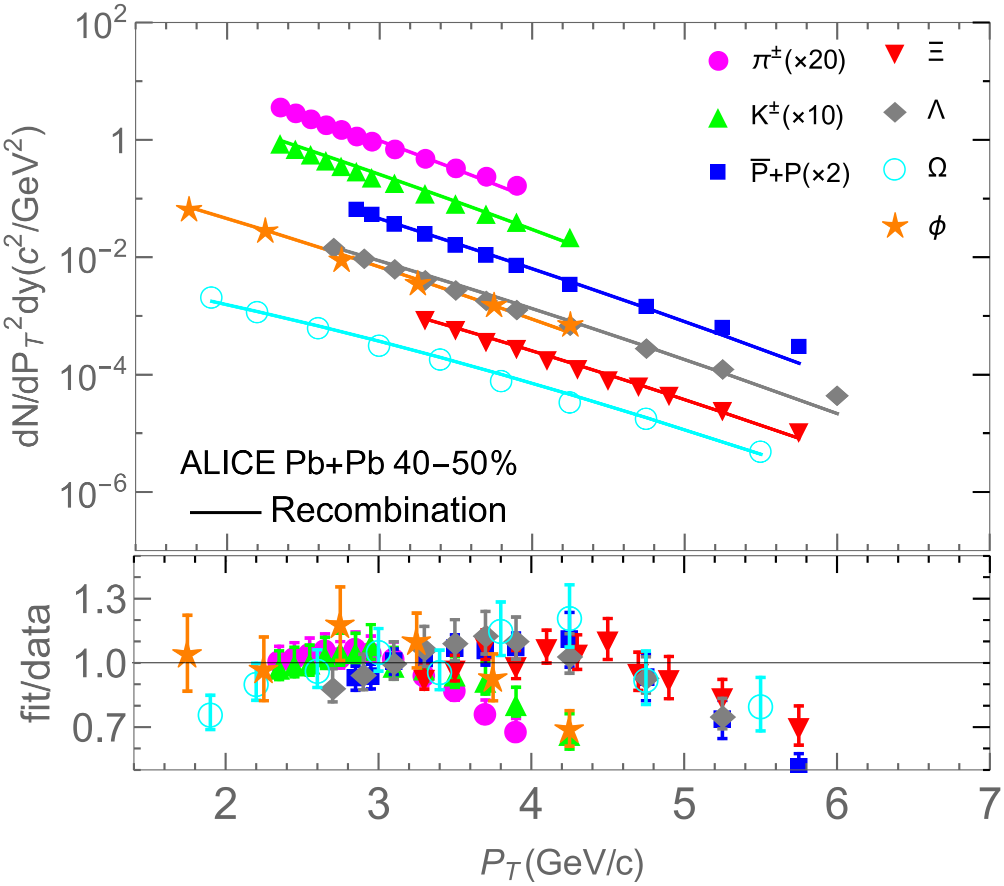

Figure A.3: Same as Fig. A.1 except in the ALICE 40-50% centrality bin. Λ,Ξ and Ω are from 40-60% centrality bin.

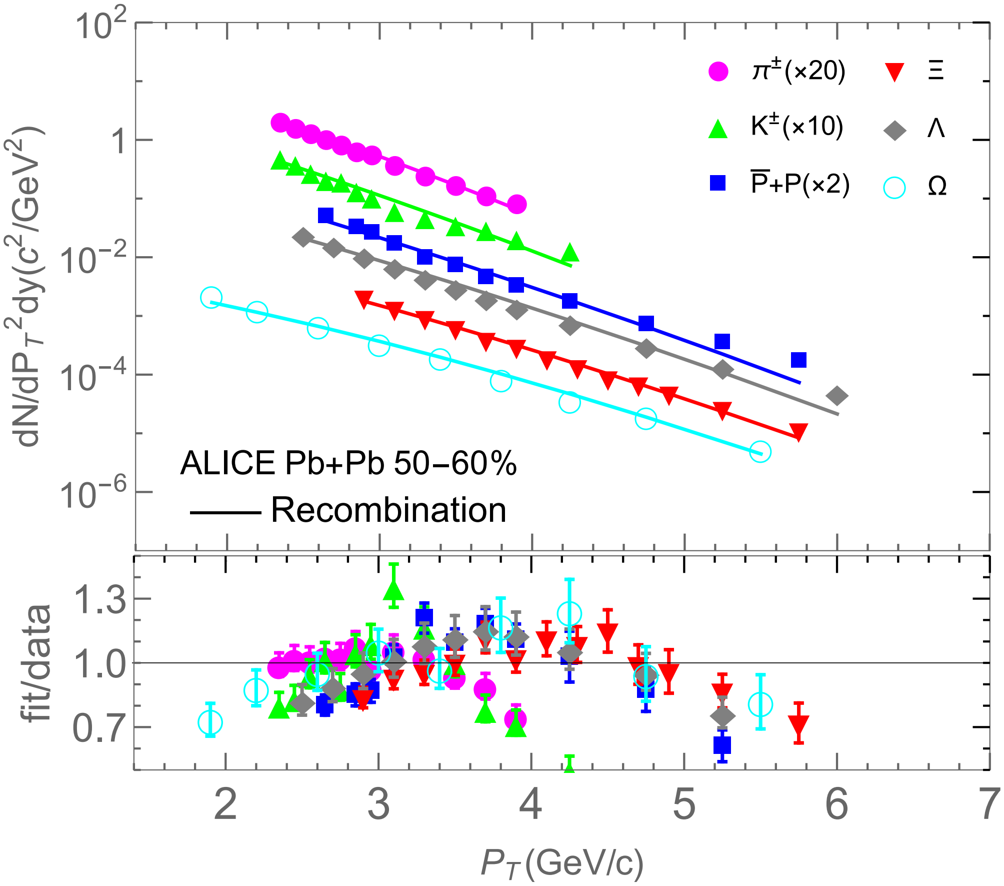

Figure A.4: Same as Fig. A.1 except in the ALICE 50-60% centrality bin. Λ,Ξ and Ω is from 40-60% centrality bin.

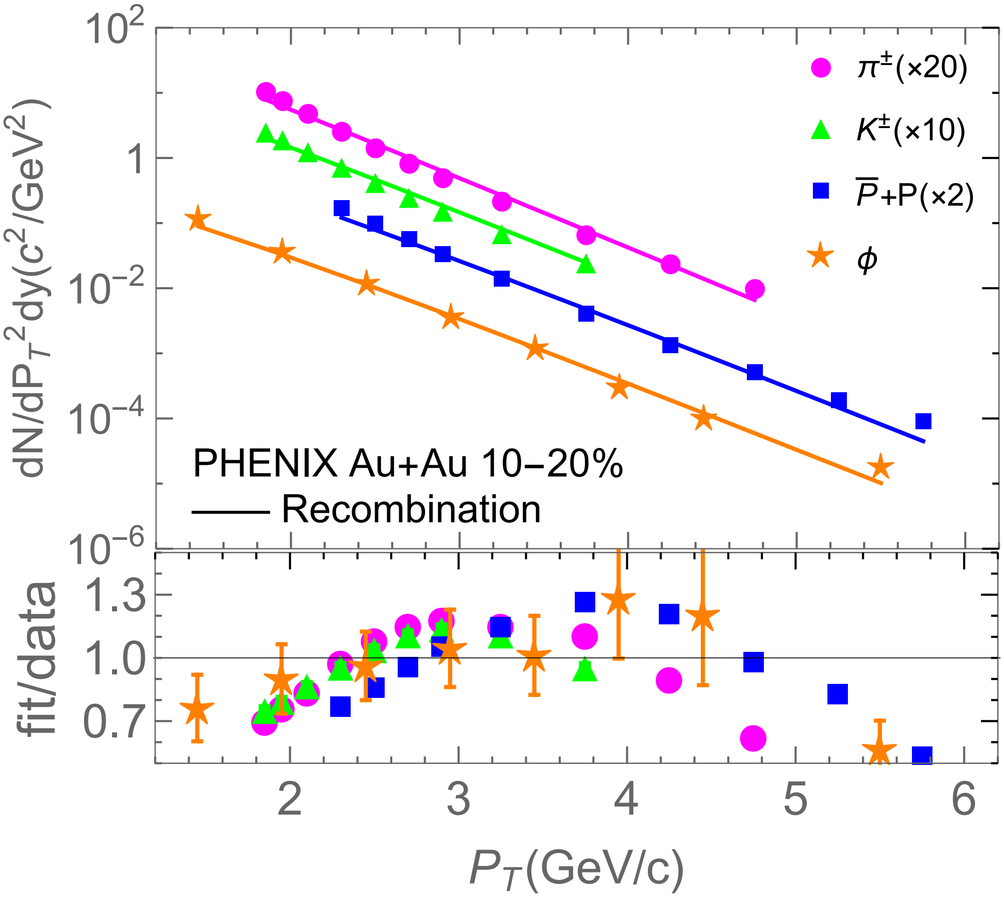

Figure A.5: Same as Fig. A.1 except in the PHENIX 10-20% centrality bin.

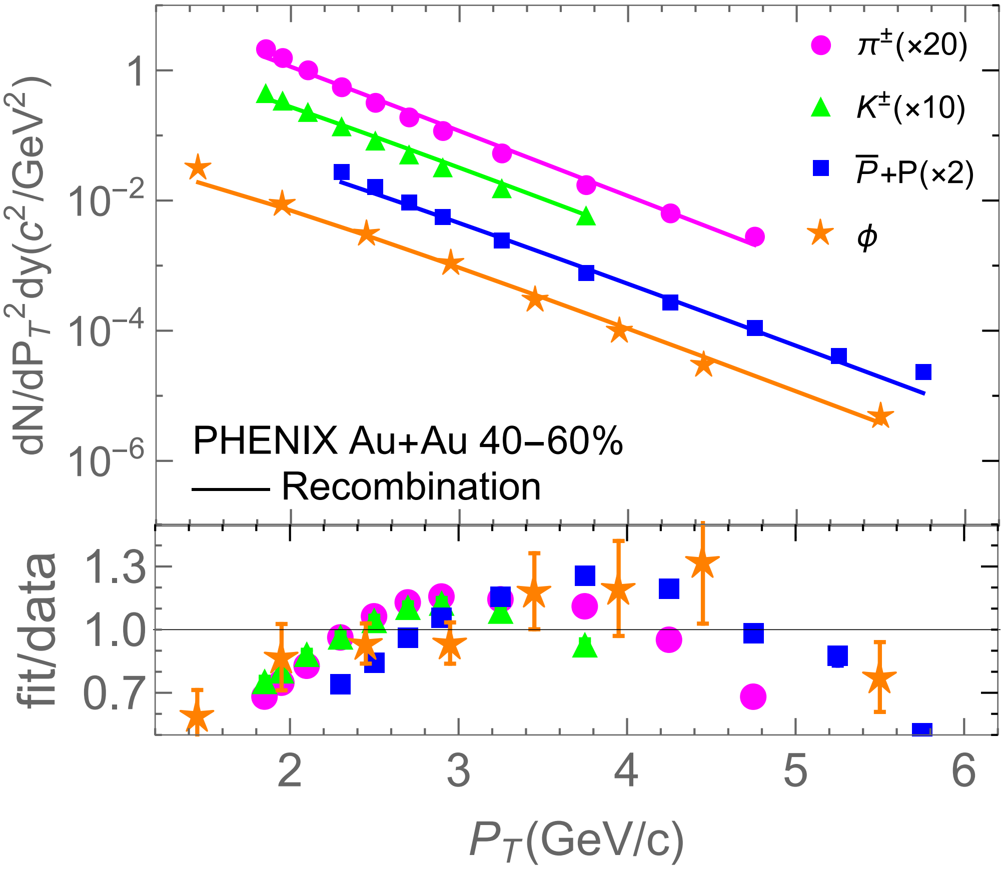

Figure A.6: Same as Fig. A.1 except in the PHENIX 40-60% centrality bin (ϕ is from 40-50 % centrality bin).

APPENDIX B

HADRON ELLIPTIC FLOW FROM QUARK RECOMBINATION

Elliptic flow of identified hadrons in different centrality bins of ALICE and RHIC, as a supplement to Fig. 5.4, 5.5. Symbols are experimental data, solid lines are recombination calculation. Parameters are given in Tab. 5.1.

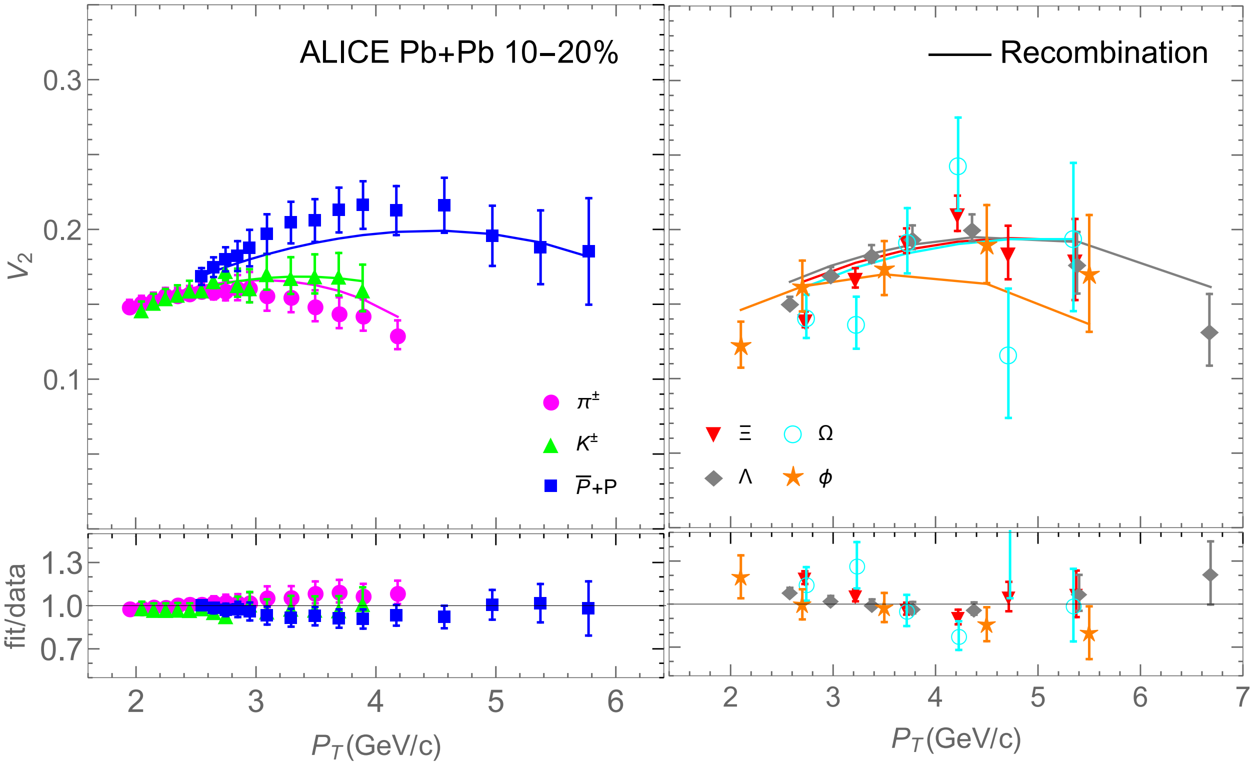

Figure B.1: Elliptic flow v_2 for $\pi^{\pm}$, K$^{\pm}$ and p+$\overline{\mathrm{p}}$ (left panel) and ϕ, Λ+$\overline{\Lambda}$, Ξ^-+$\overline{\Xi}^+$ and Ω^-+$\overline{\Omega}^+$ (right panel) in the ALICE 10-20 % centrality bin. Symbols are experimental data, solid lines are recombination calculation.

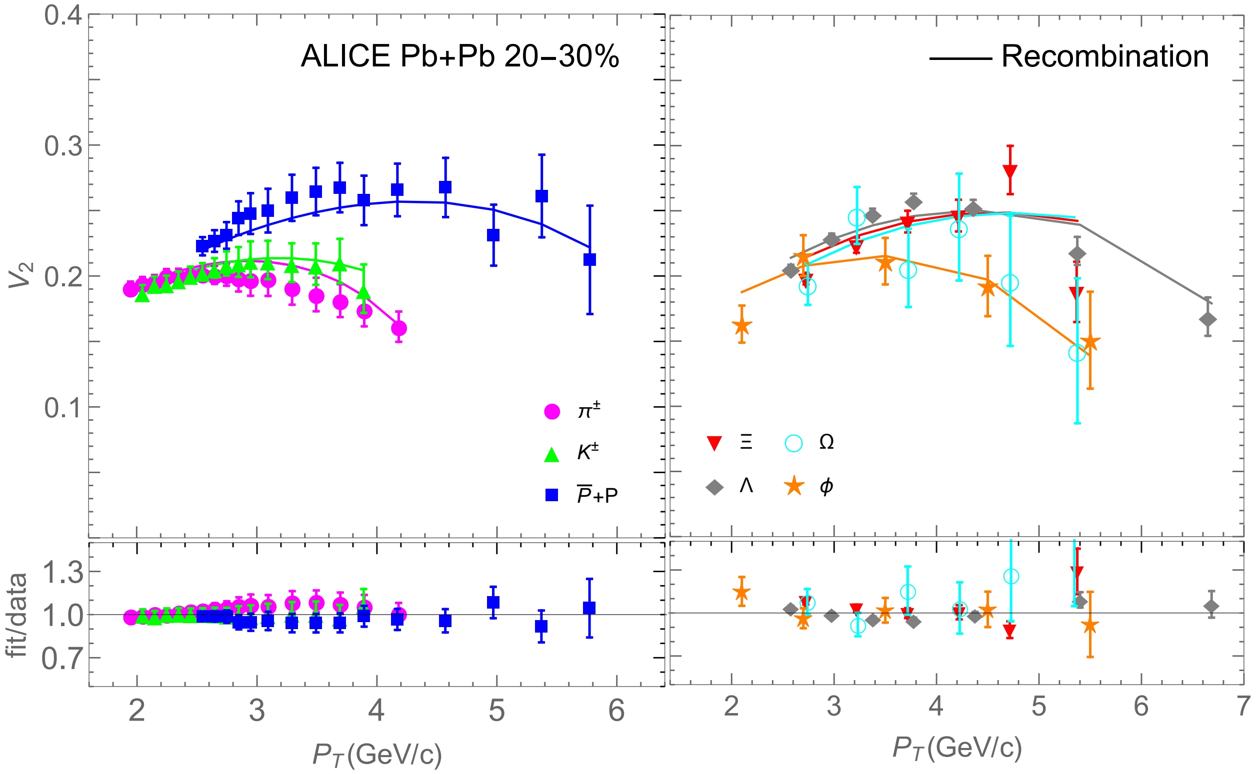

Figure B.2: Same as Fig. B.1 except in the ALICE 20-30 % centrality bin.

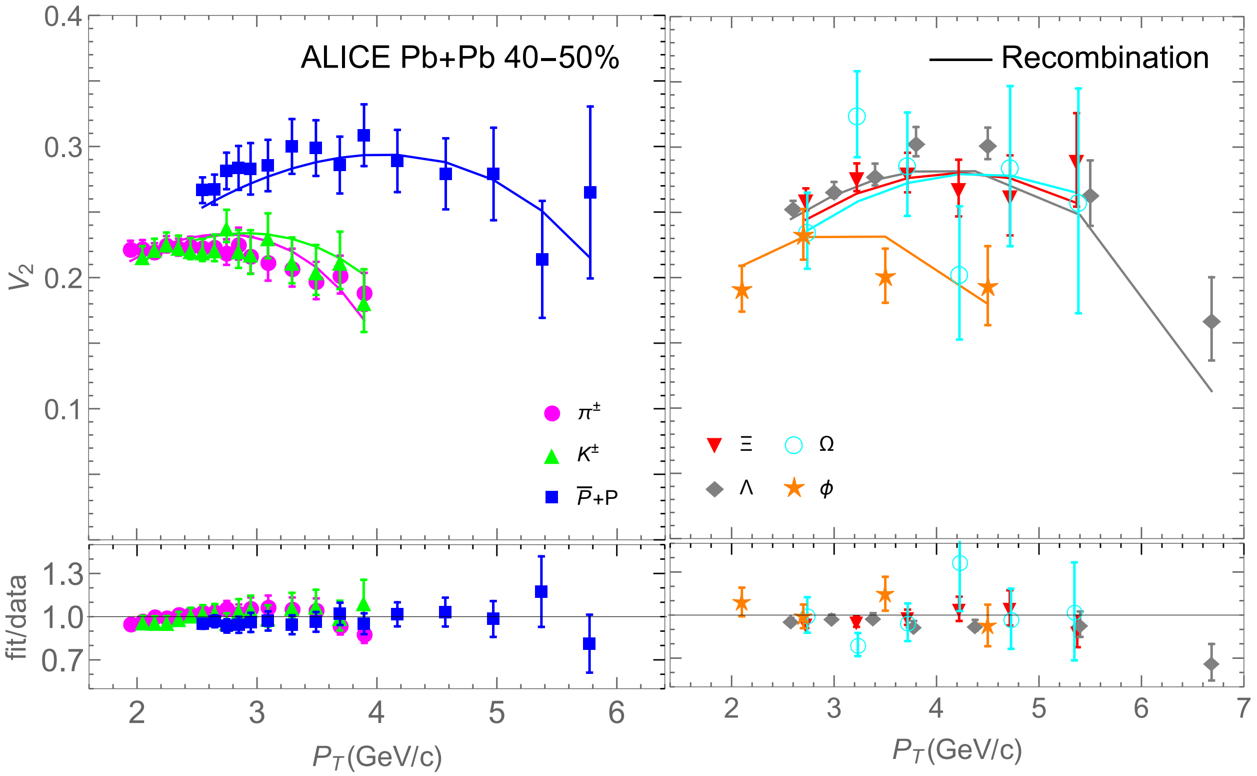

Figure B.3: Same as Fig. B.1 except in the ALICE 40-50 % centrality bin.

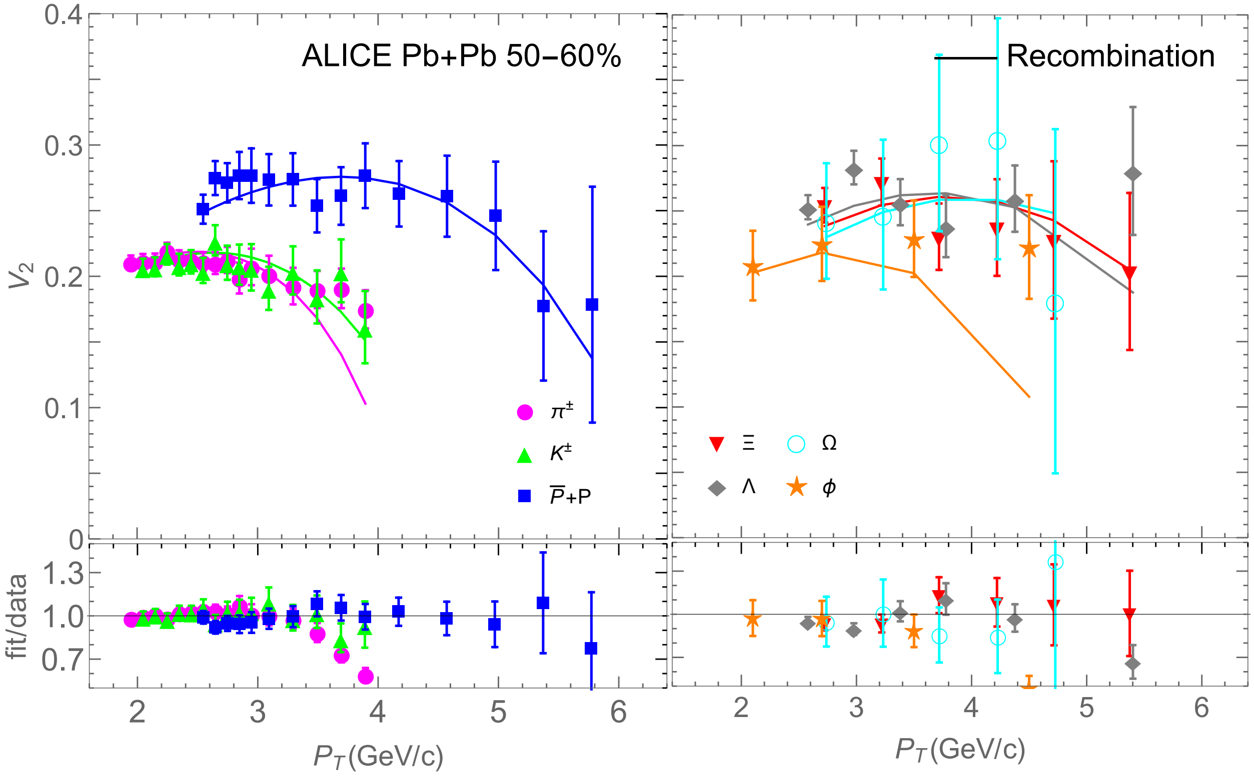

Figure B.4: Same as Fig. B.1 except in the ALICE 50-60 % centrality bin.

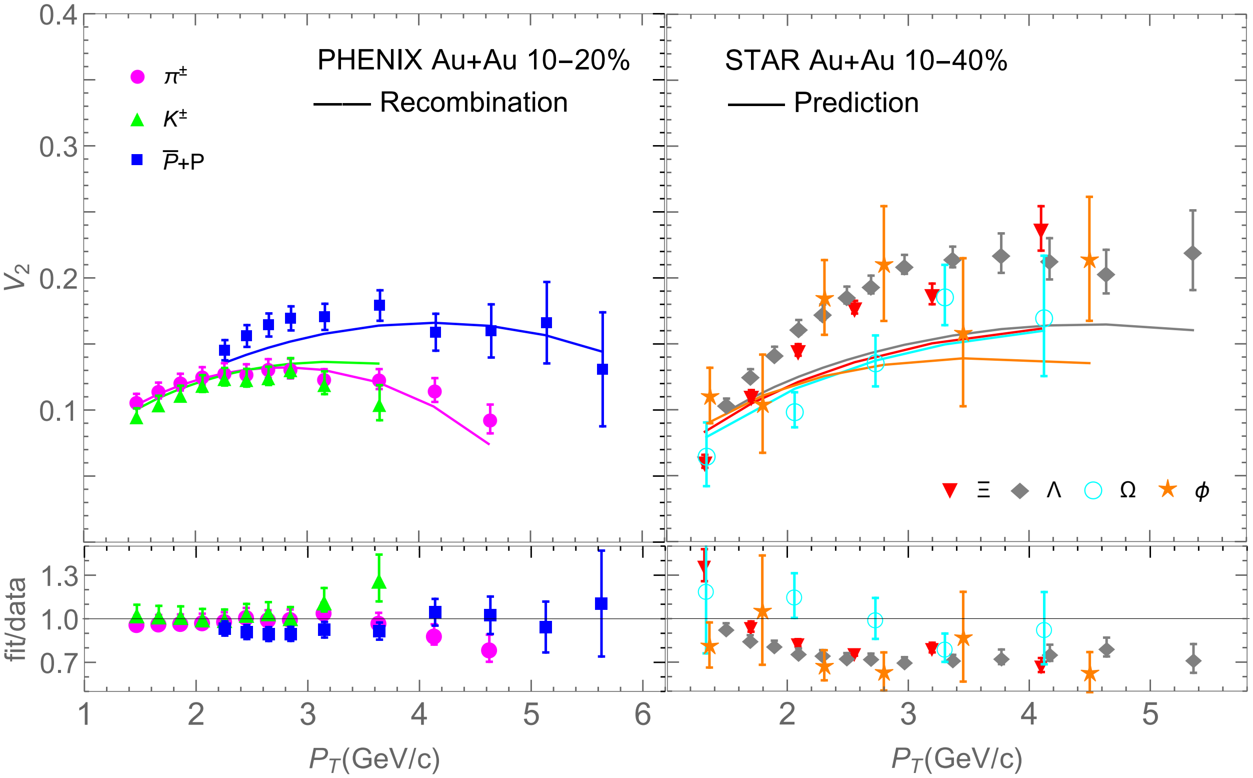

Figure B.5: Elliptic flow v_2 for $\pi^{\pm}$, $\mathrm{K}^{\pm}$ and p+$\overline{\mathrm{p}}$ (left panel) in the PHENIX 10-20% centrality bin and ϕ, Λ+$\overline{\Lambda}$, Ξ^{-}+$\overline{\Xi}^{+}$ and Ω^{-}+$\overline{\Omega}^{+}$ in the STAR 10-40% centrality bin (right panel).Ω is from the STAR 0-80% centrality bin. Symbols are experimental data, solid lines are recombination calculation. Note:we only fit π, K and p, right panel is calculated using the same parameter as left panel.

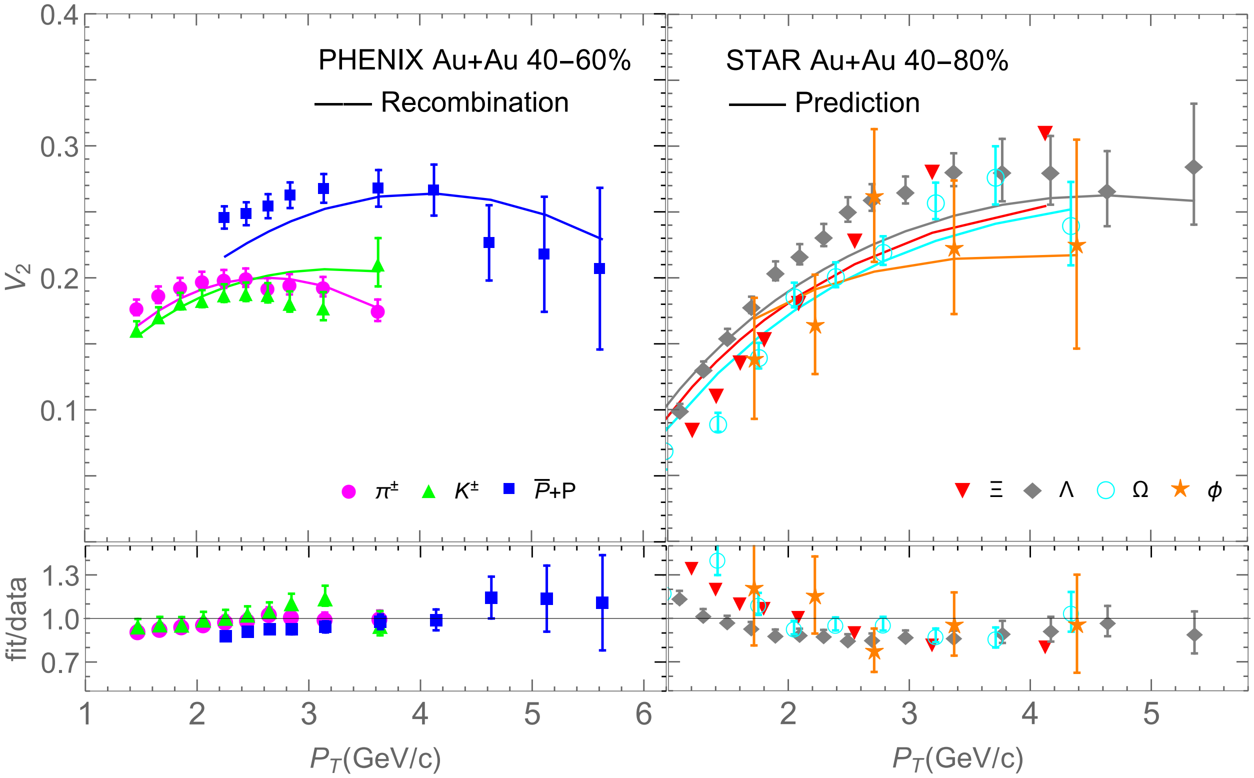

Figure B.6: Same as Fig. B.5 except in the PHENIX 40-60% centrality bin and STAR 40-80% centrality bin. Ω is from the STAR 30-80% centrality bin.